

## Elliptical accretion disk as a model for tidal disruption events

F.K. LIU,<sup>1,2</sup> C.Y. CAO,<sup>1</sup> M.A. ABRAMOWICZ,<sup>3,4,2,5</sup> M. WIELGUS ,<sup>6,7,2</sup> R. CAO,<sup>1</sup> AND Z.Q. ZHOU<sup>1</sup>

<sup>1</sup>*Department of Astronomy, School of Physics, Peking University, Beijing 100871, China*

<sup>2</sup>*Kavli Institute for Astronomy and Astrophysics, Peking University, Beijing 100871, China*

<sup>3</sup>*Nicolaus Copernicus Astronomical Center, Polish Academy of Sciences, Bartycka 18, PL-00-716 Warszawa, Poland*

<sup>4</sup>*Physics Department, University of Gothenburg, 412-96 Göteborg, Sweden*

<sup>5</sup>*Institute of Physics, Silesian University in Opava, Czech Republic*

<sup>6</sup>*Black Hole Initiative at Harvard University, 20 Garden St., Cambridge, MA 02138, USA*

<sup>7</sup>*Center for Astrophysics / Harvard & Smithsonian, 60 Garden Street, Cambridge, MA 02138, USA*

(Received June 1, 2019; Revised January 10, 2019; Accepted February 25, 2021)

Submitted to ApJ

### ABSTRACT

Elliptical accretion disk models for tidal disruption events (TDEs) have been recently proposed and independently developed by two groups. Although these two models are characterized by a similar geometry, their physical properties differ considerably. In this paper, we further investigate the properties of the elliptical accretion disk of the nearly uniform distribution of eccentricity within the disk plane. Our results show that the elliptical accretion disks have distinctive hydrodynamic structures and spectral energy distributions, associated with TDEs. The soft X-ray photons generated at pericenter and nearby are trapped in the disk and advected around the ellipse because of large electron scattering opacity. They are absorbed and reprocessed into emission lines and low-frequency continuum via recombination and bremsstrahlung emission. Because of the rapid increase of bound-free and free-free opacities with radius, the low-frequency continuum photons become trapped in the disk at large radius and are advected through apocenter and back to the photon-trapping radius. Elliptical accretion disks predict sub-Eddington luminosities and emit mainly at the photon-trapping radius of thousands of Schwarzschild radii with a blackbody spectrum of nearly single temperature of typically about  $3 \times 10^4$  K. Because of the self-regulation, the photon-trapping radius expands and contracts following the rise and fall of accretion rate. The radiation temperature is nearly independent of BH mass and accretion rate and varies weakly with the stellar mass and the viscosity parameter. Our results are well consistent with the observations of optical/UV TDEs.

*Keywords:* accretion, accretion disk — black hole physics — galaxies: active — quasars: supermassive black holes — stars: black holes

## 1. INTRODUCTION

When a star closely passing by a supermassive black hole (SMBH) is tidally disrupted, the subsequent accretion of stellar debris ignites the otherwise quiescent BH (Hills 1975; Rees 1988). In the classical work of Rees (1988), the bound stellar debris is expected to be circularized rapidly because of strong relativistic apsidal precession and to form a circular accretion disk of about twice the size of the orbital pericenter of the star. The hydrodynamic simulations of stellar tidal disruptions show that rapid circularization of the debris streams and the formation of a compact accretion disk are allowed when the orbital pericenter of the star is of order of the BH Schwarzschild radius and the self-intersection of the streams occurs near the orbital pericenter, which is caused by the strong relativistic apsidal precession (Ramirez-Ruiz & Rosswog 2009; Hayasaki et al. 2013; Guillochon et al. 2014; Bonnerot et al. 2016; Sadowski et al. 2016; Steinberg et al. 2019; Krolik et al. 2020; Ryu et al. 2020a). Because the accretion disk is hot and radiates dominantly in soft X-rays, the emission in optical/UV wave bands is the extremely weak Rayleigh-Jeans tail, and no strong broad optical emission line is expected (Strubbe & Quataert 2009).

The observations of tidal disruption events (TDEs) and candidates discovered in the optical/UV sky-surveys are inconsistent with the expectations and challenge the classical circular accretion disk model (see Komossa 2015, for a recent review of observations). Most optical/UV TDEs and candidates are much more luminous in optical/UV wave bands than expected and with little or no radiation in soft X-rays (e.g., Gezari et al. 2012; Holoien et al. 2014, 2016a,b; Blagorodnova et al. 2019; Leloudas et al. 2019; van Velzen et al. 2021) and have strong broad optical emission lines of complex and diverse profiles (Komossa et al. 2008; Gezari et al. 2012; Wang et al. 2012; Arcavi et al. 2014; Holoien et al. 2014, 2016b,a, 2019; Short et al. 2020; van Velzen et al. 2021) and of peculiar chemical abundance (Gezari et al. 2012; Arcavi et al. 2014; Short et al. 2020). The spectral energy distributions (SEDs) of all optical/UV TDEs are blackbodies of nearly single and constant temperature at about  $(1 - 6) \times 10^4$  K and the effective spherical blackbody radii of optical/UV radiations are as large as a few thousand Schwarzschild radii of SMBHs and much larger than the expected tidal disruption radius of main-sequence stars (Gezari et al. 2012; Holoien et al. 2014, 2016a,b, 2019; Nicholl et al. 2019; van Velzen et al. 2021). To solve the problem, it is proposed that an optically thick envelope of a few thousand Schwarzschild radii, enshrouding the compact hot accretion disk, forms and reprocesses the soft X-ray photons to low frequency at large radius (Strubbe & Quataert 2009; Lodato & Rossi 2011; Metzger & Stone 2016; Roth et al. 2016; Dai et al. 2018). The optically thick envelope may be formed by the disk outflows or winds during the super-Eddington accretion at the early time, and the photosphere would recede with the decay of the disk outflows and winds following the fallback rate. The broad optical emission lines form in the surface layers of the optically thick envelopes (Roth et al. 2016). A top-capped light curve regulated by the Eddington luminosity would be expected with the super-Eddington disk-envelope model for TDEs and significantly decoupled from the fallback rate during the super-Eddington accretion.

The close follow-up of the bolometric luminosity to the fallback rate of TDEs (e.g. Mockler et al. 2019) challenges the model of the super-Eddington accretion and strong outflows. The observations

of sub-Eddington peak bolometric luminosity and the extremely small amount of total accreted matter of TDEs challenge the circular accretion disk model (Saxton et al. 2018). The hydrodynamic simulations of tidal disruption of a star with orbital pericenter radius much larger than the BH Schwarzschild radius show that the circularization of the bound debris streams is quite inefficient and the circularization timescale is much longer than the fallback timescale, because the relativistic apsidal precession is little and the self-intersection of the streams occurs nearly at the apocenter of the most bound stellar debris (Shiokawa et al. 2015). Inspired by the hydrodynamic simulations, Piran et al. (2015) proposed that the optical and UV radiation of optical/UV TDEs is powered by the shocks at the self-intersection of streams, rather than accretion onto the SMBH. Provided that the fallback materials, including the most bound stellar debris, have zero initial bound energy and the thermal energy converted from the orbital kinetic energy by the shocks can be radiated efficiently with little of the heat being converted back into kinetic energy, they showed that the shock model can approximately explain the observations of optical luminosities, the low temperature, and the large radiation radius of optical/UV TDEs at the peak brightness. Because the shock model neglects the radiation contributions of disk accretion, it has to explain what happens to this radiation (Piran et al. 2015). It is argued that the radiation originating from the accretion disk may be much weaker than that originating from the shocks at the apocenter, if the angular momentum transport in the accretion disk is much faster than the orbital energy dissipation, and the eccentricity of the inner parts of the debris disk rises so much that the pericenter radius of the orbits of the inner accretion disk reaches the marginally bound orbit, and the matter plunges directly onto the BH without significant decrease of the orbital semimajor axis (Svirski et al. 2017; Chan et al. 2018).

The evolution of eccentricity of accretion disks is complex. The hydrodynamic investigations of eccentric accretion disks show that the eccentricity of an elliptical accretion disk may or may not decrease with time because the viscosity may not lead to the circularization of a disk (Syer & Clarke 1992; Lyubarskij et al. 1994; Ogilvie 2001; Ogilvie & Barker 2014). The investigations of magnetohydrodynamic (MHD) stress and the magnetorotational instability (MRI) in eccentric accretion disks show that in some situations the angular momentum transport is more efficient, but in other cases the orbital energy dissipation is more significant. It is unclear which one is preferred in the accretion disk of TDEs, and more investigations are needed (Svirski et al. 2017; Chan et al. 2018).

Liu and colleagues (Liu et al. 2017; Cao et al. 2018) recently proposed an elliptical accretion disk model for TDEs, whose size and eccentricity are mainly determined by the orbital pericenter of a star and the relativistic apsidal precession of the most bound stellar debris. The orbital eccentricity of the disk fluid elements is nearly the same across different radii. The inner edge is determined by the marginal bound orbit and the eccentricity of the inner disk fluids. They suggested that the double-peaked broad  $H\alpha$  emission line of the TDE candidate PTF09djl, as a reminiscent of the double-peaked broad Balmer emission lines of active galactic nuclei (AGNs), originates in the eccentric accretion disk (Liu et al. 2017). They suggested to observationally determine the structure of the accretion disk of TDEs by modeling the complex and asymmetric profiles of broad optical emission lines of optical/UV TDEs (Liu et al. 2017; Cao et al. 2018). The disk origination of broad optical emission lines can naturally explain the complexities, asymmetries, and diversities of the line profiles with the random disk inclinations and pericenter orientations (Liu et al. 2017; Cao et al. 2018; Holoien et al. 2019; Short et al. 2020), the peculiar intensity ratios of broad emission lines of the He and H elements with the chromosphere of the optically thick disk as in cataclysmic variables and hot main-sequence

stars (Gaskell & Rojas Lobos 2014; Guillochon et al. 2014; Roth et al. 2016; Liu et al. 2017; Cao et al. 2018), and the flat Balmer decrement of some optical/UV TDEs (Short et al. 2020). Modeling the double-peaked line profiles of PTF09djl suggests that the peculiar substructures of the line profiles with one peak at the line rest wavelength and the other redshifted to about  $3.5 \times 10^4 \text{ km s}^{-1}$  are mainly due to the orbital motion of the emitting matter within the disk plane of size a few hundred Schwarzschild radii and of roughly uniform eccentricity of about 0.966 (Liu et al. 2017). Modeling the optical emission lines of the TDE ASASSN-14li with radically different profiles also reveals a large accretion disk of size up to 1700 Schwarzschild radii and roughly uniform eccentricity about 0.977 (Cao et al. 2018).

Elliptical accretion disk models for the TDEs have been independently suggested by two groups – Piran et al. (2015) and Liu et al. (2017). The similarities of these models follow from the fact that the TDEs originate from matter with a lot of energy (of order of the binding energy at the apocenter) and very little angular momentum (of order of the angular momentum of rotation at the pericenter). Unless there is a rapid process of energy dissipation, this will lead to an elliptical disk. At the same time, there is an "inverse energy crisis" as the energy observed in TDEs is around  $10^{51}$  erg (or at most  $10^{52}$  erg) while the energy reservoir has  $> 10^{53}$  erg. This suggests that the elliptical disk does not circularize quickly, if at all. Although the two models are characterized by a similar geometry, their physical properties differ considerably.

Piran and colleagues argued that the energy dissipation at the disk is not the energy source of the observed radiation. The energy source of the radiation is the stream-stream interaction that takes place at around the apocenter. The dissipation processes that take place in the elliptical disk are mostly unimportant given the fact that it loses some small fraction of its angular momentum and then the matter falls ballistically onto the BH without energy production (Piran et al. 2015; Svirski et al. 2017). Piran (2015) coined the name "Jerusalem bagel" for these disks because of their oval shape – in contrast to the circular thick accretion disks, often referred to as Polish doughnuts (Abramowicz et al. 1978). The dynamics and thermal emission of the elliptical accretion disk heated by the self-crossing shocks at about apocenter have been investigated recently (Zanazzi & Ogilvie 2020).

In contrast, the elliptical accretion disk model of the Beijing group assumes that the energy dissipation occurs mainly in the accretion of the matter into the BH, because of the uniform eccentricity of the fluid orbits. The energy dissipation from the shocks at apocenter is unimportant (Liu et al. 2017; Cao et al. 2018; Zhou et al. 2021). To stress similarities and differences, we call these disks "Jerusalem bagels from Beijing."

The accretion of matter with large orbital eccentricity onto the central BH would convert a small but significant amount of the orbital kinetic energy into heat (Liu et al. 2017; Cao et al. 2018; Zhou et al. 2021). Based on the relativistic elliptical accretion disk model, we recently calculated the conversion efficiency of matter into radiation and compared the model expectations of peak luminosity and total radiation energy with the observations of a sample of TDEs (Zhou et al. 2021). The results showed that the expectations of both the peak luminosity and total radiation energy of TDEs are well consistent with the observations. The masses of SMBHs of the TDEs, derived by comparing the model expectations and the observations, are well consistent with the estimates of BH masses of the sample TDE sources obtained with the  $M_{\text{BH}} - \sigma_*$  relation of the BH mass and the stellar velocity dispersion of host galaxy (Zhou et al. 2021).

In this paper, we investigate the dynamic structure and SED of an elliptical accretion disk of uniform eccentricity. The relationship of the TDEs discovered in the optical/UV and X-ray transient surveys will be discussed in the next work. Following Liu et al. (2017) and Cao et al. (2018), for simplicity we assume that the elliptical accretion disk consists of an aligned ellipse of uniform eccentricity. Because the orbital energy dissipation happens mainly at pericenter and near regions with radius  $r \sim r_p$  and  $-\pi/2 \lesssim \phi \lesssim \pi/2$ , with  $\phi$  the azimuthal angle starting at pericenter (Svirski et al. 2017; Chan et al. 2018), and the angular momentum transport near apocenter may be less efficient (Chan et al. 2018), we assume for simplicity that the heat generation and angular momentum transfer occur only at pericenter and nearby and that both effects can be described by introducing an effective viscosity parameter  $\alpha$  of a step function with  $\alpha = \alpha_p$  for  $r \sim r_p$  and  $-\pi/2 \lesssim \phi \lesssim \pi/2$  and  $\alpha = 0$  otherwise.

The paper is organized as follows. In section 2 we briefly introduce the elliptical accretion disk model for TDEs. Sections 3-5 discuss, respectively, the mass conservation, angular momentum conservations, and heat generation of a vertically integrated quasi-stationary elliptical accretion disk. In section 6, we investigate the hydrodynamic structures around a highly eccentric ellipse. The vertical hydro-equilibrium and the distributions of mass density, temperature, and radiation around the ellipse are distinctively different from those in circular annulus of the circular accretion disk. In section 7, we compare the expectations of the elliptical accretion disk model and the observations of optical/UV TDEs. It is shown that the expectations are well consistent with the observations. A brief discussion and conclusions are given in section 8.

## 2. THE ELLIPTICAL ACCRETION DISK MODEL FOR TDES

### 2.1. The elliptical accretion disk

In this section, we summarize the properties of the elliptical accretion disk model. A more detailed and complete description can be found in Liu et al. (2017) and Cao et al. (2018).

A star of radius  $R_*$  and mass  $M_*$  is tidally disrupted by an SMBH of mass  $M_{\text{BH}}$ , when the orbital pericenter radius of the star,  $r_{p*}$ , is less than the tidal disruption radius

$$\begin{aligned} r_t &= f_T R_* (M_{\text{BH}}/M_*)^{1/3} \\ &\simeq 23.545 f_T r_* m_*^{-1/3} M_6^{-2/3} r_S, \end{aligned} \quad (1)$$

where  $r_* = R_*/R_\odot$ ,  $m_* = M_*/M_\odot$ ,  $M_6 = M_{\text{BH}}/10^6 M_\odot$ , and  $r_S = 2GM_{\text{BH}}/c^2$ . The correction factor  $f_T$  depends on the internal stellar structure (Phinney 1989; Guillochon & Ramirez-Ruiz 2013; Ryu et al. 2020a,b) and relativistic effects (Ivanov & Chernyakova 2006; Ryu et al. 2020a). The general relativistic hydrodynamic simulations of tidal disruptions of a main sequence star give the correction factor  $f_T = f_{\text{BH}} f_*$  with  $f_{\text{BH}} \simeq 0.80 + 0.26 M_6^{0.5}$  and  $f_* \simeq 1.47$  for a star of mass  $m_* \lesssim 0.5$  and  $f_* \simeq 1/2.34$  for star of mass  $m_* \gtrsim 1$  (Ryu et al. 2020a). For star of typical mass  $m_* = 0.3$  and BH of typical mass  $M_6 = 1$ ,  $f_T \simeq 1.56$ . We notice that here we adopt the Latin letters  $f_T$ ,  $f_*$  and  $f_{\text{BH}}$  to note the correction factors, which are, respectively, denoted by the Greek letters  $\Psi$ ,  $\Psi_*$  and  $\Psi_{\text{BH}}$  in Ryu et al. (2020a). After tidal disruption, about half of the stellar debris becomes bound and returns to the orbital pericenter of the star. The fallback rate of the bound stellar debris after peak is approximately a power-law,

$$\dot{M} \simeq \dot{M}_p \left( \frac{t + \Delta t_p}{\Delta t_p} \right)^{-n}, \quad (2)$$

where time  $t$  starts at peak fallback rate and the power-law index  $n$  depends on both the structure and age of the star (Rees 1988; Evans & Kochanek 1989; Phinney 1989; Lodato et al. 2009; Guillochon

& Ramirez-Ruiz 2013; Stone et al. 2013) and the orbital penetration factor  $\beta_* = r_t/r_{p*}$  (Guillochon & Ramirez-Ruiz 2013; Coughlin & Nixon 2019; Ryu et al. 2020a). For full tidal disruptions,  $n = 5/3$  is a very good approximation except for at about the peak time (Guillochon & Ramirez-Ruiz 2013), and for partial disruptions  $n = 9/4$  is more typical (Guillochon & Ramirez-Ruiz 2013; Coughlin & Nixon 2019; Ryu et al. 2020a). The peak time  $\Delta t_p$  and peak fallback rate  $\dot{M}_p$  are, respectively,

$$\begin{aligned}\Delta t_p &\simeq 2\pi \left( \frac{a_{\text{mb}}^3}{GM_{\text{BH}}} \right)^{1/2} \\ &\simeq 0.1122 f_{\text{T}}^3 r_*^{3/2} m_*^{-1} M_6^{1/2} \text{ yr}\end{aligned}\quad (3)$$

with  $a_{\text{mb}} \simeq r_t^2/(2R_*)$  the orbital semi-major axis of the most tightly bound stellar debris and

$$\begin{aligned}\dot{M}_p &\simeq \frac{M_*}{3\Delta t_p} \left[ \frac{3}{2}(n-1) \right] \\ &\simeq 2.972 [3(n-1)/2] f_{\text{T}}^{-3} r_*^{-3/2} m_*^2 M_6^{-1/2} M_{\odot}/\text{yr}.\end{aligned}\quad (4)$$

When it is needed in this paper, we adopt the mass-radius relation for a main-sequence star to convert the radius to the mass of a star:  $r_* \simeq m_*^{1-\zeta}$  with  $\zeta = 0.21$  for  $0.1 \leq m_* \leq 1$  and  $\zeta = 0.44$  for  $1 \leq m_* \leq 150$  (Kippenhahn & Weigert 2012).

In the popular circular accretion disk model for TDEs in the literature, the typical radiation efficiency  $\eta = 0.1$  is adopted and the peak mass fallback rate given by equation (2) leads to hyper-Eddington luminosities for TDEs with the BH mass  $M_{\text{BH}} \sim 10^6 M_{\odot}$  and strong outflows may be driven by the radiation pressure (Strubbe & Quataert 2009; Lodato & Rossi 2011; Metzger & Stone 2016; Roth et al. 2016; Dai et al. 2018) or may not (see the theoretical arguments given by Abramowicz et al. (2000)). The real accretion rate of matter onto the BH is expected to significantly deviate from the mass fallback rate given by equation (2). Because the radiation efficiency of the elliptical accretion disk is as small as  $\sim 10^{-3}$  (Liu et al. 2017; Cao et al. 2018; Zhou et al. 2021, see also equation (142)) and the peak luminosity is sub-Eddington for TDEs with the BH mass  $M_{\text{BH}} \gtrsim 10^6 M_{\odot}$  (see also equation (143)), no strong outflow is expected for the elliptical accretion disks, and the accretion rate of matter onto the BH would closely follow the mass fallback rate given by equation (2). In this paper, the results are given as functions of the accretion rate  $\dot{M}$  and the peak fallback rate  $\dot{M}_p$  given by equation (4) is adopted mainly for scaling the accretion rate. The results are mainly determined by the accretion rate and nearly independent of the power-law index  $n$ . However, when it is needed, we will assume that the accretion rate is the mass fallback rate given by equation (2) and present the results as functions of time for the typical value  $n = 5/3$ . As an example, we will discuss the results obtained for both  $n = 5/3$  and  $n = 9/4$  in Sec. 7.3.

The semi-major axis of the elliptical orbit of the bound stellar debris after fallback is reduced to form an accretion disk mainly due to the shocks of the intersection of the newly inflowing and post-pericenter outflowing fluid streams because of the relativistic apsidal precession (Rees 1988; Evans & Kochanek 1989; Kochanek 1994; Hayasaki et al. 2013; Dai et al. 2015; Shiokawa et al. 2015; Bonnerot et al. 2016; Hayasaki & Loeb 2016). The semimajor axis  $a_d$  of the accretion disk determined by the location of the self-intersections is approximately

$$a_d \simeq \frac{r_{p*}}{1 - e_{\text{mb}} + 2^{-1} \sin^2(\Omega_{\text{dS}}/2)}$$

$$\simeq \frac{2\beta_*^{-1}r_t}{2\delta + \sin^2(\Omega_{\text{dS}}/2)} \quad (5)$$

and the eccentricity of accretion disk given by the conservation of angular momentum of the streams is

$$e_d \simeq \left[ 1 - \frac{(1 - e_{\text{mb}}^2)a_{\text{mb}}}{a_d} \right]^{1/2} \\ \simeq [1 - 2\delta(1 + \Delta_*)]^{1/2} \quad (6)$$

with  $\Delta_* \equiv \sin^2(\Omega_{\text{dS}}/2)/2\delta$  and  $\delta = 2R_*r_{\text{p}*}/r_t^2 \simeq 0.02f_{\text{T}}^{-1}\beta_*^{-1}m_*^{1/3}M_6^{-1/3}$  (Liu et al. 2017; Cao et al. 2018), where  $e_{\text{mb}} = 1 - \delta$  is the orbital eccentricity of the most bound stellar debris and  $\Omega_{\text{dS}}$  is the instantaneous de Sitter precession at periapse of the most bound stellar debris (de Sitter 1916),

$$\Omega_{\text{dS}} \simeq \frac{6\pi GM_{\text{BH}}}{c^2(1 - e_{\text{mb}}^2)a_{\text{mb}}} \\ \simeq \frac{3\pi r_{\text{S}}}{(1 + e_{\text{mb}})r_{\text{p}*}} \\ \simeq \frac{3\pi r_{\text{S}}}{2} \frac{\beta_*}{r_t} \quad (7)$$

From equation (7), we have  $\Delta_* \simeq \frac{1}{4}f_{\text{T}}^{-1}\beta_*^3r_*^{-2}m_*^{1/3}M_6^{5/3}$  for  $r_{\text{p}*} \gg r_{\text{S}}$ .

Following Liu et al. (2017) and Cao et al. (2018), we assume for simplicity that the eccentric accretion disk consists of a nested aligned ellipse of semimajor axis  $a$  and uniform eccentricity  $e$  with  $e = e_d$  and that the fluid elements in the cylindrical coordinates  $(r, \phi, z)$  have trajectories

$$r = \frac{a(1 - e^2)}{1 + e \cos(\phi)}, \quad (8)$$

where  $r$  is the radius from the center of the BH and  $\phi$  starts from the orientation of pericenter.

To include the general relativistic effects in our Newtonian treatments, we adopt the generalized Newtonian potential in the low-energy limit

$$\Phi_{\text{G}}(r, \dot{r}, \dot{\phi}) = -\frac{GM_{\text{BH}}}{r} - \left( \frac{2r_{\text{g}}}{r - 2r_{\text{g}}} \right) \times \\ \left[ \left( \frac{r - r_{\text{g}}}{r - 2r_{\text{g}}} \right) \dot{r}^2 + \frac{r^2 \dot{\phi}^2}{2} \right] \quad (9)$$

with  $r_{\text{g}} = r_{\text{S}}/2 = GM_{\text{BH}}/c^2$  the gravitational radius (Tejeda & Rosswog 2013), which is a good approximation for particles with large eccentricity and low bound energy. With the generalized Newtonian potential, the trajectories of particles in Schwarzschild space-time and the radial dependences of the specific binding energy and angular momentum of the elliptical orbits can be reproduced exactly. Provided the semimajor axis  $a$  and eccentricity  $e$  of the elliptical orbit, the specific angular momentum  $l_{\text{G}}$  and binding energy  $e_{\text{G}}$  are, respectively,

$$l_{\text{G}} = \frac{(1 - e^2)ac\sqrt{r_{\text{S}}}}{\sqrt{2(1 - e^2)a - (3 + e^2)r_{\text{S}}}}$$

$$= \frac{(1+e)r_p c \sqrt{r_s}}{\sqrt{2(1+e)r_p - (3+e^2)r_s}}, \quad (10)$$

$$e_G = \frac{c^2 [(1-e^2)a - 2r_s]r_s}{2a [2(1-e^2)a - (3+e^2)r_s]} = \frac{c^2 [(1+e)r_p - 2r_s]r_s}{2a [2(1+e)r_p - (3+e^2)r_s]} \quad (11)$$

(Liu et al. 2017; Cao et al. 2018), where  $r_p = (1-e)a$  is the pericenter radius of the elliptical orbit. Noticing  $(3+e^2)/2(1+e) = 1 + [(1-e)/2]^2 [2/(1+e)]$  and neglecting the terms  $[(1-e)/2]^2$  or higher, we have

$$l_G \simeq \left(\frac{1+e}{2}\right)^{1/2} \left(\frac{r_p}{r_s}\right)^{1/2} \left(1 - \frac{r_s}{r_p}\right)^{-1/2} r_s c \quad (12)$$

$$e_G \simeq \frac{c^2}{4} \left(\frac{r_s}{a}\right) \left[1 - \left(\frac{2}{1+e}\right) \left(\frac{r_s}{r_p}\right)\right] \left[1 - \left(\frac{r_s}{r_p}\right)\right]^{-1}. \quad (13)$$

With the specific angular momentum and binding energy, the radial and azimuthal velocities at  $r$  and  $\phi$  are, respectively,

$$v_r = c \left(1 - \frac{r_s}{r}\right) \sqrt{2 \frac{e_G}{c^2} + \frac{r_s}{r} - \frac{l_G^2}{r^2 c^2} \left(1 - \frac{r_s}{r}\right)}, \quad (14)$$

$$v_\phi = r \dot{\phi} = l_G \frac{r - r_s}{r^2} = \left(1 - \frac{r_s}{r}\right) \frac{l_G}{r} \quad (15)$$

(Tejeda & Rosswog 2013). From equations (14), (15), (10), and (11), we obtain

$$v_r \simeq c \left(\frac{r_s}{r}\right)^{1/2} \left(1 - \frac{r_s}{r}\right) \left(1 - \frac{r}{2a}\right)^{1/2} \left[1 - \left(\frac{1+e}{2}\right) \left(\frac{r_p}{r}\right) \frac{2a}{2a-r}\right]^{1/2}, \quad (16)$$

$$v_\phi \simeq c \left(\frac{1+e}{2}\right)^{1/2} \left(\frac{r_p}{r_s}\right)^{-1/2} \left(1 - \frac{r_s}{r_p}\right)^{-1/2} \left(1 - \frac{r_s}{r}\right) \left(\frac{r_p}{r}\right), \quad (17)$$

and the angular velocity

$$\Omega = \dot{\phi} = \frac{v_\phi}{r} = \left(\frac{1+e}{2}\right)^{1/2} \left(\frac{r_p}{r_s}\right)^{1/2} \left(1 - \frac{r_s}{r_p}\right)^{-1/2} \left(1 - \frac{r_s}{r}\right) \left(\frac{r_s}{r^2}\right) c. \quad (18)$$

To obtain the Equations (16)-(18), we neglect the terms  $[(1-e)/2]^2$  or higher. From equations (16) and (17), we have the fluid velocity

$$v = (v_r^2 + v_\phi^2)^{1/2} \simeq c \left(1 - \frac{r_s}{r}\right) \left(\frac{r_s}{r}\right)^{1/2} \left(1 - \frac{r}{2a}\right)^{1/2} \left[1 + \left(\frac{1+e}{2}\right) \left(\frac{r_s}{r}\right) \left(1 - \frac{r_s}{r_p}\right)^{-1} \left(\frac{2a}{2a-r}\right)\right]^{1/2}. \quad (19)$$

At  $r = r_p$ , we have

$$v_{r,p} \simeq 0 \quad (20)$$

$$v_p \simeq v_{\phi,p} \simeq c \left(\frac{1+e}{2}\right)^{1/2} \left(\frac{r_p}{r_s}\right)^{-1/2} \left(1 - \frac{r_s}{r_p}\right)^{1/2} \quad (21)$$

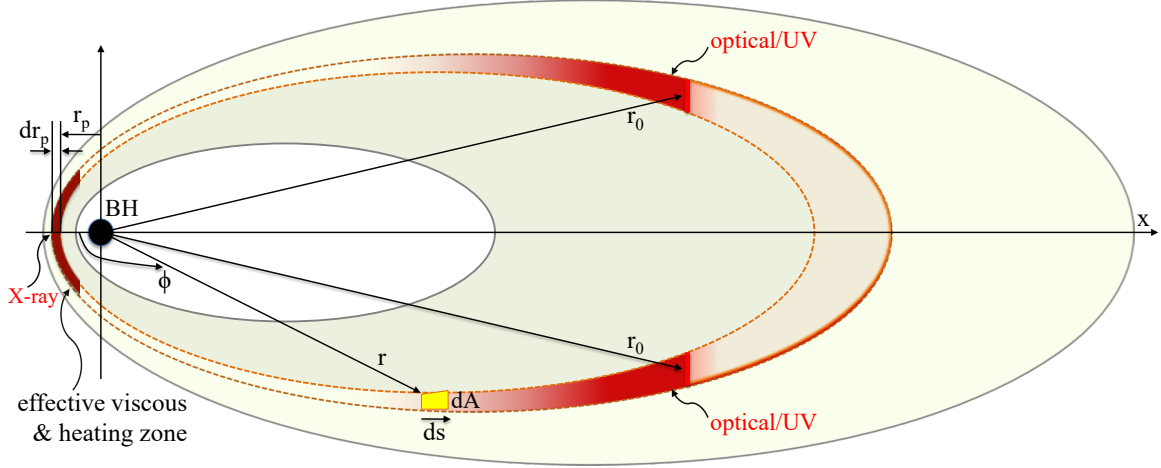


**Figure 1.** Schematics of an elliptical accretion disk. The effective viscous and heating zone is the region at the pericenter and nearby with  $r \sim r_p$  and  $-\pi/2 \lesssim \phi \lesssim \pi/2$ . Soft X-ray photons are produced in the heating zone and are trapped inside the disk because of large electron scattering opacity. They are absorbed owing to bound-free and free-free opacities and reprocessed into emission lines and low-frequency continuum via recombinations and bremsstrahlung radiation. The low-frequency continuum is emitted mainly at radiation radius  $r \lesssim r_0$ . The low-frequency photons become trapped at radius  $r > r_0$  and advected through the apocenter and back to the radiation radius  $r \lesssim r_0$  because of the large bound-free and free-free opacities. No significant radiation is emitted from the disk area with  $r > r_0$ .

and

$$\Omega_p \simeq \left( \frac{1+e}{2} \right)^{1/2} \left( 1 - \frac{r_S}{r_p} \right)^{1/2} \left( \frac{r_S}{r_p} \right)^{3/2} \frac{c}{r_S}. \quad (22)$$

## 2.2. Effective viscous torque and heating mechanisms

When the newly inflowing fluid stream intersects the post-pericenter outflowing matter at apocenter because of the general relativistic apsidal precession, the self-intersection of the streams forms shocks and would convert a fraction of the orbital kinetic energy into heat. In their elliptical accretion disk model, Piran et al. (2015) proposed that the observed luminosity of the optical/UV light of TDEs is powered by the self-crossing shocks at about apocenter at the formation of an elliptical accretion disk rather than during the subsequent accretion of matter onto the BH. For the elliptical accretion disk model of roughly uniform eccentricity proposed by Liu et al. (2017), optical/UV TDEs are powered by the accretion of matter onto the BH, and the radiation emitted by the self-crossing shocks is small (Liu et al. 2017; Cao et al. 2018; Zhou et al. 2021). The energy of the orbital kinetic dissipated by the self-crossing shocks at formation of the elliptical accretion disk is  $\Delta e_{\text{sh}} \simeq e_G(a_d) - e_G(a_{\text{mb}}) \lesssim e_G(a_d) \sim e_G(a_{\text{mb}})$  for  $a_d \sim a_{\text{mb}}$ , where  $e_G(a_d)$  and  $e_G(a_{\text{mb}})$  are given by equation (13) for semimajor axis  $a_d$  and  $a_{\text{mb}}$ , respectively. Comparing the energy  $\Delta e_{\text{sh}}$  with the total radiation of an elliptical accretion disk of uniform eccentricity,  $\Delta e_{\text{tot}} \simeq e_G(a_{\text{in}})$ , we have  $\Delta e_{\text{sh}}/\Delta e_{\text{tot}} \lesssim a_{\text{in}}/a_{\text{mb}} \lesssim r_{\text{ms}}/r_{\text{p}^*}$ . For a typical tidal disruption of star with orbital pericenter  $r_{\text{p}^*} \sim r_t \sim 23r_S$ , we have  $\Delta e_{\text{sh}}/\Delta e_{\text{tot}} \lesssim 1/10$ . Taking into account that a fraction of the kinetic energy dissipated by the self-crossing shocks may be converted back to kinetic energy by adiabatic expansion (Jiang et al. 2016), we could neglect the radiation of the self-crossing shocks and assume that the optical/UV TDEs are powered by the accretion of matter onto the BH. Because no significant

intersection shock is expected for the eccentric ellipse with semimajor  $a < a_d$ , it is reasonable to assume that no strong shock forms at apocenter of the eccentric ellipse with  $a_{\text{in}} \leq a \leq a_d$  and that the eccentric ellipse of the elliptical accretion disk is symmetric with respect to the major axis.

At the pericenter region, the streams in different orbital planes in the  $z$ -direction converge to form a "nozzle shock" (Evans & Kochanek 1989; Kochanek 1994; Ogilvie & Barker 2014; Shiokawa et al. 2015), which is too weak to be important for the stream circularization but strong enough to heat the matter to radiate in soft X-rays (Guillochon et al. 2014; Krolik et al. 2016). In addition to the convergence nozzle shock, interaction shocks would be introduced at about pericenter by the relativistic apsidal precession of the orbits and dissipate some part of the orbital kinetic into heat (Svirski et al. 2017; Chan et al. 2018). The MRI evolves differently in an eccentric accretion disk, and the strong magnetic stresses can be efficiently developed (Chan et al. 2018). The strong shear viscous torques in the pericenter region would efficiently dissipate the orbital energy (Svirski et al. 2017; Chan et al. 2018). Both the nozzle and interaction shocks and the shear viscous torques work together to efficiently dissipate the orbital kinetic energy and transfer angular momentum outward at pericenter and nearby (Svirski et al. 2017; Chan et al. 2018).

Because of the complexity and the nonlinearity of the physical processes at pericenter and nearby with  $r \sim r_p$  (Svirski et al. 2017; Chan et al. 2018), we do not discuss the physical processes and the structures of density, pressure, temperature, and entropy in that region. Instead, we assume that the physics effects of the transfer of the angular momentum and the dissipation of kinetic energy can be approximated with effective shear viscous torque at the pericenter and nearby and the complexity and uncertainties can be effectively absorbed by the viscosity parameter  $\alpha$  as for those in the standard thin  $\alpha$ -disk (Shakura & Sunyaev 1973). In a geometrically thin elliptical accretion disk, the velocity in the  $z$ -direction is much smaller than the azimuthal velocity at pericenter and the nozzle shock is weak. The energy dissipation and the angular momentum at the pericenter and nearby are dominated by the magnetic stresses, and the assumption of the effective shear viscous torque would be reasonable. We approximate the effective viscosity with a step function:  $\alpha = \alpha_p$  for  $r \sim r_p$  and  $-\pi/2 \lesssim \phi \lesssim \pi/2$ , and  $\alpha = 0$  for  $r \gg r_p$ . We call the pericenter and nearby the "heating zone." The "heating zone" generates the soft X-ray photons, and has a radial size  $r \sim r_p$ , and extends azimuthally between  $-\pi/2 \lesssim \phi \lesssim \pi/2$ , as is schematically shown in Figure 1.

### 3. MASS CONSERVATION

We consider a vertically integrated quasi-stationary elliptical accretion disk. We assume that the radius of the apocenter  $r_{\text{ap}}$  is much larger than the pericenter  $r_p$ ,  $r_{\text{ap}}/r_p \gg 1$  or specifically  $e \gtrsim 0.6$ . The mass element of disk material at radius  $(r, \phi)$  along an arbitrary ellipse lying between  $a$  and  $a + da$  for  $a_{\text{in}} \leq a \leq a_d$  is

$$dM = 2H\rho dA ds = \Sigma dA ds, \quad (23)$$

where  $\rho$  is the mass density on the midplane of the disk,  $H$  is the disk half-thickness in the  $z$ -direction,  $\Sigma = 2H\rho$  is the surface density of the accretion disk,  $ds$  is the arc-length element along the fluid streamline, and  $dA$  is the cross section of the ellipse between  $a$  and  $a + da$  at radius  $r$  (see Fig. 1). In the cylindrical coordinates  $(r, \phi, z)$ , the vector arc-length element in the disk equatorial plane is  $d\vec{s} = (\partial s/\partial r)dr\vec{e}_r + (\partial s/\partial \phi)d\phi\vec{e}_\phi$ . From Equation (8), we have the arc-length element

$$ds = \left(\frac{1+e}{2}\right)^{-1/2} \left(\frac{r}{r_p}\right)^{3/2} \left(1 - \frac{r}{2a}\right)^{1/2} r_p d\phi, \quad (24)$$

or

$$ds = \left[ 1 - \left( \frac{1+e}{2} \right) \left( \frac{r_p}{r} \right) \left( 1 - \frac{r}{2a} \right)^{-1} \right]^{-1/2} dr, \quad (25)$$

and the cross section of the stream lines

$$\begin{aligned} dA &= \frac{dr \times rd\phi}{\sqrt{(dr)^2 + (rd\phi)^2}} \\ &= \left( \frac{1+e}{2} \right)^{1/2} \left( \frac{r}{r_p} \right)^{1/2} \left( 1 - \frac{r}{2a} \right)^{-1/2} dr_p. \end{aligned} \quad (26)$$

From Equations (24) and (26), we have

$$dAds = \left( \frac{r}{r_p} \right)^2 r_p dr_p d\phi, \quad (27)$$

or from Equations (25) and (26) we have

$$\begin{aligned} dAds &= \left( \frac{1+e}{2} \right)^{1/2} \left( \frac{r}{r_p} \right)^{1/2} \left( 1 - \frac{r}{2a} \right)^{-1/2} \times \\ &\quad \left[ 1 - \left( \frac{1+e}{2} \right) \left( \frac{r_p}{r} \right) \left( 1 - \frac{r}{2a} \right)^{-1} \right]^{-1/2} dr_p dr. \end{aligned} \quad (28)$$

Equations (23) and (27) give

$$dM = \Sigma \left( \frac{r}{r_p} \right)^2 r_p dr_p d\phi \quad (29)$$

and

$$\Delta M = \oint_a \Sigma dAds = \frac{dr_p}{r_p} \oint_a \Sigma r^2 d\phi, \quad (30)$$

where the integration is around the ellipse of semimajor axis  $a$ . The conservation of mass around the ellipse between  $a$  and  $a + da$  reads

$$\begin{aligned} \frac{\partial \Delta M}{\partial t} &= \oint_{a+da} \Sigma v_a ds - \oint_a \Sigma v_a ds \\ &= da \times \frac{\partial}{\partial a} \oint_a \Sigma v_a ds, \end{aligned} \quad (31)$$

where  $v_a = da/dt$  is the radial drift velocity of matter and is a function of position  $(r, \phi)$ . For a quasi-stationary elliptical accretion disk,

$$\frac{\partial \Delta M}{\partial t} = 0 \quad (32)$$

and

$$da \times \frac{\partial}{\partial a} \oint_a \Sigma v_a ds = 0. \quad (33)$$

From equation (33), we have

$$\oint_a \Sigma v_a ds = \text{constant}. \quad (34)$$

We define the mass accretion rate of an elliptical disk as

$$\dot{M} \equiv - \oint_a \Sigma v_a ds. \quad (35)$$

## 4. ANGULAR MOMENTUM CONSERVATION

In an elliptical accretion disk, the angular momentum is constant along the streamline of semimajor axis  $a$  and eccentricity  $e$ . The vertically integrated torque per  $ds$  arc length along the ellipse with semimajor axis  $a$  is

$$d\vec{\mathcal{G}} = -2Hr\vec{\sigma} \cdot d\vec{s}, \quad (36)$$

where  $\vec{\sigma}$  is the shear stress tensor. The total torque exerted on the outer ring by the inner ring is given by

$$\begin{aligned} \mathcal{G}(a) &= - \oint_a \frac{d\mathcal{G}}{ds} ds \\ &\simeq \int_{-\pi/2}^{\pi/2} 2Hr\rho\nu \left[ \frac{1}{r} \frac{\partial v_r}{\partial \phi} + r \frac{\partial \Omega}{\partial r} \right] \left( \frac{\partial s}{\partial \phi} \right) d\phi \\ &\simeq \int_{-\pi/2}^{\pi/2} r\nu\Sigma \left[ \frac{1}{r} \frac{\partial v_r}{\partial \phi} + r \frac{\partial \Omega}{\partial r} \right] \left( \frac{1+e}{2} \right)^{-1/2} \left( \frac{r}{r_p} \right)^{3/2} \left( 1 - \frac{r}{2a} \right)^{1/2} r_p d\phi \\ &\simeq \int_{-\pi/2}^{\pi/2} r\nu\Sigma \left[ \frac{1}{r} \frac{\partial v_r}{\partial r} \left( \frac{re \sin \phi}{1+e \cos \phi} \right) + r \frac{\partial \Omega}{\partial r} \right] \times \\ &\quad \left( \frac{1+e}{2} \right)^{-1/2} \left( \frac{r}{r_p} \right)^{3/2} \left( 1 - \frac{r}{2a} \right)^{1/2} r_p d\phi, \end{aligned} \quad (37)$$

where  $\nu$  is the effective kinematic viscous coefficient and the integration is along the ellipse with  $r$  given by equation (8). In equation (37), we neglected the bulk component of viscosity  $\sigma_{rr}$ , because for the geometrically thin elliptical accretion disk the vertical velocity is small, and the compressing "nozzle shocks" are weak and negligible in dissipation of the orbital kinetic energy, and the turbulent shear viscosity is dominating (See Section 2.2 for more discussion). We adopt the standard  $\alpha$ -prescription for the kinematic viscous coefficient  $\nu = \alpha c_s H$ , with  $c_s$  the sound speed at  $r$  (Shakura & Sunyaev 1973), and a step function for the effective viscosity parameter,  $\alpha = \alpha_p$  for  $r \sim r_p$  and  $\alpha = 0$  for  $r \gg r_p$ . From equation (37), we have

$$\begin{aligned} \mathcal{G}(a) &\simeq \nu_p \Sigma_p r_p^2 \left( r_p \frac{\partial \Omega_p}{\partial r_p} \right) \Delta\phi \\ &\simeq \nu_p \Sigma_p r_p^2 \left( r_p \frac{\partial \Omega_p}{\partial r_p} \right) \pi, \end{aligned} \quad (38)$$

where  $\nu_p$  and  $\Sigma_p$  are, respectively, the kinematic viscous coefficient and the surface mass density of a disk at pericenter  $r \simeq r_p = (1-e)a$ . In equation (38), we adopt  $\Delta\phi \sim \pi$ . However, we will show that our results are insensitive to the exact value of  $\Delta\phi$ . From equations (38) and (22), we have

$$\mathcal{G}(a) \simeq -\frac{3}{2}\pi D_p \nu_p \Sigma_p r_p^2 \Omega_p, \quad (39)$$

where  $D_p = 1 - \frac{1}{3} \left( \frac{r_s}{r_p} \right) \left( 1 - \frac{r_s}{r_p} \right)^{-1}$ .

The net torque on an ellipse of a gas streamline per unit arc length between  $a$  and  $a + da$  (or between  $r_p$  and  $r_p + dr_p$  at pericenter) is

$$d\mathcal{G} = \frac{d\mathcal{G}(a+da)}{ds} - \frac{d\mathcal{G}(a)}{ds}$$

$$= \frac{\partial}{\partial A} \left( \frac{\partial \mathcal{G}}{\partial s} \right) dA. \quad (40)$$

Because the angular momentum per  $ds$  arc length along the streamline is

$$dL = l_G \Sigma ds dA, \quad (41)$$

we have the total angular momentum of the ellipse between  $a$  and  $a + da$

$$\begin{aligned} \Delta L &= \oint_a l_G \Sigma ds dA \\ &= \frac{dr_p}{r_p} \oint_a l_G \Sigma r^2 d\phi. \end{aligned} \quad (42)$$

The conservation of angular momentum gives

$$\frac{\partial(\Delta L)}{\partial t} = \oint_a l_G \Sigma v_a ds - \oint_{a+da} l_G \Sigma v_a ds + \oint_a \left( \frac{\partial^2 \mathcal{G}}{\partial s \partial A} \right) ds dA. \quad (43)$$

For quasi-stationary accretion disk  $\partial(\Delta L)/\partial t = 0$ , we have

$$-da \times \frac{\partial}{\partial a} \oint_a l_G \Sigma v_a ds + da \times \frac{\partial}{\partial a} \oint_a \left( \frac{\partial \mathcal{G}}{\partial s} \right) ds = 0. \quad (44)$$

Integrating equation (44), we have

$$\begin{aligned} \oint_a l_G \Sigma v_a ds &= \oint_a \left( \frac{\partial \mathcal{G}}{\partial s} \right) ds + C \\ &= \mathcal{G}(a) + C, \end{aligned} \quad (45)$$

where  $C$  is the integration constant. Because  $l_G$  is constant around the ellipse of semimajor axis  $a$ , we have

$$\begin{aligned} \oint_a l_G \Sigma v_a ds &= l_G \oint_a \Sigma v_a ds \\ &= l_G (-\dot{M}). \end{aligned} \quad (46)$$

From equations (45) and (46), we have

$$-l_G \dot{M} = \mathcal{G}(a) + C. \quad (47)$$

When the disk fluids migrate toward the BH and the orbital pericenter of the fluids reaches the marginally stable orbit  $r_{ms}$ , the matter passing through  $r_{ms}$  falls freely onto the BH (Abramowicz et al. 1978). For a parabolic orbit with  $e = 1$ ,  $r_{ms} = 2r_S$ , and for a circular orbit  $r_{ms} = 3r_S$ . For an elliptical orbit with  $0 < e < 1$ , we have  $2r_S < r_{ms} < 3r_S$ . We adopt the corresponding elliptical orbit of fluid as the inner edge of the elliptical accretion disk and take the simple inner boundary condition  $\mathcal{G}_{in} = \mathcal{G}(a_{in}) = 0$ , where  $a_{in} = r_{ms}/(1 - e)$  is the semimajor axis of the inner boundary of an elliptical accretion disk. From equation (12), we have the specific orbital angular momentum of the fluid at the inner boundary

$$l_{in} = l_G(a_{in})$$

$$\simeq \left(\frac{1+e}{2}\right)^{1/2} \left(\frac{r_{\text{ms}}}{r_{\text{S}}}\right)^{1/2} \left(1 - \frac{r_{\text{S}}}{r_{\text{ms}}}\right)^{-1/2} r_{\text{S}} c \quad (48)$$

From the inner boundary condition, equation (47) gives

$$\mathcal{G}(a) = -\dot{M} l_{\text{G}} \left(1 - \frac{l_{\text{in}}}{l_{\text{G}}}\right). \quad (49)$$

From equations (39) and (49), we have

$$\nu_{\text{p}} \Sigma_{\text{p}} = \frac{2\dot{M}}{3\pi} f C_{\text{p}}^{-1} D_{\text{p}}^{-1}, \quad (50)$$

where  $C_{\text{p}} = 1 - (r_{\text{S}}/r_{\text{p}})$  and

$$f = 1 - \frac{l_{\text{in}}}{l_{\text{G}}} \simeq 1 - \left(\frac{r_{\text{ms}}}{r_{\text{p}}}\right)^{1/2} \left[\frac{1 - (r_{\text{S}}/r_{\text{ms}})}{1 - (r_{\text{S}}/r_{\text{p}})}\right]^{-1/2}. \quad (51)$$

## 5. HEAT GENERATION IN THE PERICENTER REGION

The net torque on an ellipse of a gas streamline per unit arc length

$$d\mathcal{G} = \frac{\partial}{\partial A} \left(\frac{\partial \mathcal{G}}{\partial s}\right) dA. \quad (52)$$

(see Equation (40)) is acting on the ring of gas per  $ds$  arc length at radius  $r$  in the sense of angular velocity  $\Omega(a, r)$  and dissipates the orbital kinetic energy at a rate of work

$$\begin{aligned} d^2 Q^+ &= \vec{\Omega} \cdot d\vec{\mathcal{G}} \\ &= \frac{\partial}{\partial A} \left(\vec{\Omega} \cdot \frac{\partial \vec{\mathcal{G}}}{\partial s} ds\right) dA - \left(\frac{\partial \vec{\mathcal{G}}}{\partial s} ds\right) \cdot \left(\frac{\partial \vec{\Omega}}{\partial A}\right) dA \\ &\simeq \nu \Sigma r \left(\frac{1}{r} \frac{\partial v_r}{\partial \phi} + r \frac{\partial \Omega}{\partial r}\right) \left(\frac{\partial \Omega}{\partial A}\right) \left(\frac{\partial s}{\partial \phi}\right) d\phi dA, \end{aligned} \quad (53)$$

where  $\left[\partial \left(\vec{\Omega} \cdot \frac{\partial \vec{\mathcal{G}}}{\partial s}\right) / \partial A\right] dA$  is the convection term of the rotational energy through the gas by the torques, is determined solely by the inner and outer disk edges, and does not contribute to the local rate of loss of mechanical energy to the gas. We drop it from the equation. The total viscous dissipation rate within the gas between  $a$  and  $a + da$  caused by the effective viscous torques is

$$\begin{aligned} \Delta Q^+ &= \oint_a d^2 Q^+ \\ &= \oint_a dA \cdot \left[\nu \Sigma r \left(\frac{1}{r} \frac{\partial v_r}{\partial \phi} + r \frac{\partial \Omega}{\partial r}\right) \left(\frac{\partial \Omega}{\partial A}\right) \left(\frac{\partial s}{\partial \phi}\right) d\phi\right]. \end{aligned} \quad (54)$$

Because  $\nu \sim \nu_{\text{p}}$  for  $r \sim r_{\text{p}}$  and  $\nu \sim 0$  for  $r \gg r_{\text{p}}$ , equation (54) gives

$$\Delta Q^+ \simeq \nu_{\text{p}} \Sigma_{\text{p}} r_{\text{p}} \left(r_{\text{p}} \frac{\partial \Omega_{\text{p}}}{\partial r_{\text{p}}}\right)^2 \Delta \phi dr_{\text{p}}$$

$$\simeq \frac{9}{4}\pi D_p^2 \nu_p \Sigma_p r_p \Omega_p^2 dr_p, \quad (55)$$

where  $r_p (\partial\Omega_p/\partial r_p) \simeq -\frac{3}{2}D_p\Omega_p$  and  $\Delta\phi \sim \pi$ .

Equations (55) and (50) give

$$\begin{aligned} \Delta Q^+ &\simeq \frac{3}{2}\dot{M}fD_pC_p^{-1}r_p\Omega_p^2 dr_p \\ &\simeq \frac{3}{2}fD_p \left[ \frac{(1+e)r_S c^2}{2r_p^2} \right] \dot{M} dr_p, \end{aligned} \quad (56)$$

which is independent of  $\Delta\phi$  and depends on the radial distribution of  $\Omega$  and angular momentum  $l_G$  at  $r \sim r_p$ , and on the assumption of uniform eccentricity. With the Eddington luminosity

$$L_{\text{Edd}} = \frac{4\pi GM_{\text{BH}}c}{\kappa_{\text{es}}} = 1.44 \times 10^{44} M_6 \text{ erg s}^{-1}, \quad (57)$$

we define the critical accretion rate

$$\dot{M}_{\text{Edd}} = \frac{L_{\text{Edd}}}{0.1c^2} = \frac{20\pi r_S c}{\kappa_{\text{es}}} \simeq 2.54 \times 10^{-2} M_6 M_{\odot} \text{ yr}^{-1}, \quad (58)$$

where  $\kappa_{\text{es}} = 0.2(1+X) \text{ cm}^2 \text{ g}^{-1} = 0.348 \text{ cm}^2 \text{ g}^{-1}$  is the electron scattering opacity of fully ionized plasma of solar abundance. We adopt the solar abundance of the mass fractions of hydrogen, helium, and metallicity, respectively,  $X = 0.740$ ,  $Y = 0.2466$ , and  $Z = 0.0134$  (Asplund et al. 2009). The viscous dissipation heating rate of energy at  $r \sim r_p$  is

$$\Delta Q^+ \simeq \left[ \frac{30\pi}{\kappa_{\text{es}}} f \right] D_p \left( \frac{1+e}{2} \right) \left( \frac{r_S}{r_p} \right)^2 \left( \frac{\dot{M}}{\dot{M}_{\text{Edd}}} \right) c^3 dr_p. \quad (59)$$

It is well known that although the Eddington luminosity depends only on the mass of an SMBH (Eddington 1918), the Eddington accretion rate is a function of both the mass of an SMBH and the radiation efficiency  $\eta$ . The radiation efficiency of a circular accretion disk in AGNs and X-ray BH binaries is typically  $\eta \simeq 0.1$ , and the corresponding critical accretion rate  $\dot{M}_{\text{Edd}}$  is also called the Eddington accretion rate in the literature. However, the radiation efficiency of TDEs inferred from TDE observations is about  $\eta \simeq 2.7 \times 10^{-3}$  and much smaller than the typical value in AGNs and galactic BH X-ray binaries (Piran et al. 2015; Liu et al. 2017; Cao et al. 2018; Mockler et al. 2019; Zhou et al. 2021). The corresponding Eddington accretion rate of TDEs is about 37 times higher than the critical accretion rate of equation (58). Although the accretion rate of equation (58) may not have much physical meaning in an elliptical accretion disk, we use it to scale the accretion rate in this paper.

## 6. STRUCTURE OF THE ELLIPTICAL DISK

### 6.1. Vertical hydrostatic equilibrium and laminar flows

We discuss the hydrostatic equilibrium of an eccentric accretion disk in the  $z$ -direction. The Euler equation for the flows around the ellipse in the  $z$ -direction reads

$$(\vec{v} \cdot \nabla) v_z = -\frac{1}{\rho} \frac{\partial p}{\partial z} - \frac{\partial \Phi_G}{\partial z}, \quad (60)$$

where  $v_z$  is the vertical velocity and  $p$  is the total pressure of gas. The surface boundary condition is no mass flux to cross the disk surface, which gives

$$\frac{v_H}{v_r} \simeq \frac{\partial H}{\partial r} \simeq \frac{H}{r}, \quad (61)$$

where  $v_H$  is the velocity in the  $z$ -direction at the disk surface  $z = H$ . The vertical integration of equation (60) gives

$$\frac{v_H^2}{H} \simeq \frac{1}{\rho} \frac{p}{H} - \frac{GM_{\text{BH}}H}{r^3} \left[ 1 + \left( \frac{r_S}{r} \right) \left( 2 - \frac{r}{2a} \right) \right], \quad (62)$$

where  $p$  and  $\rho$  are, respectively, the pressure and density of the disk center. To obtain equation (62), we have neglected the terms of  $(r_S/r)^2$  or higher order in the brackets on the right-hand side related to the gravity in  $z$ -direction. Together with the surface boundary conditions, equation (62) gives

$$\frac{H}{r} \simeq \frac{c_s}{r\Omega_K} f_H^{-1/2}, \quad (63)$$

where  $c_s^2 = p/\rho$  is the isothermal sound speed,  $\Omega_K = (GM_{\text{BH}}/r^3)^{1/2}$  is the Keplerian angular velocity, and

$$f_H = 1 + \left( \frac{v_r}{r\Omega_K} \right)^2 + \left( \frac{r_S}{r} \right) \left( 2 - \frac{r}{2a} \right) \quad (64)$$

and  $f_H \sim 1$ . Equation (63) suggests that any deviation from hydrostatic equilibrium in the  $z$ -direction would be smoothed out on the timescale

$$t_z = H/c_s \simeq \frac{r}{r\Omega_K} f_H^{-1/2}. \quad (65)$$

Because of the radial movement of particles, the vertical gravity varies on the timescale

$$t_{\text{dyn}} \simeq \frac{r}{v_r}. \quad (66)$$

To respond to the variations of vertical gravity and establish hydrostatic equilibrium,  $t_z \ll t_{\text{dyn}}$  is required. Because

$$\begin{aligned} \frac{t_z}{t_{\text{dyn}}} &\simeq \frac{v_r}{r\Omega_K} f_H^{-1/2} \\ &\simeq \frac{v_r}{r\Omega_K} \left[ 1 + \left( \frac{v_r}{r\Omega_K} \right)^2 + \left( \frac{r_S}{r} \right) \left( 2 - \frac{r}{2a} \right) \right]^{-1/2} \end{aligned} \quad (67)$$

and

$$\frac{v_r}{r\Omega_K} \simeq \sqrt{2} \left( 1 - \frac{r_S}{r} \right) \left[ 1 - \frac{r}{2a} - \left( \frac{1+e}{2} \right) \left( \frac{r_p}{r} \right) \right]^{1/2}, \quad (68)$$

we have  $t_z \sim t_{\text{dyn}}$ . The vertical hydrostatic equilibrium cannot be well established in an elliptical accretion disk because of the variations of the gravitational potential in the  $z$ -direction around the ellipse. The flow is laminar in an eccentric accretion disk<sup>1</sup>. The conclusion is consistent with the results of the detailed hydrodynamic simulations (Ogilvie & Barker 2014).

<sup>1</sup> The calculations show that the assumption of vertical hydrostatic equilibrium would change little the results of the work.

The laminar flows move around the ellipse with a nearly constant opening angle

$$\tan \theta \simeq \frac{H}{r} \simeq \frac{H_p}{r_p}, \quad (69)$$

where  $H_p$  is the disk scale height at  $r \sim r_p$ . The convergence of the orbital velocity field near the pericenter strongly compresses the plasma in an elliptical accretion disk of eccentricity  $e \gtrsim 0.5$ , and the vertical gravity becomes unimportant at the shocks (Ogilvie & Barker 2014). From equation (62), we have  $v_{Hp} \simeq c_{sp}$  with  $c_{sp}$  the isothermal sound speed at  $r_p$ . We assume that the laminar flows move around the ellipse with the same velocity  $v$  within the opening angle  $\theta$ . We have

$$\frac{H}{r} \simeq \frac{H_p}{r_p} \simeq \frac{v_{Hp}}{v_p} \simeq \frac{c_{sp}}{v_p}. \quad (70)$$

### 6.2. Variation of mass density around the ellipse

The conservation of the mass around the ellipse of  $a = \text{constant}$  between semimajor axis  $a$  and  $a + da$  (or between  $r_p$  and  $r_p + dr_p$  at  $r_p$ ) gives

$$\Sigma_p v_p dr_p = \Sigma v dA \quad (71)$$

with  $\Sigma_p$  the surface density of mass at  $r_p$ , and we have

$$\begin{aligned} \Sigma &= \Sigma_p \left( \frac{v_p}{v} \right) \left( \frac{dr_p}{dA} \right) \\ &\simeq \Sigma_p C_p^{1/2} \left( 1 - \frac{r_S}{r} \right)^{-1} \left[ 1 + \left( \frac{1+e}{2} \right) \left( \frac{r_S}{r} \right) C_p^{-1} \left( 1 - \frac{r}{2a} \right)^{-1} \right]^{-1/2} \\ &\simeq \frac{\nu_p \Sigma_p}{\nu_p} C_p^{1/2} \left( 1 - \frac{r_S}{r} \right)^{-1} \left[ 1 + \left( \frac{1+e}{2} \right) \left( \frac{r_S}{r} \right) C_p^{-1} \left( 1 - \frac{r}{2a} \right)^{-1} \right]^{-1/2}. \end{aligned} \quad (72)$$

From equations (72) and (50), we have

$$\Sigma \simeq \left( \frac{2\dot{M}}{3\pi} \right) f C_p^{-1/2} D_p^{-1} \left( 1 - \frac{r_S}{r} \right)^{-1} \left[ 1 + \left( \frac{1+e}{2} \right) \left( \frac{r_S}{r} \right) C_p^{-1} \left( 1 - \frac{r}{2a} \right)^{-1} \right]^{-1/2} \nu_p^{-1} \quad (73)$$

and

$$\begin{aligned} \rho &= \frac{\Sigma}{2H} \\ &\simeq \left( \frac{\dot{M}}{3\pi} f \right) C_p^{-1/2} D_p^{-1} \left( 1 - \frac{r_S}{r} \right)^{-1} \left[ 1 + \left( \frac{1+e}{2} \right) \left( \frac{r_S}{r} \right) C_p^{-1} \left( 1 - \frac{r}{2a} \right)^{-1} \right]^{-1/2} \frac{1}{\nu_p H}. \end{aligned} \quad (74)$$

Equations (73) and (74) show that both the surface density  $\Sigma$  and mass density  $\rho$  depend on  $\Delta\phi$ , but the uncertainties due to  $\Delta\phi$  can be absorbed into the effective viscosity parameter  $\alpha_p$  through  $\nu_p = \alpha_p c_{sp} H_p$ . From equation (74), we have

$$\rho \simeq \left( \frac{\dot{M}}{3\pi \alpha_p} f \right) C_p^{-1/2} D_p^{-1} \left( 1 - \frac{r_S}{r} \right)^{-1} \left[ 1 + \left( \frac{1+e}{2} \right) \left( \frac{r_S}{r} \right) C_p^{-1} \left( 1 - \frac{r}{2a} \right)^{-1} \right]^{-1/2} \frac{v_p^2}{c_{sp}^3 r_p r}, \quad (75)$$

where we have used  $\nu_p = \alpha_p c_{\text{sp}} H_p$ ,  $H_p = (c_{\text{sp}}/v_p) r_p$ , and  $H = (c_{\text{sp}}/v_p) r$ .

For the polytropic process  $p \propto \rho^\gamma$ , with  $\gamma$  the polytropic index, we have the isothermal sound speed  $c_s^2 = p/\rho \propto \rho^{\gamma-1}$  and

$$\frac{c_{\text{sp}}}{c_s} = \left( \frac{\rho_p}{\rho} \right)^{(\gamma-1)/2}. \quad (76)$$

From equation (75), we have

$$\begin{aligned} \rho \simeq & \left( \frac{\dot{M}}{3\pi\alpha_p} f \right) C_p^{-1/2} D_p^{-1} \left( 1 - \frac{r_S}{r} \right)^{-1} \times \\ & \left[ 1 + \left( \frac{1+e}{2} \right) \left( \frac{r_S}{r} \right) C_p^{-1} \left( 1 - \frac{r}{2a} \right)^{-1} \right]^{-1/2} \frac{v_p^2}{c_s^3 r_p r} \left( \frac{\rho}{\rho_p} \right)^{3(\gamma-1)/2}. \end{aligned} \quad (77)$$

Because

$$\begin{aligned} \frac{\rho}{\rho_p} &= \left( \frac{\Sigma}{2H} \right) \left( \frac{\Sigma_p}{2H_p} \right)^{-1} \simeq \left( \frac{\Sigma}{\Sigma_p} \right) \left( \frac{r_p}{r} \right) \\ &\simeq C_p^{1/2} \left( 1 - \frac{r_S}{r} \right)^{-1} \left[ 1 + \left( \frac{1+e}{2} \right) \left( \frac{r_S}{r} \right) C_p^{-1} \left( 1 - \frac{r}{2a} \right)^{-1} \right]^{-1/2} \left( \frac{r_p}{r} \right), \end{aligned} \quad (78)$$

equation (77) gives

$$\begin{aligned} \rho \simeq & \left( \frac{\dot{M}}{3\pi\alpha_p} f \right) C_p^{(3\gamma-5)/4} D_p^{-1} \left( 1 - \frac{r_S}{r} \right)^{-(3\gamma-1)/2} \times \\ & \left[ 1 + \left( \frac{1+e}{2} \right) \left( \frac{r_S}{r} \right) C_p^{-1} \left( 1 - \frac{r}{2a} \right)^{-1} \right]^{-(3\gamma-1)/4} \frac{v_p^2}{c_s^3 r_p^2} \left( \frac{r_p}{r} \right)^{(3\gamma-1)/2}. \end{aligned} \quad (79)$$

### 6.3. Opacities and photon trapping

The electron scattering opacity becomes dominated for temperature  $T \gtrsim 10^4$  K to the soft X-ray photons (Frank et al. 2002). Because of the large optical depth in the vertical direction due to the electron scattering, the vertical diffusion timescale of soft X-ray photons is much larger than the orbital period of the ellipse (see the discussion in Section 6.6). When the soft X-ray photons generated at pericenter and nearby are advected with the fluids around the ellipse, they are well trapped and only a small fraction of photons could escape from the thin layer of the photosphere of the disk surface in the region  $r \sim r_p$ . The soft X-ray photons can be absorbed owing to bound-free (photoionization) and free-free absorptions and reprocessed into emission lines and low-frequency continuum mainly as a result of recombination and free-free emission. The optical/UV continuum and emission lines of optical/UV TDEs are powered primarily by the soft X-ray photons trapped inside the disk. Collisional excitations would make some contributions to the line emission.

Because the electron scattering increases the diffusive path of photons and increases the effective bound-free and free-free absorptions, the effective Rosseland mean opacity is

$$\kappa_{\text{eff}} \simeq \sqrt{\kappa_{\text{es}} \kappa_{\text{R}}}, \quad (80)$$

and the Kramers opacity  $\kappa_{\text{R}}$  is

$$\kappa_{\text{R}} = \kappa_0 \rho T^{-7/2}, \quad (81)$$

where  $\kappa_0$  is a constant depending on the chemical abundance of gas with  $\kappa_0 \simeq 3.9 \times 10^{22}(1 + X)(1 - Z) \text{ cm}^5 \text{ K}^{7/2} \text{ g}^{-2} \simeq 6.7 \times 10^{22} \text{ cm}^5 \text{ K}^{7/2} \text{ g}^{-2}$  for free-free opacity and  $\kappa_0 \simeq 4.3 \times 10^{25} Z(1 + X) \text{ cm}^5 \text{ K}^{7/2} \text{ g}^{-2} \simeq 1.0 \times 10^{24} \text{ cm}^5 \text{ K}^{7/2} \text{ g}^{-2}$  for bound-free opacity of gas with the solar chemical abundances. The bound-free opacity is strongly dominated over the free-free opacity. With the effective Rosseland mean opacity, we have the effective optical depth in the vertical direction

$$\tau_{\text{eff}} \simeq \kappa_{\text{eff}} \rho H \simeq (\kappa_{\text{es}} \kappa_0)^{1/2} \rho^{3/2} T^{-7/4} H \quad (82)$$

and the vertical diffusion timescale due to the effective Rosseland mean opacity

$$t_{\text{diff}} \simeq \frac{H}{c} \tau_{\text{eff}} \propto \rho^{3/2} T^{-7/4} H^2 \propto \rho^{-(7\gamma-13)/4} r^2. \quad (83)$$

From equation (75), we have the vertical diffusion timescale

$$t_{\text{diff}} \propto r^{(7\gamma-5)/4}. \quad (84)$$

Because the local dynamic timescale is

$$t_{\text{dyn}} = \frac{r}{v} \propto r^{3/2} \left(1 - \frac{r}{2a}\right)^{-1/2}, \quad (85)$$

we have the vertical diffusion time relative to the local dynamic timescale

$$\frac{t_{\text{diff}}}{t_{\text{dyn}}} \propto r^{(7\gamma-11)/4} \left(1 - \frac{r}{2a}\right)^{1/2}. \quad (86)$$

Defining the photon-trapping radius  $r_0$ , at which the vertical diffusion timescale  $t_{\text{diff}} = (H/c)\tau$  because of the effective Rosseland mean opacity equals to the dynamic timescale  $t_{\text{dyn}} = r/v$ , or

$$\left(\frac{H_0}{c}\right) \tau_0 = \frac{r_0}{v_0}, \quad (87)$$

where  $\tau_0$  and  $v_0$  are, respectively, the effective optical depth and velocity at  $r_0$ , we have

$$\frac{t_{\text{diff}}}{t_{\text{dyn}}} \simeq \left(\frac{r}{r_0}\right)^{(7\gamma-11)/4} \left[\frac{1 - \frac{r}{2a}}{1 - \frac{r_0}{2a}}\right]^{1/2}, \quad (88)$$

which for the typical polytropic index  $\gamma = 5/3$  gives

$$\frac{t_{\text{diff}}}{t_{\text{dyn}}} \simeq \left(\frac{r}{r_0}\right)^{1/6} \left[\frac{1 - \frac{r}{2a}}{1 - \frac{r_0}{2a}}\right]^{1/2}. \quad (89)$$

Equation (89) shows that the vertical diffusion timescales of low-frequency photons are smaller than the local dynamic timescale for  $r < r_0$ . Because for  $r > r_0$  the vertical diffusion timescales due to the effective Rosseland mean opacity are larger than the local dynamic timescale, the low-frequency photons are trapped inside the disk and move outward with the fluid. When the trapped photons go around through apocenter and return to  $r \leq r_0$ , they would be radiatively transported to the disk surface and emitted away. In our elliptical accretion disk model, most of the dissipation occurs in the

disk (and not at the shocks). In addition, we do not discuss the elliptical accretion disk model for super-Eddington accretion in this work, because the advection cooling of heat across the eccentric ellipse is neglected in equation (106) for energy balance. Therefore, the assumption of  $\gamma = 5/3$  or  $\sim 2$  is reasonable. We leave the discussion of the elliptical accretion disk model of the polytropic index  $\gamma = 4/3$  for super-Eddington luminosity for a future work.

We assume that the energy transfer in the  $z$ -direction is mainly due to the radiation and that the energy transports due to turbulence and thermal conductivity are small. The flux of radiant energy in the  $z$ -direction is

$$\begin{aligned} F_{\text{rad}} &= -\frac{16\sigma_{\text{SB}}T^3}{3\kappa_{\text{eff}}\rho} \frac{\partial T}{\partial z} \\ &= -\frac{16\sigma_{\text{SB}}T^4}{3} \left( \frac{1}{T} \frac{\partial T}{\partial \tau_{\text{eff}}} \right), \end{aligned} \quad (90)$$

where  $\sigma_{\text{SB}}$  is the Stefan-Boltzmann constant. Because the strong vertically compressing shock near pericenter uniformly heats the plasma, it is expected that the temperature of the shocked gas is homogeneous and the gradient of temperature in the  $z$ -direction in the region  $r \sim r_{\text{p}}$  is small,  $(\delta T/T) \sim 0$ . At  $r \sim r_{\text{p}}$ , the disk temperature is  $T \gtrsim 10^6$  K, the He II is also photonionized and the absorption due to photoionization is negligible. After the fluids move away from the heating region and expand adiabatically, the photons escape from the thin layer of photosphere of the disk surface. The typical emitted energy at radius  $r$  is

$$\begin{aligned} \Delta E^- &\simeq \sigma_{\text{SB}}T^4 t_{\text{dyn}} dA ds \\ &\propto T^4 r^{3/2} \left(1 - \frac{r}{2a}\right)^{-1/2} r^{3/2} \left(1 - \frac{r}{2a}\right)^{-1/2} dr_{\text{p}} \\ &\propto r^{-(4\gamma-7)} \left(1 - \frac{r}{2a}\right)^{-1} dr_{\text{p}}. \end{aligned} \quad (91)$$

For the polytropic index  $\gamma = 5/3$ ,  $\Delta E^- \propto r^{1/3} \left(1 - \frac{r}{2a}\right)^{-1} dr_{\text{p}}$ . The radiation emits mainly at large radii.

The emission decreases the temperature of the disk surface, and a vertical gradient of temperature propagates toward the disk center in response to the radiative cooling. For a sufficiently large vertical gradient of temperature at  $r \gg r_{\text{p}}$ , we define the radiation timescale

$$t_{\text{rad}} = \frac{H a_{\text{rad}} T^4}{\sigma_{\text{SB}} T_{\text{s}}^4}, \quad (92)$$

where  $T_{\text{s}}$  is the surface temperature of the disk and  $a_{\text{rad}} = 4\sigma_{\text{SB}}/c$  is the radiation constant. At the critical radius  $r_{\text{rad}}$ , the radiation timescale  $t_{\text{rad}}$  equals the dynamic (advection) timescale  $t_{\text{dyn,rad}}$ ,

$$\frac{H_{\text{rad}} a_{\text{rad}} T_{\text{rad}}^4}{\sigma_{\text{SB}} T_{\text{bb}}^4} = t_{\text{dyn,rad}}. \quad (93)$$

In equation (93),  $T_{\text{bb}}$  and  $T_{\text{rad}}$  are, respectively, the surface and center blackbody temperature of the disk at  $r_{\text{rad}}$ ,  $H_{\text{rad}}$  is the disk scale height at  $r_{\text{rad}}$ , and  $t_{\text{dyn,rad}} = r_{\text{rad}}/v_{\text{rad}}$  (with  $v_{\text{rad}}$  the velocity at  $r_{\text{rad}}$ ) is the dynamical timescale. For  $r \lesssim r_{\text{rad}}$ , we have  $t_{\text{rad}} \lesssim t_{\text{dyn}}$ . Whether the surface density of

radiation contents can be efficiently radiated depends on the vertical gradient of temperature, which is established by the surface cooling  $\Delta E^-$ . From equation (90), we have

$$\begin{aligned} F_{\text{rad}} &= \sigma_{\text{SB}} T_{\text{bb}}^4 \\ &\simeq -\frac{16\sigma_{\text{SB}} T^3}{3\kappa_{\text{eff,rad}}\rho_{\text{rad}}} \left( \frac{\partial T}{\partial z} \right)_{\text{rad}} \\ &\simeq \frac{4\sigma_{\text{SB}} T_{\text{rad}}^4}{3\tau_{\text{rad}}}, \end{aligned} \quad (94)$$

where  $\tau_{\text{rad}} \simeq \kappa_{\text{eff,rad}}\rho_{\text{rad}}H_{\text{rad}}$  is the vertical effective optical depth at  $r = r_{\text{rad}}$  and  $\rho_{\text{rad}}$  and  $\kappa_{\text{eff,rad}}$  are, respectively, the density and effective Rosseland mean opacity at  $r_{\text{rad}}$ . To obtain equation (94), we have assumed  $T_{\text{rad}}^4 \gg T_{\text{bb}}^4$  at  $r_{\text{rad}}$ , although we may have  $T_{\text{rad}} \gtrsim T_{\text{bb}}$ . It is reasonable that the local dynamic time at  $r \gg r_{\text{p}}$  is long for the vertical gradient of temperature to be established self-consistently in response to the surface cooling emission  $\Delta E^-$ . From equations (93) and (94), we have

$$3 \left( \frac{H_{\text{rad}}}{c} \right) \tau_{\text{rad}} = \left( \frac{r_{\text{rad}}}{v_{\text{rad}}} \right). \quad (95)$$

Equations (95) and (87) show that the radiation radius  $r_{\text{rad}}$  is slightly larger than the photon-trapping radius  $r_0$ . Because the low-frequency photons also become trapped owing to the bound-free and free-free absorptions at  $r > r_0$ , the photon-trapping radius  $r_0$  is the typical radiation radius.

At the typical radiation radius  $r_0$ , we have the velocity

$$v_0 \simeq cA_0^{1/2}C_0 \left( \frac{r_{\text{S}}}{r_0} \right)^{1/2} \left( 1 - \frac{r_0}{2a} \right)^{1/2} \quad (96)$$

with  $C_0 = 1 - \frac{r_{\text{S}}}{r_0}$  and  $A_0 = 1 + C_{\text{p}}^{-1} \left( \frac{1+e}{2} \right) \left( \frac{r_{\text{S}}}{r_0} \right) \left( 1 - \frac{r_0}{2a} \right)^{-1}$ , and the disk half-thickness

$$\begin{aligned} H_0 &= \left( \frac{c_{\text{sp}}}{v_{\text{p}}} \right) r_0 \simeq \left( \frac{c_{\text{s0}}}{v_{\text{p}}} \right) \left( \frac{\rho_{\text{p}}}{\rho_0} \right)^{(\gamma-1)/2} r_0 \\ &= \left( \frac{c_{\text{s0}}}{v_{\text{p}}} \right) C_{\text{p}}^{-(\gamma-1)/4} C_0^{(\gamma-1)/2} A_0^{(\gamma-1)/4} \left( \frac{r_0}{r_{\text{p}}} \right)^{(\gamma-1)/2} r_0, \end{aligned} \quad (97)$$

where  $p_0$  and  $\rho_0$  are, respectively, the total pressure and mass density on the midplane of the disk at  $r_0$  and  $c_{\text{s0}}^2 = p_0/\rho_0$  is the isothermal sound speed. From equation (82), we have the effective ("true") optical depth at  $r_0$

$$\tau_0 = (\kappa_{\text{es}}\kappa_0)^{1/2} \rho_0^{3/2} T_0^{-7/4} H_0 \quad (98)$$

and from equation (79) the mass density at  $r_0$

$$\rho_0 \simeq \left( \frac{\dot{M}}{3\pi\alpha_{\text{p}} f} \right) C_{\text{p}}^{(3\gamma-5)/4} D_{\text{p}}^{-1} C_0^{-(3\gamma-1)/2} A_0^{-(3\gamma-1)/4} \frac{v_{\text{p}}^2}{c_{\text{s0}}^3 r_{\text{p}}^2} \left( \frac{r_{\text{p}}}{r_0} \right)^{(3\gamma-1)/2}. \quad (99)$$

Finally, equation (87) gives the first relation of the temperature  $T_0$  and the radiation radius  $r_0$

$$T_0^{-3} \left( \frac{r_0}{r_{\text{p}}} \right)^{-(5\gamma-1)/4} \left\{ \left( \frac{\beta_{\text{g}}^{-1} k_{\text{B}}}{\mu m_{\text{H}}} \right)^{-5/4} r_{\text{S}}^{-1/2} c^{5/2} \kappa_{\text{es}}^{-1} \kappa_0^{1/2} \right\} \left( \frac{r_{\text{p}}}{r_{\text{S}}} \right)^{-3} \left( \frac{1+e}{2} \right)^{1/2} \times$$

$$C_p^{(5\gamma-7)/8} C_0^{-(5\gamma-3)/4} D_p^{-3/2} A_0^{-(5\gamma-3)/8} \left( \frac{20f}{3\alpha_p} \right)^{3/2} \left( 1 - \frac{r_0}{2a} \right)^{1/2} \left( \frac{\dot{M}}{\dot{M}_{\text{Edd}}} \right)^{3/2} = 1, \quad (100)$$

where  $\beta_g = p_g/p$  is the ratio of gas pressure to total pressure and  $\beta_g \sim 1$  in the present paper,  $k_B$  is the Boltzmann constant,  $m_H$  is the mass of hydrogen, and  $\mu$  is the mean molecular weight, with  $\mu = 0.60$  for fully ionized gas of solar chemical abundance. The equation of state for a mixture of perfect gas and radiation is adopted,

$$p = p_g + p_r = \frac{\rho k_B T}{\mu m_H} + \frac{a_{\text{rad}}}{3} T^4, \quad (101)$$

where  $p_r$  is the radiation pressure. The isothermal sound speed is

$$c_s = \left( \frac{p}{\rho} \right)^{1/2} = \beta_g^{-1/2} \left( \frac{p_g}{\rho} \right)^{1/2} = \left( \frac{\beta_g^{-1} k_B}{\mu m_H} \right)^{1/2} T^{1/2} \quad (102)$$

and

$$c_{s0} = \left( \frac{\beta_g^{-1} k_B}{\mu m_H} \right)^{1/2} T_0^{1/2}. \quad (103)$$

#### 6.4. Energy balance

In Section 6.3, we showed that the emission of radiation along the ellipse is dominated at large radius and mainly at the typical radiation radius  $r_0$  with radiation flux

$$F_{\text{rad},0} = \sigma_{\text{SB}} T_{\text{bb}}^4 \simeq \frac{4\sigma_{\text{SB}}}{3\tau_0} T_0^4. \quad (104)$$

The total cooling rate of the disk around the ellipse is

$$\Delta Q^- \simeq 2 \times 2 \times F_{\text{rad},0} \times dA \Delta s, \quad (105)$$

where  $dA = \left( \frac{1+e}{2} \right)^{1/2} \left( \frac{r_0}{r_p} \right)^{1/2} \left( 1 - \frac{r_0}{2a} \right)^{-1/2} dr_p$  and  $\Delta s \simeq \left[ 1 + \frac{1}{2} \left( \frac{1+e}{2} \right) \left( \frac{r_p}{r_0} \right) \left( 1 - \frac{r_0}{2a} \right)^{-1} \right] r_0$ . The first "2" on the right-hand side of equation (105) is due to the two sides of the disk surface, and the second "2" is because of the symmetry of the ellipse with respect to the major axis. If we assume that the energy generating rate  $\Delta Q^+$  is balanced by the radiation cooling rate  $\Delta Q^-$

$$\Delta Q^+ = \Delta Q^-, \quad (106)$$

we have

$$\left( \frac{r_0}{r_p} \right)^{3/2} \left( 1 - \frac{r_0}{2a} \right)^{-1/2} \left( \frac{\sigma_{\text{SB}} T_0^4}{\tau_0} \right) \simeq \left( \frac{45\pi}{8\kappa_{\text{es}}} f \right) \left( \frac{1+e}{2} \right)^{1/2} \left( \frac{r_p}{r_S} \right)^{-3} \times D_p B_0^{-1} r_S^{-1} c^3 \left( \frac{\dot{M}}{\dot{M}_{\text{Edd}}} \right) \quad (107)$$

with  $B_0 = 1 + \frac{1}{2} \left( \frac{1+e}{2} \right) \left( \frac{r_p}{r_0} \right) \left( 1 - \frac{r_0}{2a} \right)^{-1}$ . In equation (106), the energy generating rate is locally balanced by the radiation cooling rate, and the cooling due to the advection of heat across the eccentric

ellipse is neglected. Because the advection cooling may be important in an elliptical accretion disk of super-Eddington luminosity in TDEs, e.g., by a BH of mass  $M_{\text{BH}} \lesssim 10^5 M_{\odot}$  (see equation (143)), our results cannot be applied to such accretion systems, and an elliptical slim disk model with the advective cooling across eccentric ellipse is needed. Equations (87) and (97) give the optical depth at  $r_0$ ,

$$\begin{aligned} \tau_0 &\simeq \left(\frac{c}{v_0}\right) \left(\frac{r_0}{H_0}\right) \\ &\simeq C_{\text{p}}^{(\gamma+1)/4} C_0^{-(\gamma+1)/2} A_0^{-(\gamma+1)/4} \left(\frac{1+e}{2}\right)^{1/2} \left(1 - \frac{r_0}{2a}\right)^{-1/2} \times \\ &\quad \left\{ \left(\frac{\beta_{\text{g}}^{-1} k_{\text{B}}}{\mu m_{\text{H}}}\right)^{-1/2} c \right\} T_0^{-1/2} \left(\frac{r_0}{r_{\text{p}}}\right)^{-(\gamma-2)/2}. \end{aligned} \quad (108)$$

From Equations (107) and (108), we obtain the second relation of the temperature  $T_0$  and the radiation radius  $r_0$ ,

$$\begin{aligned} \frac{r_0}{r_{\text{p}}} &\simeq T_0^{-9/(\gamma+1)} \left(\frac{45\pi}{8} f\right)^{2/(\gamma+1)} \left(\frac{1+e}{2}\right)^{2/(\gamma+1)} \times \\ &\quad A_0^{-1/2} B_0^{-2/(\gamma+1)} C_0^{-1} C_{\text{p}}^{1/2} D_{\text{p}}^{2/(\gamma+1)} \times \\ &\quad \left\{ \left(\frac{\beta_{\text{g}}^{-1} k_{\text{B}}}{\mu m_{\text{H}}}\right)^{-1/(\gamma+1)} \sigma_{\text{SB}}^{-2/(\gamma+1)} \kappa_{\text{es}}^{-2/(\gamma+1)} r_{\text{S}}^{-2/(\gamma+1)} c^{8/(\gamma+1)} \right\} \times \\ &\quad \left(\frac{r_{\text{p}}}{r_{\text{S}}}\right)^{-6/(\gamma+1)} \left(\frac{\dot{M}}{\dot{M}_{\text{Edd}}}\right)^{2/(\gamma+1)}. \end{aligned} \quad (109)$$

### 6.5. Radiation radius and physics of the disk at $r_0$

From equations (100) and (109), we obtain the temperature of the disk center at  $r_0$  as a function of pericenter  $r_{\text{p}}$  and accretion rate  $\dot{M}$ ,

$$\begin{aligned} T_0 &\simeq A_0^{-(\gamma+1)/(33\gamma-21)} B_0^{-2(5\gamma-1)/(33\gamma-21)} C_{\text{p}}^{3(\gamma+1)/(33\gamma-21)} C_0^{-2(\gamma+1)/(33\gamma-21)} D_{\text{p}}^{4(4\gamma+1)/(33\gamma-21)} \times \\ &\quad \left(\frac{45\pi}{8} f\right)^{2(5\gamma-1)/(33\gamma-21)} \left(\frac{20}{3\alpha_{\text{p}}} f\right)^{-6(\gamma+1)/(33\gamma-21)} \left(\frac{1+e}{2}\right)^{4(2\gamma-1)/(33\gamma-21)} \times \\ &\quad \left\{ \left(\frac{\beta_{\text{g}}^{-1} k_{\text{B}}}{\mu m_{\text{H}}}\right)^{6/(33\gamma-21)} \sigma_{\text{SB}}^{-2(5\gamma-1)/(33\gamma-21)} \kappa_{\text{es}}^{-6(\gamma-1)/(33\gamma-21)} r_{\text{S}}^{-4(2\gamma-1)/(33\gamma-21)} c^{6(5\gamma-3)/(33\gamma-21)} \right. \\ &\quad \left. \kappa_0^{-2(\gamma+1)/(33\gamma-21)} \right\} \beta_*^{18(\gamma-1)/(33\gamma-21)} \left(\frac{r_{\text{t}}}{r_{\text{S}}}\right)^{-18(\gamma-1)/(33\gamma-21)} \left(\frac{r_{\text{p}}}{r_{\text{p}^*}}\right)^{-18(\gamma-1)/(33\gamma-21)} \times \\ &\quad \left(1 - \frac{r_0}{2a}\right)^{-2(\gamma+1)/(33\gamma-21)} \left(\frac{\dot{M}_{\text{p}}}{\dot{M}_{\text{Edd}}}\right)^{4(\gamma-2)/(33\gamma-21)} \left(\frac{\dot{M}}{\dot{M}_{\text{p}}}\right)^{4(\gamma-2)/(33\gamma-21)}, \end{aligned} \quad (110)$$

and from equations (109) and (110), we have the radiation radius

$$\frac{r_0}{r_{\text{p}}} \simeq A_0^{-(11\gamma-13)/2(11\gamma-7)} B_0^{8/(11\gamma-7)} C_{\text{p}}^{(11\gamma-25)/2(11\gamma-7)} C_0^{-(11\gamma-13)/(11\gamma-7)} D_{\text{p}}^{-26/(11\gamma-7)} \times$$

$$\begin{aligned}
& \left( \frac{45\pi}{8} f \right)^{-8/(11\gamma-7)} \left( \frac{20}{3\alpha_p} f \right)^{18/(11\gamma-7)} \left( \frac{1+e}{2} \right)^{-2/(11\gamma-7)} \times \\
& \left\{ \left( \frac{\beta_g^{-1} k_B}{\mu m_H} \right)^{-11/(11\gamma-7)} \sigma_{\text{SB}}^{8/(11\gamma-7)} \kappa_{\text{es}}^{-4/(11\gamma-7)} r_{\text{S}}^{2/(11\gamma-7)} c^{-2/(11\gamma-7)} \kappa_0^{6/(11\gamma-7)} \right\} \times \\
& \beta_*^{12/(11\gamma-7)} \left( \frac{r_t}{r_{\text{S}}} \right)^{-12/(11\gamma-7)} \left( \frac{r_p}{r_{p*}} \right)^{-12/(11\gamma-7)} \left( 1 - \frac{r_0}{2a} \right)^{6/(11\gamma-7)} \times \\
& \left( \frac{\dot{M}_p}{\dot{M}_{\text{Edd}}} \right)^{10/(11\gamma-7)} \left( \frac{\dot{M}}{\dot{M}_p} \right)^{10/(11\gamma-7)}, \tag{111}
\end{aligned}$$

where we have used

$$\frac{r_p}{r_{\text{S}}} = \beta_*^{-1} \left( \frac{r_p}{r_{p*}} \right) \left( \frac{r_t}{r_{\text{S}}} \right) \tag{112}$$

for  $r_{\text{ms}} \leq r_p \leq r_{p*}$  and

$$\frac{\dot{M}}{\dot{M}_{\text{Edd}}} = \left( \frac{\dot{M}}{\dot{M}_p} \right) \left( \frac{\dot{M}_p}{\dot{M}_{\text{Edd}}} \right). \tag{113}$$

Equations (110) and (111) become, respectively,

$$\begin{aligned}
T_0 & \simeq A_0^{-(\gamma+1)/(33\gamma-21)} B_0^{-2(5\gamma-1)/(33\gamma-21)} C_p^{3(\gamma+1)/(33\gamma-21)} C_0^{-2(\gamma+1)/(33\gamma-21)} D_p^{4(4\gamma+1)/(33\gamma-21)} \times \\
& f^{4(\gamma-2)/(33\gamma-21)} \left( \frac{45\pi}{8} \right)^{2(5\gamma-1)/(33\gamma-21)} \left( \frac{20}{3} \right)^{-6(\gamma+1)/(33\gamma-21)} \alpha_p^{6(\gamma+1)/(33\gamma-21)} \times \\
& \left( \frac{1+e}{2} \right)^{4(2\gamma-1)/(33\gamma-21)} \left\{ \left( \frac{\beta_g^{-1} k_B}{\mu m_H} \right)^{6/(33\gamma-21)} \sigma_{\text{SB}}^{-2(5\gamma-1)/(33\gamma-21)} \kappa_{\text{es}}^{-6(\gamma-1)/(33\gamma-21)} \times \right. \\
& \left. r_{11}^{-4(2\gamma-1)/(33\gamma-21)} c^{6(5\gamma-3)/(33\gamma-21)} \kappa_0^{-2(\gamma+1)/(33\gamma-21)} \right\} 23.545^{-18(\gamma-1)/(33\gamma-21)} \times \\
& f_{\text{T}}^{-6(5\gamma-7)/(33\gamma-21)} m_*^{2(7\gamma-11)/(33\gamma-21)} r_*^{-6(4\gamma-5)/(33\gamma-21)} \beta_*^{18(\gamma-1)/(33\gamma-21)} 117^{4(\gamma-2)/(33\gamma-21)} \times \\
& M_6^{-2(\gamma-2)/(33\gamma-21)} \left[ \frac{3(n-1)}{2} \right]^{4(\gamma-2)/(33\gamma-21)} \left( 1 - \frac{r_0}{2a} \right)^{-2(\gamma+1)/(33\gamma-21)} \times \\
& \left( \frac{r_p}{r_{p*}} \right)^{-18(\gamma-1)/(33\gamma-21)} \left( \frac{\dot{M}}{\dot{M}_p} \right)^{4(\gamma-2)/(33\gamma-21)} \tag{114}
\end{aligned}$$

and

$$\begin{aligned}
\frac{r_0}{r_{p*}} & \simeq A_0^{-(11\gamma-13)/2(11\gamma-7)} B_0^{8/(11\gamma-7)} C_p^{(11\gamma-25)/2(11\gamma-7)} C_0^{-(11\gamma-13)/(11\gamma-7)} D_p^{-26/(11\gamma-7)} \times \\
& f^{10/(11\gamma-7)} \alpha_p^{-18/(11\gamma-7)} \left( \frac{45\pi}{8} \right)^{-8/(11\gamma-7)} \left( \frac{20}{3} \right)^{18/(11\gamma-7)} \left( \frac{1+e}{2} \right)^{-2/(11\gamma-7)} \times \\
& \left\{ \left( \frac{\beta_g^{-1} k_B}{\mu m_H} \right)^{-11/(11\gamma-7)} \sigma_{\text{SB}}^{8/(11\gamma-7)} \kappa_{\text{es}}^{-4/(11\gamma-7)} r_{11}^{2/(11\gamma-7)} c^{-2/(11\gamma-7)} \kappa_0^{6/(11\gamma-7)} \right\} \times \\
& 23.545^{-12/(11\gamma-7)} f_{\text{T}}^{-42/(11\gamma-7)} m_*^{24/(11\gamma-7)} r_*^{-27/(11\gamma-7)} \beta_*^{12/(11\gamma-7)} 117^{10/(11\gamma-7)} \times \\
& M_6^{-5/(11\gamma-7)} \left[ \frac{3(n-1)}{2} \right]^{10/(11\gamma-7)} \left( 1 - \frac{r_0}{2a} \right)^{6/(11\gamma-7)} \times
\end{aligned}$$

$$\left(\frac{r_p}{r_{p*}}\right)^{(11\gamma-19)/(11\gamma-7)} \left(\frac{\dot{M}}{\dot{M}_p}\right)^{10/(11\gamma-7)}, \quad (115)$$

where  $r_{11} = r_S/M_6 = 2.954 \times 10^{11}$  cm and  $\dot{M}_p \simeq 117 [3(n-1)/2] f_T^{-3} r_*^{-3/2} m_*^2 M_6^{-3/2} \dot{M}_{\text{Edd}}$ . Note that we use  $r_0/r_{p*}$  on the left-hand side of equation (115).

For typical polytropic index  $\gamma = 5/3$ , equations (114) and (115) give, respectively,

$$\begin{aligned} T_0 &\simeq A_0^{-4/51} B_0^{-22/51} C_p^{4/17} C_0^{-8/51} D_p^{46/51} f^{-2/51} \left(\frac{45\pi}{8}\right)^{22/51} \left(\frac{20}{3}\right)^{-8/17} \alpha_p^{8/17} \times \\ &\quad \left(\frac{1+e}{2}\right)^{14/51} \left\{ \left(\frac{\beta_g^{-1} k_B}{\mu m_H}\right)^{3/17} \sigma_{\text{SB}}^{-22/51} \kappa_{\text{es}}^{-2/17} r_{11}^{-14/51} c^{16/17} \kappa_0^{-8/51} \right\} \\ &\quad 23.545^{-6/17} 117^{-2/51} f_T^{-4/17} m_*^{2/51} r_*^{-5/17} \beta_*^{6/17} M_6^{1/51} \times \\ &\quad \left[\frac{3(n-1)}{2}\right]^{-2/51} \left(1 - \frac{r_0}{2a}\right)^{-8/51} \left(\frac{r_p}{r_{p*}}\right)^{-6/17} \left(\frac{\dot{M}}{\dot{M}_p}\right)^{-2/51} \\ &\simeq 2.42 \times 10^5 \text{ (K)} A_0^{-4/51} B_0^{-22/51} C_0^{-8/51} C_p^{4/17} D_p^{46/51} \times \\ &\quad f^{-2/51} f_T^{-4/17} \alpha_{-1}^{8/17} \left(\frac{1+e}{2}\right)^{14/51} \beta_g^{-3/17} m_*^{2/51} r_*^{-5/17} \beta_*^{6/17} M_6^{1/51} \times \\ &\quad \left[\frac{3(n-1)}{2}\right]^{-2/51} \left(\frac{r_p}{r_{p*}}\right)^{-6/17} \left(1 - \frac{r_0}{2a}\right)^{-8/51} \left(\frac{\dot{M}}{\dot{M}_p}\right)^{-2/51} \end{aligned} \quad (116)$$

and

$$\begin{aligned} \frac{r_0}{r_{p*}} &\simeq A_0^{-4/17} B_0^{12/17} C_0^{-8/17} C_p^{-5/17} D_p^{-39/17} \times \\ &\quad f^{15/17} \alpha_p^{-27/17} \left(\frac{45\pi}{8}\right)^{-12/17} \left(\frac{20}{3}\right)^{27/17} \left(\frac{1+e}{2}\right)^{-3/17} \times \\ &\quad \left\{ \left(\frac{\beta_g^{-1} k_B}{\mu m_H}\right)^{-33/34} \sigma_{\text{SB}}^{12/17} \kappa_{\text{es}}^{-6/17} r_{11}^{3/17} c^{-3/17} \kappa_0^{9/17} \right\} \times \\ &\quad 23.545^{-18/17} 117^{15/17} f_T^{-63/17} m_*^{36/17} r_*^{-81/34} \beta_*^{18/17} \times \\ &\quad M_6^{-15/34} \left[\frac{3(n-1)}{2}\right]^{15/17} \left(1 - \frac{r_0}{2a}\right)^{9/17} \left(\frac{r_p}{r_{p*}}\right)^{-1/17} \left(\frac{\dot{M}}{\dot{M}_p}\right)^{15/17} \\ &\simeq 3.43 \times 10^4 A_0^{-4/17} B_0^{12/17} C_0^{-8/17} C_p^{-5/17} D_p^{-39/17} \times \\ &\quad f^{15/17} f_T^{-63/17} \alpha_{-1}^{-27/17} \left(\frac{1+e}{2}\right)^{-3/17} \beta_g^{33/34} m_*^{36/17} r_*^{-81/34} \beta_*^{18/17} \times \\ &\quad M_6^{-15/34} \left[\frac{3(n-1)}{2}\right]^{15/17} \left(1 - \frac{r_0}{2a}\right)^{9/17} \left(\frac{r_p}{r_{p*}}\right)^{-1/17} \left(\frac{\dot{M}}{\dot{M}_p}\right)^{15/17}, \end{aligned} \quad (117)$$

where  $\alpha_{-1} = \alpha_p/0.1$ . Equation (116) shows that the temperature of the disk center at the radiation radius  $r_0$  is practically independent of both the accretion rate with power-law index  $-0.039$  and BH mass with power-law index  $0.020$ , while the radiation radius  $r_0$  given by equation (117) significantly

depends on both of them. Equations (116) and (117) show that both the temperature  $T_0$  and radiation radius  $r_0$  depend on the effective viscosity parameter  $\alpha_p$ . The disk-dominated late-time UV observations of TDEs show that the disk viscosity parameter is probably in the range  $-1.1 \lesssim \log \alpha \lesssim -0.2$  with average  $\langle \log \alpha \rangle \simeq -0.46$  (see Table 3 of van Velzen et al. 2019). We notice that they adopted a circular accretion disk of radius  $2r_p$  for TDEs which is different from the disk model in this work. Because the viscous torque in an elliptical accretion disk is expected to operate efficiently only in the vicinity of the pericenter at  $r \sim r_p$  and the effective viscous and heating region would be expected to be about from  $-\pi/2 \lesssim \phi \lesssim \pi/2$  and  $r \sim r_p$ , the size of the effective viscous regions is not much different from the circular accretion disk. Taking into account the very large uncertainties of the measurements of viscosity parameters of TDEs and the simplifications adopted in this work, we do not take into account the differences of two viscosity parameters and adopt the range of viscosity parameters  $0.01 \lesssim \alpha_p \lesssim 1$  with the typical value  $\alpha_p = 0.2$ .

From equations (99), (110), and (111), we have the mass density at  $r_0$

$$\begin{aligned} \rho_0 \simeq & \left( \frac{45\pi}{8} f \right)^{(7\gamma-3)/(11\gamma-7)} \left( \frac{20}{3\alpha_p} f \right)^{-(13\gamma-5)/(11\gamma-7)} \left( \frac{1+e}{2} \right)^{2(5\gamma-3)/(11\gamma-7)} \times \\ & \left\{ A_0^{-2(2\gamma-1)/(11\gamma-7)} B_0^{-(7\gamma-3)/(11\gamma-7)} C_p^{6(2\gamma-1)/(11\gamma-7)} C_0^{-4(2\gamma-1)/(11\gamma-7)} D_p^{4(5\gamma-2)/(11\gamma-7)} \right\} \times \\ & \left\{ \left( \frac{\beta_g^{-1} k_B}{\mu m_H} \right)^{2/(11\gamma-7)} \sigma_{\text{SB}}^{-(7\gamma-3)/(11\gamma-7)} \kappa_{\text{es}}^{-2(\gamma-1)/(11\gamma-7)} r_S^{-2(5\gamma-3)/(11\gamma-7)} c^{(21\gamma-13)/(11\gamma-7)} \times \right. \\ & \left. \kappa_0^{-4(2\gamma-1)/(11\gamma-7)} \right\} \left( \frac{r_p}{r_S} \right)^{-6(\gamma-1)/(11\gamma-7)} \left( 1 - \frac{r_0}{2a} \right)^{-4(2\gamma-1)/(11\gamma-7)} \left( \frac{\dot{M}}{\dot{M}_{\text{Edd}}} \right)^{-2(3\gamma-1)/(11\gamma-7)} \end{aligned} \quad (118)$$

For  $\gamma = 5/3$ , equation (118) gives

$$\begin{aligned} \rho_0 \simeq & \left( \frac{45\pi}{8} \right)^{13/17} \left( \frac{20}{3} \right)^{-25/17} \left( \frac{1+e}{2} \right)^{16/17} f^{-12/17} \alpha_p^{25/17} \times \\ & \left\{ A_0^{-7/17} B_0^{-13/17} C_p^{21/17} C_0^{-14/17} D_p^{38/17} \right\} \times \\ & \left\{ \left( \frac{\beta_g^{-1} k_B}{\mu m_H} \right)^{3/17} \sigma_{\text{SB}}^{-13/17} \kappa_{\text{es}}^{-2/17} r_S^{-16/17} c^{33/17} \kappa_0^{-14/17} \right\} \\ & \left( \frac{r_p}{r_S} \right)^{-6/17} \left( 1 - \frac{r_0}{2a} \right)^{-14/17} \left( \frac{\dot{M}}{\dot{M}_{\text{Edd}}} \right)^{-12/17} \\ \simeq & 6.95 \times 10^{-10} \text{ (g cm}^{-3}\text{)} \alpha_{-1}^{25/17} f^{-12/17} \left( \frac{1+e}{2} \right)^{16/17} \times \\ & \left\{ A_0^{-7/17} B_0^{-13/17} C_0^{-14/17} C_p^{21/17} D_p^{38/17} \right\} \times \\ & \beta_g^{-3/17} \beta_*^{6/17} f_{\text{T}}^{30/17} r_*^{12/17} m_*^{-22/17} M_6^{6/17} \times \\ & \left[ \frac{3(n-1)}{2} \right]^{-12/17} \left( 1 - \frac{r_0}{2a} \right)^{-14/17} \left( \frac{r_p}{r_{p*}} \right)^{-6/17} \left( \frac{\dot{M}}{\dot{M}_p} \right)^{-12/17} \end{aligned} \quad (119)$$

Equation (119) shows that the mass density at the radiation radius  $r_0$  decreases with accretion rate  $\rho_0 \propto \dot{M}^{-12/17}$  and thus increases with time  $\rho_0 \propto t^{12n/17} \propto t^{60/51}$  for  $n = 5/3$ , mainly because of the

receding of the radiation radius  $r_0$  with the decay of accretion rate. The mass density at  $r_0$  increases with the mass of SMBHs but decreases with stellar mass,  $\rho_0 \propto r_*^{12/17} m_*^{-22/17} \propto m_*^{-(10+12\zeta)/17} \propto m_*^{-0.736}$  for  $\zeta = 0.21$ .

From equation (75), we have the mass density around the ellipse

$$\rho \simeq A_0^{1/2} C_0 \left(1 - \frac{r_S}{r}\right)^{-1} \left[1 + \left(\frac{1+e}{2}\right) \left(\frac{r_S}{r}\right) C_p^{-1} \left(1 - \frac{r}{2a}\right)^{-1}\right]^{-1/2} \left(\frac{r_0}{r}\right) \rho_0. \quad (120)$$

Equation (120), together with equations (111) and (118), gives

$$\begin{aligned} \rho \simeq & \left(1 - \frac{r_S}{r}\right)^{-1} \left[1 + \left(\frac{1+e}{2}\right) \left(\frac{r_S}{r}\right) C_p^{-1} \left(1 - \frac{r}{2a}\right)^{-1}\right]^{-1/2} \left(\frac{r_p}{r}\right) \times \\ & \left(\frac{45\pi}{8} f\right)^{(7\gamma-11)/(11\gamma-7)} \left(\frac{20}{3\alpha_p} f\right)^{-(13\gamma-23)/(11\gamma-7)} \left(\frac{1+e}{2}\right)^{2(5\gamma-4)/(11\gamma-7)} \times \\ & \left\{A_0^{-(4\gamma-5)/(11\gamma-7)} B_0^{-(7\gamma-11)/(11\gamma-7)} C_0^{-2(4\gamma-5)/(11\gamma-7)} C_p^{(35\gamma-37)/2(11\gamma-7)} \times \right. \\ & D_p^{(20\gamma-34)/(11\gamma-7)} \left. \right\} \left\{ \left(\frac{\beta_g^{-1} k_B}{\mu m_H}\right)^{-9/(11\gamma-7)} \sigma_{\text{SB}}^{-(7\gamma-11)/(11\gamma-7)} \kappa_{\text{es}}^{-2(\gamma+1)/(11\gamma-7)} \times \right. \\ & r_S^{-2(5\gamma-4)/(11\gamma-7)} c^{3(7\gamma-5)/(11\gamma-7)} \kappa_0^{-2(4\gamma-5)/(11\gamma-7)} \left. \right\} \left(\frac{r_p}{r_S}\right)^{-6(\gamma+1)/(11\gamma-7)} \times \\ & \left(1 - \frac{r_0}{2a}\right)^{-2(4\gamma-5)/(11\gamma-7)} \left(\frac{\dot{M}}{\dot{M}_{\text{Edd}}}\right)^{-6(\gamma-2)/(11\gamma-7)}. \end{aligned} \quad (121)$$

For  $\gamma = 5/3$ , we have

$$\begin{aligned} \rho \simeq & \left(1 - \frac{r_S}{r}\right)^{-1} \left[1 + \left(\frac{1+e}{2}\right) \left(\frac{r_S}{r}\right) C_p^{-1} \left(1 - \frac{r}{2a}\right)^{-1}\right]^{-1/2} \left(\frac{r_p}{r}\right) \times \\ & \left(\frac{45\pi}{8} f\right)^{1/17} \left(\frac{20}{3\alpha_p} f\right)^{2/17} \left(\frac{1+e}{2}\right)^{13/17} \times \\ & \left\{A_0^{-5/34} B_0^{-1/17} C_0^{-5/17} C_p^{16/17} D_p^{-1/17}\right\} \times \\ & \left\{ \left(\frac{\beta_g^{-1} k_B}{\mu m_H}\right)^{-27/34} \sigma_{\text{SB}}^{-1/17} \kappa_{\text{es}}^{-8/17} r_S^{-13/17} c^{30/17} \times \right. \\ & \left. \kappa_0^{-5/17} \right\} \left(\frac{r_p}{r_S}\right)^{-24/17} \left(1 - \frac{r_0}{2a}\right)^{-5/17} \left(\frac{\dot{M}}{\dot{M}_{\text{Edd}}}\right)^{3/17} \\ \simeq & 2.38 \times 10^{-5} (\text{g cm}^{-3}) f^{3/17} \alpha_{-1}^{-2/17} \left(\frac{1+e}{2}\right)^{13/17} \times \\ & \left(1 - \frac{r_S}{r}\right)^{-1} \left[1 + \left(\frac{1+e}{2}\right) \left(\frac{r_S}{r}\right) C_p^{-1} \left(1 - \frac{r}{2a}\right)^{-1}\right]^{-1/2} \times \\ & \left\{A_0^{-5/34} B_0^{-1/17} C_0^{-5/17} C_p^{16/17} D_p^{-1/17}\right\} \times \\ & \beta_g^{27/34} \beta_*^{24/17} f_T^{-33/17} r_*^{-57/34} m_*^{14/17} M_6^{-3/34} \times \\ & \left[\frac{3(n-1)}{2}\right]^{3/17} \left(1 - \frac{r_0}{2a}\right)^{-5/17} \left(\frac{r_p}{r_{p*}}\right)^{-24/17} \left(\frac{\dot{M}}{\dot{M}_p}\right)^{3/17} \left(\frac{r_p}{r}\right). \end{aligned} \quad (122)$$

Equation (122) shows that the mass density at a given radius depends weakly on the accretion rate and BH mass and decreases with the mass of a star,  $\rho \propto r_*^{-57/34} m_*^{14/17} \propto m_*^{-(29-57\zeta)/34} \propto m_*^{-0.501}$ .

From equations (97) and (109), we have the disk half-thickness at  $r_0$ ,

$$H_0 = \left( \frac{45\pi}{8} f \right) \left( \frac{1+e}{2} \right)^{1/2} \left\{ A_0^{-1/2} B_0^{-1} C_0^{-1} D_p \right\} \left\{ \sigma_{\text{SB}}^{-1} \kappa_{\text{es}}^{-1} c^3 \right\} \times \left( \frac{r_p}{r_S} \right)^{-3/2} \left( \frac{\dot{M}}{\dot{M}_{\text{Edd}}} \right) T_0^{-4}, \quad (123)$$

which suggests a fourth power of the temperature of the disk center. Because the temperature is nearly independent of the accretion rate, the disk half-thickness at  $r_0$  approximately linearly increases with the accretion rate. Equations (123) and (110) give

$$\begin{aligned} H_0 \simeq & \left( \frac{45\pi}{8} f \right)^{-(7\gamma+13)/(33\gamma-21)} \left( \frac{20}{3\alpha_p} f \right)^{24(\gamma+1)/(33\gamma-21)} \left( \frac{1+e}{2} \right)^{-(31\gamma-11)/2(33\gamma-21)} \times \\ & \left\{ A_0^{-(25\gamma-29)/2(33\gamma-21)} B_0^{(7\gamma+13)/(33\gamma-21)} C_0^{-(25\gamma-29)/(33\gamma-21)} C_p^{-12(\gamma+1)/(33\gamma-21)} \times \right. \\ & \left. D_p^{-(31\gamma+37)/(33\gamma-21)} \right\} \left\{ \left( \frac{\beta_g^{-1} k_B}{\mu m_H} \right)^{-24/(33\gamma-21)} \sigma_{\text{SB}}^{(7\gamma+13)/(33\gamma-21)} \kappa_{\text{es}}^{-3(3\gamma+1)/(33\gamma-21)} \times \right. \\ & \left. r_S^{16(2\gamma-1)/(33\gamma-21)} c^{-3(7\gamma-3)/(33\gamma-21)} \kappa_0^{8(\gamma+1)/(33\gamma-21)} \right\} \left( \frac{r_p}{r_S} \right)^{9(5\gamma-9)/2(33\gamma-21)} \times \\ & \left( 1 - \frac{r_0}{2a} \right)^{8(\gamma+1)/(33\gamma-21)} \left( \frac{\dot{M}}{\dot{M}_{\text{Edd}}} \right)^{(17\gamma+11)/(33\gamma-21)}. \end{aligned} \quad (124)$$

For  $\gamma = 5/3$ , the disk half-thickness at  $r_0$  becomes

$$\begin{aligned} H_0 \simeq & \left( \frac{45\pi}{8} f \right)^{-37/51} \left( \frac{20}{3\alpha_p} f \right)^{32/17} \left( \frac{1+e}{2} \right)^{-61/102} \times \\ & \left\{ A_0^{-19/102} B_0^{37/51} C_0^{-19/51} C_p^{-16/17} D_p^{-133/51} \right\} \times \\ & \left\{ \left( \frac{\beta_g^{-1} k_B}{\mu m_H} \right)^{-12/17} \sigma_{\text{SB}}^{37/51} \kappa_{\text{es}}^{-9/17} r_S^{56/51} c^{-13/17} \kappa_0^{32/51} \right\} \times \\ & \left( \frac{r_p}{r_S} \right)^{-3/34} \left( 1 - \frac{r_0}{2a} \right)^{32/51} \left( \frac{\dot{M}}{\dot{M}_{\text{Edd}}} \right)^{59/51} \\ \simeq & 7.23 \times 10^{15} \text{ (cm)} f^{59/51} \alpha_{-1}^{-32/17} \left( \frac{1+e}{2} \right)^{-61/102} \times \\ & \left\{ A_0^{-19/102} B_0^{37/51} C_0^{-19/51} C_p^{-16/17} D_p^{-133/51} \right\} \times \\ & \beta_g^{12/17} \beta_*^{3/34} f_{\text{T}}^{-121/34} r_*^{-31/17} m_*^{239/102} M_6^{-59/102} \left( \frac{r_p}{r_{p*}} \right)^{-3/34} \times \\ & \left[ \frac{3(n-1)}{2} \right]^{59/51} \left( 1 - \frac{r_0}{2a} \right)^{32/51} \left( \frac{\dot{M}}{\dot{M}_p} \right)^{59/51}. \end{aligned} \quad (125)$$

From equations (118) and (124), we obtain the surface density at the radiation radius  $r_0$ ,

$$\begin{aligned}
 \Sigma_0 &\simeq 2\rho_0 H_0 \\
 &\simeq 2 \left( \frac{45\pi}{8} f \right)^{2(7\gamma-11)/3(11\gamma-7)} \left( \frac{20}{3\alpha_p} f \right)^{-(5\gamma-13)/(11\gamma-7)} \left( \frac{1+e}{2} \right)^{(29\gamma-25)/6(11\gamma-7)} \times \\
 &\quad \left\{ A_0^{-(49\gamma-41)/6(11\gamma-7)} B_0^{-2(7\gamma-11)/3(11\gamma-7)} C_0^{-(49\gamma-41)/3(11\gamma-7)} C_p^{2(4\gamma-5)/(11\gamma-7)} \times \right. \\
 &\quad \left. D_p^{(29\gamma-61)/3(11\gamma-7)} \right\} \left\{ \left( \frac{\beta_g^{-1} k_B}{\mu m_H} \right)^{-6/(11\gamma-7)} \sigma_{\text{SB}}^{-2(7\gamma-11)/3(11\gamma-7)} \kappa_{\text{es}}^{-(5\gamma-1)/(11\gamma-7)} \times \right. \\
 &\quad \left. r_S^{2(\gamma+1)/3(11\gamma-7)} c^{2(7\gamma-5)/(11\gamma-7)} \kappa_0^{-4(4\gamma-5)/3(11\gamma-7)} \right\} \left( \frac{r_p}{r_S} \right)^{3(\gamma-5)/2(11\gamma-7)} \times \\
 &\quad \left( 1 - \frac{r_0}{2a} \right)^{-4(4\gamma-5)/3(11\gamma-7)} \left( \frac{\dot{M}}{\dot{M}_{\text{Edd}}} \right)^{-(\gamma-17)/3(11\gamma-7)}. \tag{126}
 \end{aligned}$$

For  $\gamma = 5/3$ , we have

$$\begin{aligned}
 \Sigma_0 &\simeq 2 \left( \frac{45\pi}{8} f \right)^{2/51} \left( \frac{20}{3\alpha_p} f \right)^{7/17} \left( \frac{1+e}{2} \right)^{35/102} \times \\
 &\quad \left\{ A_0^{-61/102} B_0^{-2/51} C_0^{-61/51} C_p^{5/17} D_p^{-19/51} \right\} \times \\
 &\quad \left\{ \left( \frac{\beta_g^{-1} k_B}{\mu m_H} \right)^{-9/17} \sigma_{\text{SB}}^{-2/51} \kappa_{\text{es}}^{-11/17} r_S^{8/51} c^{20/17} \times \right. \\
 &\quad \left. \kappa_0^{-10/51} \right\} \left( \frac{r_p}{r_S} \right)^{-15/34} \left( 1 - \frac{r_0}{2a} \right)^{-10/51} \left( \frac{\dot{M}}{\dot{M}_{\text{Edd}}} \right)^{23/51} \\
 &\simeq 1.00 \times 10^7 \text{ (g cm}^{-2}\text{)} f^{23/51} \alpha_{-1}^{-7/17} \left( \frac{1+e}{2} \right)^{35/102} \times \\
 &\quad \left\{ A_0^{-61/102} B_0^{-2/51} C_0^{-61/51} C_p^{5/17} D_p^{-19/51} \right\} \times \\
 &\quad \beta_g^{9/17} \beta_*^{15/34} f_{\text{T}}^{-61/34} r_*^{-19/17} m_*^{107/102} M_6^{-23/102} \left( \frac{r_p}{r_{p*}} \right)^{-15/34} \times \\
 &\quad \left[ \frac{3(n-1)}{2} \right]^{23/51} \left( 1 - \frac{r_0}{2a} \right)^{-10/51} \left( \frac{\dot{M}}{\dot{M}_p} \right)^{23/51}. \tag{127}
 \end{aligned}$$

From equation (72), we have the surface density around the ellipse

$$\frac{\Sigma}{\Sigma_0} \simeq C_0 A_0^{1/2} \left( 1 - \frac{r_S}{r} \right)^{-1} \left[ 1 + \left( \frac{1+e}{2} \right) \left( \frac{r_S}{r} \right) C_p^{-1} \left( 1 - \frac{r}{2a} \right)^{-1} \right]^{-1/2}, \tag{128}$$

which is nearly independent of radius  $r$ .

### 6.6. Geometrically thin and optically thick disk

From equation (97), we have the half-opening angle of the disk

$$\frac{H_0}{r_0} = \left( \frac{c_{s0}}{v_p} \right) A_0^{(\gamma-1)/4} C_0^{(\gamma-1)/2} C_p^{-(\gamma-1)/4} \left( \frac{r_0}{r_p} \right)^{(\gamma-1)/2}$$

$$\begin{aligned}
&= \left(\frac{1+e}{2}\right)^{-1/2} \left\{ A_0^{(\gamma-1)/4} C_0^{(\gamma-1)/2} C_p^{-(\gamma+1)/4} \right\} \left\{ \left(\frac{\beta_g^{-1} k_B}{\mu m_H}\right)^{1/2} c^{-1} \right\} \times \\
&\quad \left(\frac{r_p}{r_S}\right)^{1/2} T_0^{1/2} \left(\frac{r_0}{r_p}\right)^{(\gamma-1)/2}.
\end{aligned} \tag{129}$$

Equation (129), together with equations (100) and (111), gives

$$\begin{aligned}
\frac{H_0}{r_0} &= \left(\frac{45\pi}{8} f\right)^{-(7\gamma-11)/3(11\gamma-7)} \left(\frac{20}{3\alpha_p} f\right)^{2(4\gamma-5)/(11\gamma-7)} \left(\frac{1+e}{2}\right)^{-(31\gamma-23)/6(11\gamma-7)} \times \\
&\quad \left\{ A_0^{(4\gamma-5)/3(11\gamma-7)} B_0^{(7\gamma-11)/3(11\gamma-7)} C_0^{2(4\gamma-5)/3(11\gamma-7)} C_p^{-(19\gamma-17)/2(11\gamma-7)} \times \right. \\
&\quad \left. D_p^{-(31\gamma-41)/3(11\gamma-7)} \right\} \left\{ \left(\frac{\beta_g^{-1} k_B}{\mu m_H}\right)^{3/(11\gamma-7)} \sigma_{\text{SB}}^{(7\gamma-11)/3(11\gamma-7)} \kappa_{\text{es}}^{-3(\gamma-1)/(11\gamma-7)} \times \right. \\
&\quad \left. r_S^{-(\gamma+1)/3(11\gamma-7)} c^{-(7\gamma-5)/(11\gamma-7)} \kappa_0^{2(4\gamma-5)/3(11\gamma-7)} \right\} \left(\frac{r_p}{r_S}\right)^{-(7\gamma-11)/2(11\gamma-7)} \times \\
&\quad \left(1 - \frac{r_0}{2a}\right)^{2(4\gamma-5)/3(11\gamma-7)} \left(\frac{\dot{M}}{\dot{M}_{\text{Edd}}}\right)^{(17\gamma-19)/3(11\gamma-7)}.
\end{aligned} \tag{130}$$

For  $\gamma = 5/3$ , the disk opening angle becomes

$$\begin{aligned}
\frac{H_0}{r_0} &= \left(\frac{45\pi}{8} f\right)^{-1/51} \left(\frac{20}{3\alpha_p} f\right)^{5/17} \left(\frac{1+e}{2}\right)^{-43/102} \times \\
&\quad \left\{ A_0^{5/102} B_0^{1/51} C_0^{5/51} C_p^{-11/17} D_p^{-16/51} \right\} \times \\
&\quad \left\{ \left(\frac{\beta_g^{-1} k_B}{\mu m_H}\right)^{9/34} \sigma_{\text{SB}}^{1/51} \kappa_{\text{es}}^{-3/17} r_S^{-4/51} c^{-10/17} \kappa_0^{5/51} \right\} \times \\
&\quad \left(\frac{r_p}{r_S}\right)^{-1/34} \left(1 - \frac{r_0}{2a}\right)^{5/51} \left(\frac{\dot{M}}{\dot{M}_{\text{Edd}}}\right)^{14/51} \\
&\simeq 3.03 \times 10^{-2} f^{14/51} \alpha_{-1}^{-5/17} \left(\frac{1+e}{2}\right)^{-43/102} \times \\
&\quad \left\{ A_0^{5/102} B_0^{1/51} C_0^{5/51} C_p^{-11/17} D_p^{-16/51} \right\} \times \\
&\quad \beta_g^{-9/34} \beta_*^{1/34} f_{\text{T}}^{-29/34} M_6^{-8/17} r_*^{-15/34} m_*^{19/34} \times \\
&\quad \left[\frac{3(n-1)}{2}\right]^{14/51} \left(\frac{r_p}{r_{p*}}\right)^{-1/34} \left(1 - \frac{r_0}{2a}\right)^{5/51} \left(\frac{\dot{M}}{\dot{M}_p}\right)^{14/51}.
\end{aligned} \tag{131}$$

Because the scale height of an elliptical accretion disk at radius  $r$  around the ellipse is  $H \simeq (H_0/r_0)r$ , equation (131) shows that the elliptical accretion disk is geometrically thin.

From equations (108), (110), and (111), we have the vertical optical depth at  $r_0$ ,

$$\begin{aligned}
\tau_0 &\simeq \left(\frac{c}{v_0}\right) \left(\frac{r_0}{H_0}\right) \\
&\simeq A_0^{-(115\gamma-101)/4(33\gamma-21)} B_0^{-(7\gamma-23)/(33\gamma-21)} C_0^{-(115\gamma-101)/2(33\gamma-21)} \times
\end{aligned}$$

$$\begin{aligned}
 & C_p^{(49\gamma-59)/4(11\gamma-7)} D_p^{(31\gamma-80)/(33\gamma-21)} \left( \frac{45\pi}{8} \right)^{(7\gamma-23)/(33\gamma-21)} \times \\
 & \left( \frac{20}{3\alpha_p} \right)^{-(8\gamma-19)/(11\gamma-7)} f^{-17(\gamma-2)/(33\gamma-21)} \left( \frac{1+e}{2} \right)^{(31\gamma-29)/2(33\gamma-21)} \times \\
 & \left\{ \left( \frac{\beta_g^{-1} k_B}{\mu m_H} \right)^{-17/2(11\gamma-7)} \sigma_{\text{SB}}^{-(7\gamma-23)/(33\gamma-21)} \kappa_{\text{es}}^{3(3\gamma-5)/(33\gamma-21)} r_{\text{S}}^{(\gamma+4)/(33\gamma-21)} \right\} \times \\
 & c^{3(7\gamma-6)/(33\gamma-21)} \kappa_0^{-(8\gamma-19)/(33\gamma-21)} \left\{ \left( \frac{r_p}{r_S} \right)^{3(3\gamma-5)/(11\gamma-7)} \right\} \times \\
 & \left( 1 - \frac{r_0}{2a} \right)^{-(49\gamma-59)/2(33\gamma-21)} \left( \frac{\dot{M}}{\dot{M}_{\text{Edd}}} \right)^{-17(\gamma-2)/(33\gamma-21)}. \tag{132}
 \end{aligned}$$

For  $\gamma = 5/3$ , we have

$$\begin{aligned}
 \tau_0 & \simeq \left( \frac{45\pi}{8} \right)^{-1/3} \left( \frac{20}{3\alpha_p} \right)^{1/2} f^{1/6} \left( \frac{1+e}{2} \right)^{1/3} \times \\
 & A_0^{-2/3} B_0^{1/3} C_0^{-4/3} C_p^{1/2} D_p^{-85/102} \times \\
 & \left\{ \left( \frac{\beta_g^{-1} k_B}{\mu m_H} \right)^{-3/4} \sigma_{\text{SB}}^{1/3} r_S^{1/6} c^{1/2} \kappa_0^{1/6} \right\} \times \\
 & \left( 1 - \frac{r_0}{2a} \right)^{-1/3} \left( \frac{\dot{M}}{\dot{M}_{\text{Edd}}} \right)^{1/6} \\
 & \simeq 2.96 \times 10^4 \times \alpha_{-1}^{-1/2} f^{1/6} \left( \frac{1+e}{2} \right)^{1/3} \times \\
 & \left\{ A_0^{-2/3} B_0^{1/3} C_0^{-4/3} C_p^{1/2} D_p^{-85/102} \right\} \times \\
 & \beta_g^{3/4} f_{\text{T}}^{-1/2} r_*^{-1/4} m_*^{1/3} M_6^{-1/12} \times \\
 & \left[ \frac{3(n-1)}{2} \right]^{1/6} \left( 1 - \frac{r_0}{2a} \right)^{-1/3} \left( \frac{\dot{M}}{\dot{M}_p} \right)^{1/6}, \tag{133}
 \end{aligned}$$

which is independent of the electron scattering opacity, orbital penetration factor of a star, and disk pericenter radius  $r_p$  and depends rarely on BH mass. The optical depth  $\tau_0$  depends only weakly on the mass of a star and accretion rate with  $\tau_0 \propto m_*^{(1+3\zeta)/12} \dot{M}^{1/6} \propto m_*^{0.136} \dot{M}^{0.167}$  for  $\zeta = 0.21$ . The elliptical accretion disk at the radiation radius remains optically thick until the event essentially fades away.

The vertical optical depth at radiation radius  $r_0$  due to electron scattering is

$$\begin{aligned}
 \tau_{\text{es},0} & \simeq \kappa_{\text{es}} \Sigma_0 / 2 \\
 & \simeq 1.75 \times 10^6 f^{23/51} \alpha_{-1}^{-7/17} \left( \frac{1+e}{2} \right)^{35/102} \times \\
 & \left\{ A_0^{-61/102} B_0^{-2/51} C_0^{-61/51} C_p^{5/17} D_p^{-19/51} \right\} \times \\
 & \beta_g^{9/17} \beta_*^{15/34} f_{\text{T}}^{-61/34} r_*^{-19/17} m_*^{107/102} M_6^{-23/102} \left( \frac{r_p}{r_{p*}} \right)^{-15/34} \times
 \end{aligned}$$

$$\left[ \frac{3(n-1)}{2} \right]^{23/51} \left( 1 - \frac{r_0}{2a} \right)^{-10/51} \left( \frac{\dot{M}}{\dot{M}_p} \right)^{23/51} \quad (134)$$

and  $\tau_{\text{es}} \simeq \kappa_{\text{es}} \Sigma / 2 \simeq \tau_{\text{es},0}$  at radius  $r$ , which is independent of radius around the ellipse. The Rosseland mean opacity,  $\tau_{\text{R}} \simeq \tau_0^2 / \tau_{\text{es},0} \simeq 502$ , is about three orders of magnitude smaller than the optical depth due to the electron scattering opacity.

When the vertical diffusion timescale due to the electron scattering is longer than the radial dynamic timescale, the soft X-ray photons would be trapped in fluids and advected around the ellipse without escape. The ratio of the vertical diffusion time  $t_{\text{diff,es}}$  to the radial dynamic timescale  $t_{\text{dyn}}$  is

$$\begin{aligned} \frac{t_{\text{diff,es}}}{t_{\text{dyn}}} &\simeq \left( \frac{H}{c} \tau_{\text{es}} \right) \left( \frac{r}{v} \right)^{-1} \\ &\simeq \left( \frac{H_0}{r_0} \right) \left( \frac{\kappa_{\text{es}} \Sigma_0}{2} \right) \frac{v}{c} \\ &\simeq 1.09 \times 10^4 \alpha_{-1}^{-12/17} f^{37/51} \left( \frac{1+e}{2} \right)^{-4/51} \times \\ &\quad \beta_{\text{g}}^{9/34} \beta_*^{33/34} f_{\text{T}}^{-107/34} M_6^{-37/102} r_*^{-35/17} m_*^{181/102} \left( \frac{r_{\text{p}}}{r_{\text{p}*}} \right)^{-33/34} \times \\ &\quad \left[ \frac{3(n-1)}{2} \right]^{37/51} \left( 1 - \frac{r_0}{2a} \right)^{-5/51} \left( \frac{\dot{M}}{\dot{M}_p} \right)^{37/51} \left( 1 - \frac{r}{2a} \right)^{1/2} \left( \frac{r_{\text{p}}}{r} \right)^{1/2} \end{aligned} \quad (135)$$

for  $\gamma = 5/3$ , where we have neglected all the quantities of order unity. At apocenter of the ellipse ( $r = (1+e)a$ ), we have

$$\begin{aligned} \frac{t_{\text{diff,es}}}{t_{\text{dyn}}} &\simeq 109 \alpha_{-1}^{-12/17} f^{37/51} f_{\text{T}}^{-141/34} \left( \frac{1+e}{2} \right)^{-161/102} \times \\ &\quad \beta_{\text{g}}^{9/34} \beta_*^{-1/34} r_*^{-35/17} m_*^{215/102} M_6^{-71/102} (1 + \Delta_*) \times \\ &\quad \left[ \frac{3(n-1)}{2} \right]^{37/51} \left( \frac{r_{\text{p}}}{r_{\text{p}*}} \right)^{-33/34} \left( 1 - \frac{r_0}{2a} \right)^{-5/51} \left( \frac{\dot{M}}{\dot{M}_p} \right)^{37/51}, \end{aligned} \quad (136)$$

where we have used  $e = [1 - 2\delta(1 + \Delta_*)]^{1/2}$  and  $\delta \simeq 0.02 f_{\text{T}}^{-1} \beta_*^{-1} m_*^{1/3} M_6^{-1/3}$ .

Equation (136) shows that the vertical diffusion timescale due to electron scattering is much longer than the radial dynamic timescale even at apocenter of the ellipse. Equation (136) shows that when the accretion rate decreases to less than the critical accretion rate

$$\begin{aligned} \left( \frac{\dot{M}_x}{\dot{M}_p} \right) &\simeq 1.97 \times 10^{-2} \alpha_{-1}^{36/37} f^{-1} \left( \frac{f_{\text{T}}}{1.56} \right)^{423/74} \left( \frac{1+e}{2} \right)^{161/74} \times \\ &\quad \beta_{\text{g}}^{-27/74} \beta_*^{3/74} r_*^{105/37} m_*^{-215/74} M_6^{71/74} \times \\ &\quad \left[ \frac{3(n-1)}{2} \right]^{-1} (1 + \Delta_*)^{-51/37} \left( \frac{r_{\text{p}}}{r_{\text{p}*}} \right)^{99/74}, \end{aligned} \quad (137)$$

the vertical diffusion timescale is smaller than the dynamic timescale. To obtain equation (137), we have assumed  $r_0 \ll 2a$  for  $\dot{M} \lesssim \dot{M}_x$ . Equation (137) suggests that the elliptical accretion disk with

large viscosity parameter  $\alpha_p$  of TDEs with large BH mass but small stellar mass may have a rapid change of radiation characteristics before the accretion mode changes from a thin disk to advection-dominated accretion flow. Because of the energy conservation and the invariance of the radiation efficiency,  $\Delta Q^+ \simeq \Delta Q^- \simeq \Delta Q_{\text{optical}}^- + \Delta Q_{\text{X-ray}}^-$ , the rapid brightening of optical/UV TDEs in X-rays would be associated with a decrease of optical/UV luminosity, but the total (bolometric) luminosity may smoothly follow the accretion rate. Although the real size of the X-ray emission region is large, the effective blackbody spherical radius of the X-ray luminosity may be small. If both the emission regions of optical/UV and X-ray luminosities are spherical, the effective spherical radius  $R_X$  of the X-ray emission region is  $R_X \simeq R_{\text{bb}}(L_X/L_{\text{opt}})^{1/2}(T_{\text{bb}}/T_X)^2 \sim 3.6 \times 10^{-3}R_{\text{bb}}$  for typical blackbody temperatures  $T_{\text{bb}} \sim 3 \times 10^4$  K for optical/UV emission and  $T_X \sim 5 \times 10^5$  K for X-ray radiation and  $L_X \sim L_{\text{opt}}$ . The effective spherical radius of the X-ray emission region would be about a few hundred times smaller than that of the optical/UV radiation region. Because the model predicts a TDE to be luminous in both optical/UV wave bands and soft X-rays at late time, it may be the interpretation of the observational distinction between UV/optical and X-ray-dominated TDE candidates. Or, it may be the explanation of the rapid late-time X-ray brightening of the TDEs ASASSN-15oi (Gezari et al. 2017b; Holoien et al. 2018), AT2019azh (Liu et al. 2019; van Velzen et al. 2021), OGLE16aaa (Kajava et al. 2020), and ASASSN-19dj (Hinkle et al. 2021). We will discuss this issue further in a future work.

### 6.7. Blackbody temperature and effective blackbody radii of TDEs

We now derive the surface temperature of the emission regions and the associated effective blackbody radius, both of which are measurable. From equations (106), (105), and (104), we have

$$T_{\text{bb}}^4 = \left(\frac{30\pi}{4}f\right) \left(\frac{1+e}{2}\right)^{1/2} B_0^{-1} D_p \left\{ \kappa_{\text{es}}^{-1} \sigma_{\text{SB}}^{-1} r_{\text{S}}^{-1} c^3 \right\} \times \left(\frac{r_p}{r_{\text{S}}}\right)^{-3} \left(\frac{r_0}{r_p}\right)^{-3/2} \left(1 - \frac{r_0}{2a}\right)^{1/2} \left(\frac{\dot{M}}{\dot{M}_{\text{Edd}}}\right). \quad (138)$$

Equations (138) and (111) give

$$T_{\text{bb}} = \left(\frac{4}{3}\right)^{1/4} \left(\frac{45\pi}{8}\right)^{(11\gamma+5)/4(11\gamma-7)} \left(\frac{20}{3\alpha_p}\right)^{-27/4(11\gamma-7)} \left(\frac{1+e}{2}\right)^{(11\gamma-1)/8(11\gamma-7)} \times f^{11(\gamma-2)/4(11\gamma-7)} A_0^{3(11\gamma-13)/16(11\gamma-7)} B_0^{-(11\gamma+5)/4(11\gamma-7)} C_0^{3(11\gamma-13)/8(11\gamma-7)} \times C_p^{-3(11\gamma-25)/16(11\gamma-7)} D_p^{(11\gamma+32)/4(11\gamma-7)} \left\{ \left(\frac{\beta_{\text{g}}^{-1} k_{\text{B}}}{\mu m_{\text{H}}}\right)^{33/8(11\gamma-7)} \sigma_{\text{SB}}^{-(11\gamma+5)/4(11\gamma-7)} \times \kappa_{\text{es}}^{-(11\gamma-13)/4(11\gamma-7)} r_{\text{S}}^{-(11\gamma-4)/4(11\gamma-7)} c^{3(11\gamma-6)/4(11\gamma-7)} \kappa_0^{-9/4(11\gamma-7)} \right\} \times \beta_*^{3(11\gamma-13)/4(11\gamma-7)} \left(\frac{r_{\text{t}}}{r_{\text{S}}}\right)^{-3(11\gamma-13)/4(11\gamma-7)} \left(\frac{r_p}{r_{\text{p}^*}}\right)^{-3(11\gamma-13)/4(11\gamma-7)} \times \left(1 - \frac{r_0}{2a}\right)^{(11\gamma-25)/8(11\gamma-7)} \left(\frac{\dot{M}_p}{\dot{M}_{\text{Edd}}}\right)^{11(\gamma-2)/4(11\gamma-7)} \left(\frac{\dot{M}}{\dot{M}_p}\right)^{11(\gamma-2)/4(11\gamma-7)}. \quad (139)$$

For  $\gamma = 5/3$ , equation (139) becomes

$$T_{\text{bb}} = \left(\frac{4}{3}\right)^{1/4} \left(\frac{45\pi}{8}\right)^{35/68} \left(\frac{20}{3\alpha_p}\right)^{-81/136} \left(\frac{1+e}{2}\right)^{13/68} f^{-11/136} \times$$

$$\begin{aligned}
& A_0^{3/34} B_0^{-35/68} C_0^{3/17} C_p^{15/136} D_p^{151/136} \left\{ \left( \frac{\beta_g^{-1} k_B}{\mu m_H} \right)^{99/272} \sigma_{\text{SB}}^{-35/68} \times \right. \\
& \left. \kappa_{\text{es}}^{-2/17} r_S^{-43/136} c^{111/136} \kappa_0^{-27/136} \right\} \beta_*^{6/17} \left( \frac{r_t}{r_S} \right)^{-6/17} \left( \frac{r_p}{r_{p*}} \right)^{-6/17} \times \\
& \left( 1 - \frac{r_0}{2a} \right)^{-5/68} \left( \frac{\dot{M}_p}{\dot{M}_{\text{Edd}}} \right)^{-11/136} \left( \frac{\dot{M}}{\dot{M}_p} \right)^{-11/136} \\
& \simeq 1.98 \times 10^4 \text{ K } \alpha_{-1}^{81/136} \left( \frac{1+e}{2} \right)^{13/68} \times \\
& f^{-11/136} A_0^{3/34} B_0^{-35/68} C_0^{3/17} C_p^{15/136} D_p^{151/136} \times \\
& \beta_g^{-99/272} \beta_*^{6/17} f_T^{-15/136} M_6^{11/272} r_*^{-63/272} m_*^{-3/68} \times \\
& \left[ \frac{3(n-1)}{2} \right]^{-11/136} \left( \frac{r_p}{r_{p*}} \right)^{-6/17} \left( 1 - \frac{r_0}{2a} \right)^{-5/68} \left( \frac{\dot{M}}{\dot{M}_p} \right)^{-11/136}, \tag{140}
\end{aligned}$$

where the radiation radius  $r_0$  is given with equation (117).

Equation (140) shows that the elliptical accretion disk radiates with a typical effective blackbody temperature  $T_{\text{bb}} \simeq 3 \times 10^4 \text{ K } (\alpha_p/0.2)^{81/136}$ . Figure 2 gives the blackbody temperature as a function of accretion rate (top panel) and time (bottom panel) for  $n = 5/3$  and different viscosity parameter  $\alpha_p = 0.05, 0.1, 0.2, 0.3, \text{ and } 0.5$ . Equation (140) and Figure 2 show that the blackbody temperature depends on the viscosity parameter  $\alpha_p$  and is nearly independent of the accretion rate,  $T_{\text{bb}} \propto \alpha_{-1}^{81/136} \dot{M}^{-0.081}$  except at about the time of the peak accretion rate, when the blackbody temperature evolves rapidly (see discussion in Sec. 6.8). For the reasonable range of the viscosity parameter (van Velzen et al. 2019), the blackbody temperature of optical/UV TDEs is typically  $T_{\text{bb}} \simeq 3 \times 10^4 \text{ K}$  for  $\alpha_p \simeq 0.2$  and would be in the range of  $T_{\text{bb}} \simeq 1 \times 10^4 \text{ K}$  for  $\alpha_p = 0.05$  and  $8 \times 10^4 \text{ K}$  for  $\alpha_p = 0.5$  and  $m_* \simeq 0.3$ . For the typical fallback rate  $\dot{M} \propto t^{-5/3}$ , we have  $T_{\text{bb}} \propto t^{0.135}$ . If the radiation cooling in soft X-ray and EUV in the region of the  $r_p \lesssim r \ll r_0$  is significant, the polytropic index is larger than the adiabatic index  $\gamma_{\text{ad}} = 5/3$ . For example, if the polytropic index is  $\gamma = 2$ , typical for the gas giant planets, equation (139) shows that the radiation temperature would be completely independent of the accretion rate,  $T_{\text{bb}} \propto \dot{M}^0$ . Therefore, a prediction of the elliptical accretion disk model is that optical/UV TDEs with comparable X-ray radiation should have rather steady or even decreasing blackbody temperature with decay of the accretion rate. However, when the radiation cooling in soft X-rays at  $r \ll r_0$  is significant, we cannot simply use equation (105) to estimate the cooling rate  $\Delta Q^-$  and instead have to integrate the emission of the disk surface from  $r_p \lesssim r \lesssim r_0$ .

Figure 3 gives the blackbody temperature for the typical viscosity parameter  $\alpha_p = 0.2$  as a function of time for BH mass  $M_{\text{BH}} = 10^{5.5} M_\odot, 10^6 M_\odot, \text{ and } 10^{6.5} M_\odot$  and mass of the star  $m_* = 0.1, 0.3, \text{ and } 0.4$ . Figure 3 and equation (140) show that the typical effective blackbody temperature decreases weakly with the mass of the star,  $T_{\text{bb}} \propto r_*^{-63/272} m_*^{-3/68} \propto m_*^{-(75-63\zeta)/272} \propto m_*^{-0.23}$  for  $\zeta = 0.21$ , and is practically independent of the BH mass  $T_{\text{bb}} \propto M_6^{0.04}$  except around the time of the peak. At about the time of the peak, the blackbody temperature for low BH mass with  $M_{\text{BH}} \simeq 10^{5.5} M_\odot$  decreases rapidly first to a minimum and is followed by the swift increase to a constant value. Our results suggest that the variations of observed blackbody temperature of optical/UV TDEs are mainly due to the differences of the viscosity parameters and partly to the variations of the orbital penetration factor among TDEs.

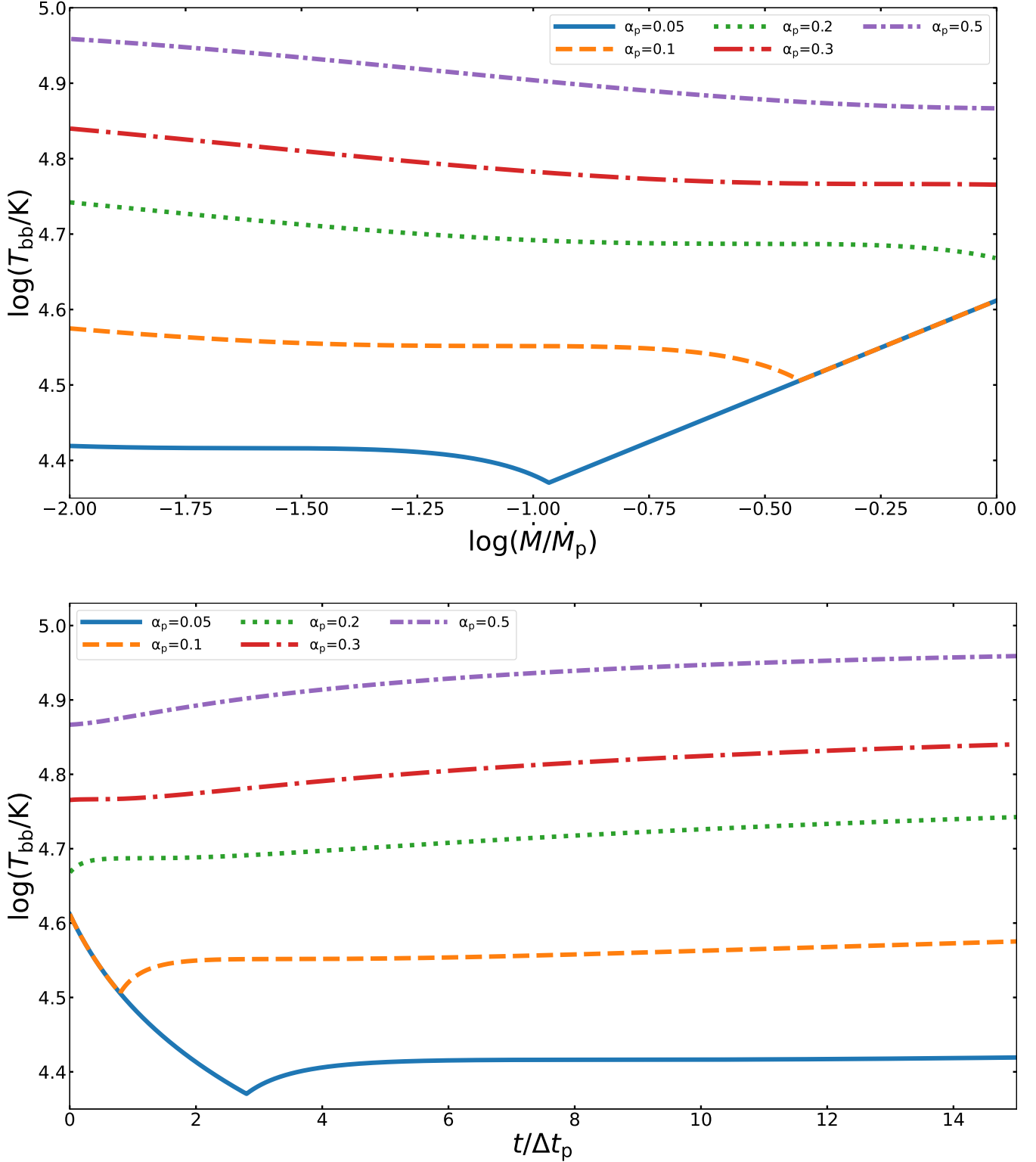


**Figure 2.** Radiation blackbody temperature as a function of accretion rate (top panel) and time (bottom panel) for different viscosity parameters  $\alpha_p$ . The blackbody temperature is calculated for full disruption with  $\beta_* = 1.0$ ,  $M_{\text{BH}} = 10^6 M_\odot$ , and  $m_* = 0.3$ . The other parameters are  $r_{\text{ms}} = 2r_{\text{S}}$ ,  $\beta_{\text{g}} = 1$ ,  $r_{\text{p}} = r_{\text{p}*}$ ,  $r_* = m_*^{1-\zeta}$  with  $\zeta = 0.21$ ,  $f_{\text{T}} = 1.56$ , and  $n = 5/3$ . The time starts at the peak of the accretion rate. The radiation blackbody temperature is nearly constant except for the low viscosity parameter at time of about the peak.

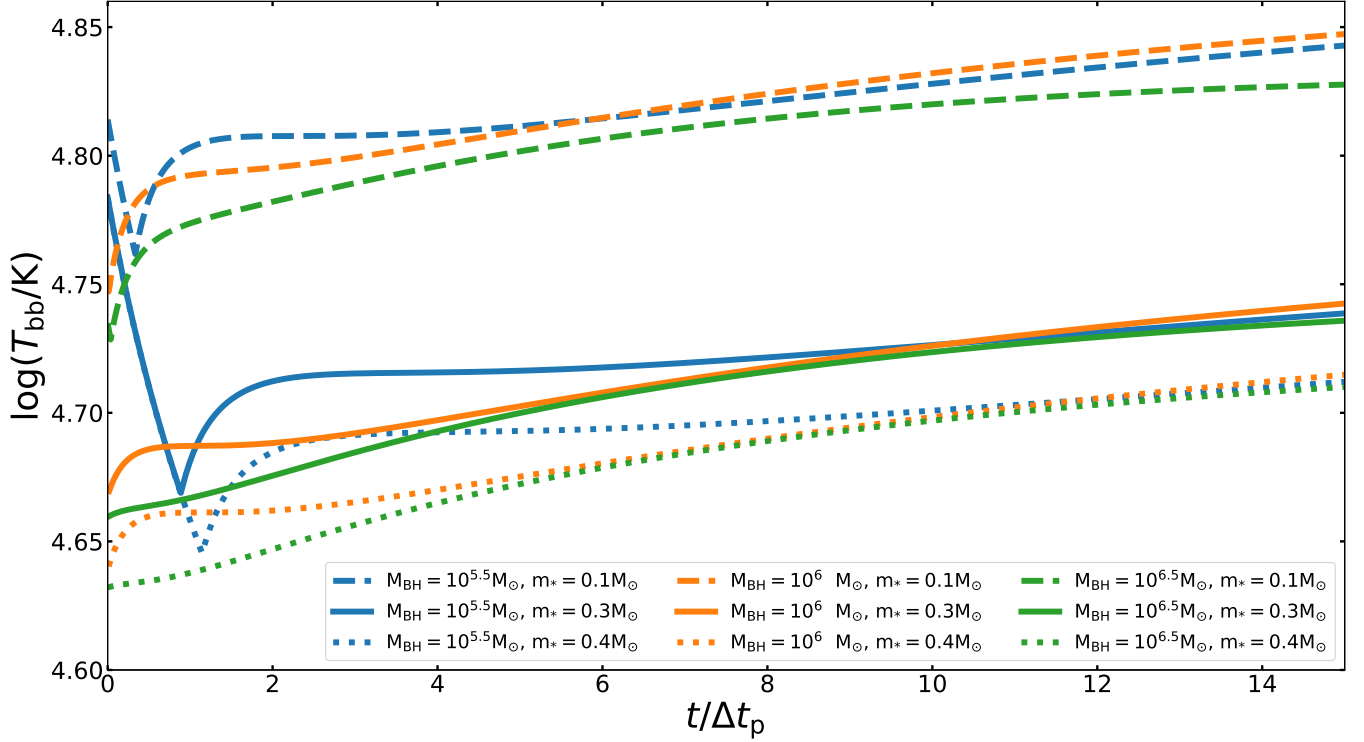


**Figure 3.** Radiation blackbody temperature as a function of time for BH mass  $M_{\text{BH}} = 10^{5.5}M_{\odot}$ ,  $10^6M_{\odot}$ , and  $10^{6.5}M_{\odot}$ , and mass of the star  $m_* = 0.1, 0.3$ , and  $0.4$ . The blackbody temperature for the viscosity parameter  $\alpha_p = 0.2$  is calculated with  $\beta_* = 1.0$ ,  $\beta_g = 1$ ,  $r_{\text{ms}} = 2r_{\text{S}}$ ,  $r_p = r_{p*}$ ,  $r_* = m_*^{1-\zeta}$  with  $\zeta = 0.21$ ,  $f_{\text{T}} = 1.47(0.80 + 0.26M_6^{0.5})$ , and  $n = 5/3$ . Time starts from the peak of the accretion rate. The radiation blackbody temperature is nearly constant with time except at about the time of the peak. For low BH mass  $M_{\text{BH}} = 10^{5.5}M_{\odot}$ , the radiation blackbody temperature decreases at about the time of the peak to the minimum, followed by rapid increase to a nearly constant value. The radiation blackbody temperature decreases with the mass of the star.

Equation (140) shows that the radiation temperature  $T_{\text{bb}}$  is a weak function of pericenter radius  $r_p$  and has a much smaller dependence of radius than the typical power law  $r^{-3/4}$  ( $r_p = r$  in the circular disk) either in the standard thin disk (Shakura & Sunyaev 1973) or  $r^{-1/2}$  in the slim accretion disk (Abramowicz et al. 1988; Strubbe & Quataert 2009). It changes by up to 70% from  $r_{p*} = 23.545r_{\text{S}}$  to  $3r_{\text{S}}$  and gives an SED of emission very close to a single-temperature blackbody, significantly different from the SEDs of either the standard thin or slim accretion disk.

The typical radiation radius  $r_0$  given with equation (117) is not directly measured in the literature. Model-independent effective blackbody radius is observationally obtained by assuming that the observed bolometric luminosity  $L_{\text{bol}}$  is emitted by a spherical envelope with blackbody of single temperature  $T_{\text{bb}}$ ,

$$4\pi R_{\text{bb}}^2 \sigma_{\text{SB}} T_{\text{bb}}^4 = L_{\text{bol}}. \quad (141)$$

In the elliptical accretion disk, the total radiation energy can be calculated with  $L_{\text{bol}} = \eta \dot{M} c^2$ , where  $\eta$  is the radiation efficiency. Letting  $r_p = r_{\text{ms}}$ , we can calculate the radiation efficiency with equation (13) (see also Liu et al. 2017; Cao et al. 2018; Zhou et al. 2021),

$$\eta = \frac{e_{\text{G}}}{c^2}$$

$$\simeq \delta \frac{(1 + \Delta_*)}{8} \left( \frac{1 + e}{2} \right)^{-1} \left( \frac{2r_S}{r_{\text{ms}}} \right) \left[ 1 - \frac{\delta(1 + \Delta_*)}{(1 + e)} \left( \frac{r_S}{r_{\text{ms}} - r_S} \right) \right]. \quad (142)$$

Here we have neglected the  $[(1 - e)/2]^2$  terms and higher. Provided the radiation efficiency, we have the total luminosity

$$\begin{aligned} L_{\text{bol}} &= \eta \dot{M} c^2 \\ &\simeq \delta \frac{(1 + \Delta_*)}{8} \left( \frac{1 + e}{2} \right)^{-1} \left( \frac{2r_S}{r_{\text{ms}}} \right) \left[ 1 - \frac{\delta(1 + \Delta_*)}{(1 + e)} \left( \frac{r_S}{r_{\text{ms}} - r_S} \right) \right] \left( \frac{\dot{M}}{\dot{M}_p} \right) \dot{M}_p c^2 \\ &\simeq 7.11 \times 10^{43} \text{ (erg s}^{-1}\text{)} \beta_*^{-1} \left( \frac{f_{\text{T}}}{1.56} \right)^{-4} r_*^{-3/2} m_*^{7/3} M_6^{-5/6} (1 + \Delta_*) \times \\ &\quad \left[ \frac{3(n - 1)}{2} \right] \left( \frac{1 + e}{2} \right)^{-1} \left( \frac{2r_S}{r_{\text{ms}}} \right) \left[ 1 - \frac{\delta(1 + \Delta_*)}{(1 + e)} \left( \frac{r_S}{r_{\text{ms}} - r_S} \right) \right] \left( \frac{\dot{M}}{\dot{M}_p} \right) \\ &\simeq 0.494 \beta_*^{-1} \left( \frac{f_{\text{T}}}{1.56} \right)^{-4} r_*^{-3/2} m_*^{7/3} M_6^{-11/6} (1 + \Delta_*) \left( \frac{1 + e}{2} \right)^{-1} \times \\ &\quad \left[ \frac{3(n - 1)}{2} \right] \left( \frac{2r_S}{r_{\text{ms}}} \right) \left[ 1 - \frac{\delta(1 + \Delta_*)}{(1 + e)} \left( \frac{r_S}{r_{\text{ms}} - r_S} \right) \right] \left( \frac{\dot{M}}{\dot{M}_p} \right) L_{\text{Edd}}. \end{aligned} \quad (143)$$

TDEs with stellar mass  $m_* \lesssim 0.5$  or BH mass  $M_{\text{BH}} \gtrsim 10^6 M_\odot$  have sub-Eddington luminosities even at peak luminosity, whereas for TDEs with BHs of mass  $M_{\text{BH}} \lesssim 10^5 M_\odot$ , the expected peak luminosity is highly super-Eddington, and the light curve would have an extended plateau top-capped by the Eddington luminosity.

From equations (141) and (143), we have the effective blackbody radius

$$\begin{aligned} R_{\text{bb}} &= \left( \frac{5}{4} \right)^{1/2} \left( \frac{1 + e}{2} \right)^{-1/2} \left( \frac{\delta}{2} \right)^{1/2} \left( \frac{2r_S}{r_{\text{ms}}} \right)^{1/2} \left[ 1 - \delta \frac{(1 + \Delta_*)}{(1 + e)} \left( \frac{r_S}{r_{\text{ms}} - r_S} \right) \right]^{1/2} \times \\ &\quad (1 + \Delta_*)^{1/2} \left\{ \sigma_{\text{SB}}^{-1/2} \kappa_{\text{es}}^{-1/2} r_S^{1/2} c^{3/2} \right\} \left( \frac{\dot{M}}{\dot{M}_{\text{Edd}}} \right)^{1/2} T_{\text{bb}}^{-2}, \end{aligned} \quad (144)$$

which, together with equation (139), gives

$$\begin{aligned} R_{\text{bb}} &= \left( \frac{320}{3} \right)^{-1/2} \left( \frac{45\pi}{8} \right)^{-(11\gamma+5)/2(11\gamma-7)} \left( \frac{20}{3\alpha_p} \right)^{27/2(11\gamma-7)} f^{-11(\gamma-2)/2(11\gamma-7)} \times \\ &\quad A_0^{-3(11\gamma-13)/8(11\gamma-7)} B_0^{(11\gamma+5)/2(11\gamma-7)} C_0^{-3(11\gamma-13)/4(11\gamma-7)} C_p^{3(11\gamma-25)/8(11\gamma-7)} \times \\ &\quad D_p^{-(11\gamma+32)/2(11\gamma-7)} \left( \frac{2r_S}{r_{\text{ms}}} \right)^{1/2} \left( \frac{1 + e}{2} \right)^{-3(11\gamma-5)/4(11\gamma-7)} \left[ 1 - \delta \frac{(1 + \Delta_*)}{(1 + e)} \left( \frac{r_S}{r_{\text{ms}} - r_S} \right) \right]^{1/2} \times \\ &\quad (1 + \Delta_*)^{1/2} \left\{ \left( \frac{\beta_g^{-1} k_{\text{B}}}{\mu m_{\text{H}}} \right)^{-33/4(11\gamma-7)} \sigma_{\text{SB}}^{6/(11\gamma-7)} \kappa_{\text{es}}^{-3/(11\gamma-7)} r_S^{11(2\gamma-1)/2(11\gamma-7)} c^{-3/2(11\gamma-7)} \times \right. \\ &\quad \left. \kappa_0^{9/2(11\gamma-7)} \right\} \left( \frac{r_p}{r_{p*}} \right)^{3(11\gamma-13)/2(11\gamma-7)} \left( \frac{r_t}{r_S} \right)^{3(11\gamma-13)/2(11\gamma-7)} \beta_*^{-(22\gamma-23)/(11\gamma-7)} f_{\text{T}}^{-1/2} \times \\ &\quad m_*^{1/6} M_6^{-1/6} \left( 1 - \frac{r_0}{2a} \right)^{-(11\gamma-25)/4(11\gamma-7)} \left( \frac{\dot{M}_p}{\dot{M}_{\text{Edd}}} \right)^{15/2(11\gamma-7)} \left( \frac{\dot{M}}{\dot{M}_p} \right)^{15/2(11\gamma-7)}. \end{aligned} \quad (145)$$

For the polytropic index  $\gamma = 5/3$ , the effective blackbody radius is

$$\begin{aligned}
R_{\text{bb}} = & \left(\frac{320}{3}\right)^{-1/2} \left(\frac{45\pi}{8}\right)^{-35/34} \left(\frac{20}{3\alpha_{\text{p}}}\right)^{81/68} f^{11/68} \times \\
& A_0^{-3/17} B_0^{35/34} C_0^{-6/17} C_{\text{p}}^{-15/68} D_{\text{p}}^{-151/68} \times \\
& \left(\frac{2r_{\text{S}}}{r_{\text{ms}}}\right)^{1/2} \left(\frac{1+e}{2}\right)^{-15/17} \left[1 - \delta \frac{(1+\Delta_*)}{(1+e)} \left(\frac{r_{\text{S}}}{r_{\text{ms}} - r_{\text{S}}}\right)\right]^{1/2} \times \\
& (1+\Delta_*)^{1/2} \left\{ \left(\frac{\beta_{\text{g}}^{-1} k_{\text{B}}}{\mu m_{\text{H}}}\right)^{-99/136} \sigma_{\text{SB}}^{9/17} \kappa_{\text{es}}^{-9/34} r_{\text{S}}^{77/68} c^{-9/68} \kappa_0^{27/68} \right\} \left(\frac{r_{\text{p}}}{r_{\text{p}^*}}\right)^{12/17} \times \\
& \left(\frac{r_{\text{t}}}{r_{\text{S}}}\right)^{12/17} \beta_*^{-41/34} f_{\text{T}}^{-1/2} m_*^{1/6} M_6^{-1/6} \left(1 - \frac{r_0}{2a}\right)^{5/34} \left(\frac{\dot{M}_{\text{p}}}{\dot{M}_{\text{Edd}}}\right)^{45/68} \left(\frac{\dot{M}}{\dot{M}_{\text{p}}}\right)^{45/68} \\
\approx & 1.87 \times 10^{15} \text{ (cm)} \alpha_{-1}^{-81/68} f^{11/68} A_0^{-3/17} B_0^{35/34} C_0^{-6/17} C_{\text{p}}^{-15/68} D_{\text{p}}^{-151/68} \times \\
& \left(\frac{2r_{\text{S}}}{r_{\text{ms}}}\right)^{1/2} \left(\frac{1+e}{2}\right)^{-15/17} \left[1 - \delta \frac{(1+\Delta_*)}{(1+e)} \left(\frac{r_{\text{S}}}{r_{\text{ms}} - r_{\text{S}}}\right)\right]^{1/2} (1+\Delta_*)^{1/2} \times \\
& \beta_{\text{g}}^{99/136} \beta_*^{-41/34} f_{\text{T}}^{-121/68} r_*^{-39/136} m_*^{64/51} M_6^{-203/408} \times \\
& \left[\frac{3(n-1)}{2}\right]^{45/68} \left(1 - \frac{r_0}{2a}\right)^{5/34} \left(\frac{r_{\text{p}}}{r_{\text{p}^*}}\right)^{12/17} \left(\frac{\dot{M}}{\dot{M}_{\text{p}}}\right)^{45/68}, \tag{146}
\end{aligned}$$

where the radiation radius  $r_0$  is given with equation (117). Equation (146) suggests that the effective blackbody radius of optical/UV TDEs increases with accretion rate and decreases with time.

Equation (146) shows that the effective blackbody radius significantly depends on the accretion rate, the BH mass, the mass and orbital penetration factor of the star, and the viscosity parameter. The effective blackbody radius of TDEs depends nearly linearly on the mass of the star,  $R_{\text{bb}} \propto r_*^{-39/136} m_*^{64/51} \propto m_*^{(395+117\zeta)/408} \propto m_*^{1.03}$  for  $\zeta = 0.21$ .

Figure 4 gives the effective blackbody radius as a function of time for different viscosity parameter  $\alpha_{\text{p}}$ , and Figure 5 shows the variations of the effective blackbody radius with time for different BH masses  $M_{\text{BH}} = 10^{5.5} M_{\odot}$ ,  $10^6 M_{\odot}$ , and  $10^{6.5} M_{\odot}$  and the mass of the star  $m_* = 0.1, 0.3, \text{ and } 0.4$ . The effective blackbody radius significantly depends on the accretion rate  $R_{\text{bb}} \propto (\dot{M}/\dot{M}_{\text{p}})^{0.662}$  and decreases with time  $R_{\text{bb}} \propto t^{-75/68} \propto t^{-1.10}$  for  $n = 5/3$ , which is very different from the expectation of constant radius of the circular accretion disk or shock model for TDEs. The power law of index 0.662, because of the slight dependence of temperature on accretion rate, is higher than the index 0.5, which is expected with constant blackbody temperature  $T_{\text{bb}}$ . Because accretion rate given in equation (2) depends on the power-law index  $n$  and the structure and age of the star, we would suggest to observe the effective blackbody radius  $R_{\text{bb}}$  as a function of both accretion rate  $\dot{M}$  (or luminosity) and time to measure the power-law index of  $n$ , which depends on the age and structure of a star.

### 6.8. Bright TDEs with constant radiation radius of apocenter

Equation (117) shows that the radiation radius  $r_0$  varies with accretion rate  $\dot{M}$  and should increase with time before peak brightness. Because the radiation radius cannot be larger than the apocenter radius  $(1+e)a_{\text{d}}$ , we have a critical accretion rate  $\dot{M}_{\text{cr}}$ . For  $\dot{M} < \dot{M}_{\text{cr}}$  the radiation radius  $r_0$  varies with accretion rate and is given by equation (117), while for  $\dot{M} \geq \dot{M}_{\text{cr}}$  the radiation radius  $r_0$  does

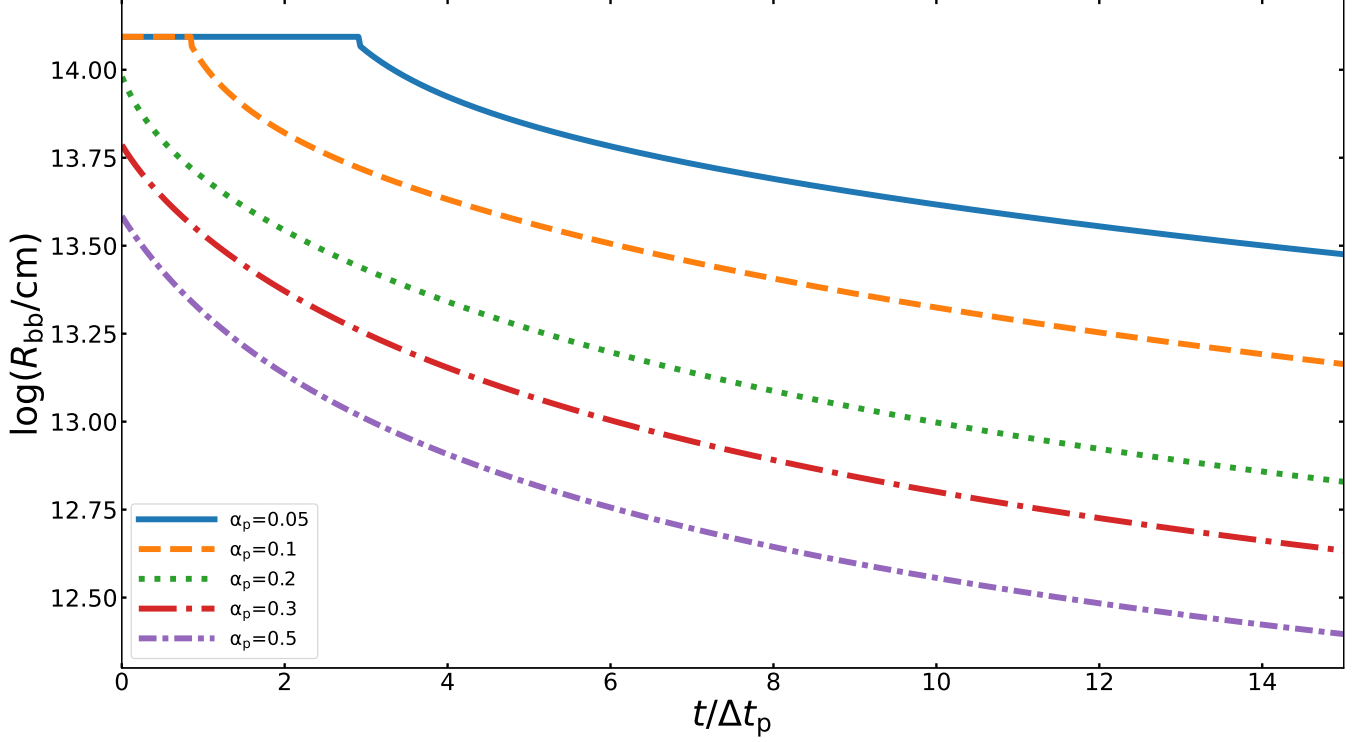


**Figure 4.** Effective blackbody radius as a function of time for different viscosity parameter  $\alpha_p$ . The effective blackbody radius is calculated with  $M_{\text{BH}} = 10^6 M_{\odot}$ ,  $\beta_* = 1$ ,  $r_{\text{ms}} = 2r_{\text{S}}$ ,  $\beta_{\text{g}} = 1$ ,  $r_{\text{p}} = r_{\text{p}*}$ ,  $m_* = 0.3$ ,  $r_* = m_*^{1-\zeta}$  with  $\zeta = 0.21$ ,  $f_{\text{T}} = 1.56$ , and  $n = 5/3$ . The time starts at the peak accretion rate.

not change with accretion rate and remains constant with  $r_0 = (1 + e)a_{\text{d}}$ . Letting  $r_0 = (1 + e)a_{\text{d}}$ ,  $a = a_{\text{d}}$ , and  $r_{\text{p}} = r_{\text{p}*}$  and from equation (111), we obtain

$$\begin{aligned}
 \frac{1+e}{1-e} \simeq & A_0^{-(11\gamma-13)/2(11\gamma-7)} B_0^{8/(11\gamma-7)} C_0^{-(11\gamma-13)/(11\gamma-7)} C_{\text{p}}^{(11\gamma-25)/2(11\gamma-7)} D_{\text{p}}^{-26/(11\gamma-7)} \times \\
 & \left( \frac{45\pi}{8} f \right)^{-8/(11\gamma-7)} \left( \frac{20}{3\alpha_{\text{p}}} f \right)^{18/(11\gamma-7)} \left( \frac{1+e}{2} \right)^{-2/(11\gamma-7)} \times \\
 & \left\{ \left( \frac{\beta_{\text{g}}^{-1} k_{\text{B}}}{\mu m_{\text{H}}} \right)^{-11/(11\gamma-7)} \sigma_{\text{SB}}^{8/(11\gamma-7)} \kappa_{\text{es}}^{-4/(11\gamma-7)} r_{\text{S}}^{2/(11\gamma-7)} c^{-2/(11\gamma-7)} \kappa_0^{6/(11\gamma-7)} \right\} \\
 & \beta_*^{12/(11\gamma-7)} \left( \frac{r_{\text{t}}}{r_{\text{S}}} \right)^{-12/(11\gamma-7)} \left( \frac{1-e}{2} \right)^{6/(11\gamma-7)} \times \\
 & \left( \frac{\dot{M}_{\text{p}}}{\dot{M}_{\text{Edd}}} \right)^{10/(11\gamma-7)} \left( \frac{\dot{M}_{\text{cr}}}{\dot{M}_{\text{p}}} \right)^{10/(11\gamma-7)}, \tag{147}
 \end{aligned}$$

where we have used  $1 - (r_0/2a) = (1 - e)/2$ . From equation (147), we have

$$\begin{aligned}
 \frac{\dot{M}_{\text{cr}}}{\dot{M}_{\text{p}}} \simeq & \left( \frac{\dot{M}_{\text{p}}}{\dot{M}_{\text{Edd}}} \right)^{-1} \left( \frac{1+e}{2} \right)^{(11\gamma-3)/5} \left[ \frac{2\delta(1+\Delta_*)}{4} \right]^{-(11\gamma-1)/10} \times \\
 & A_0^{(11\gamma-13)/20} B_0^{-4/5} C_0^{(11\gamma-13)/10} C_{\text{p}}^{-(11\gamma-25)/20} D_{\text{p}}^{13/5} \times
 \end{aligned}$$

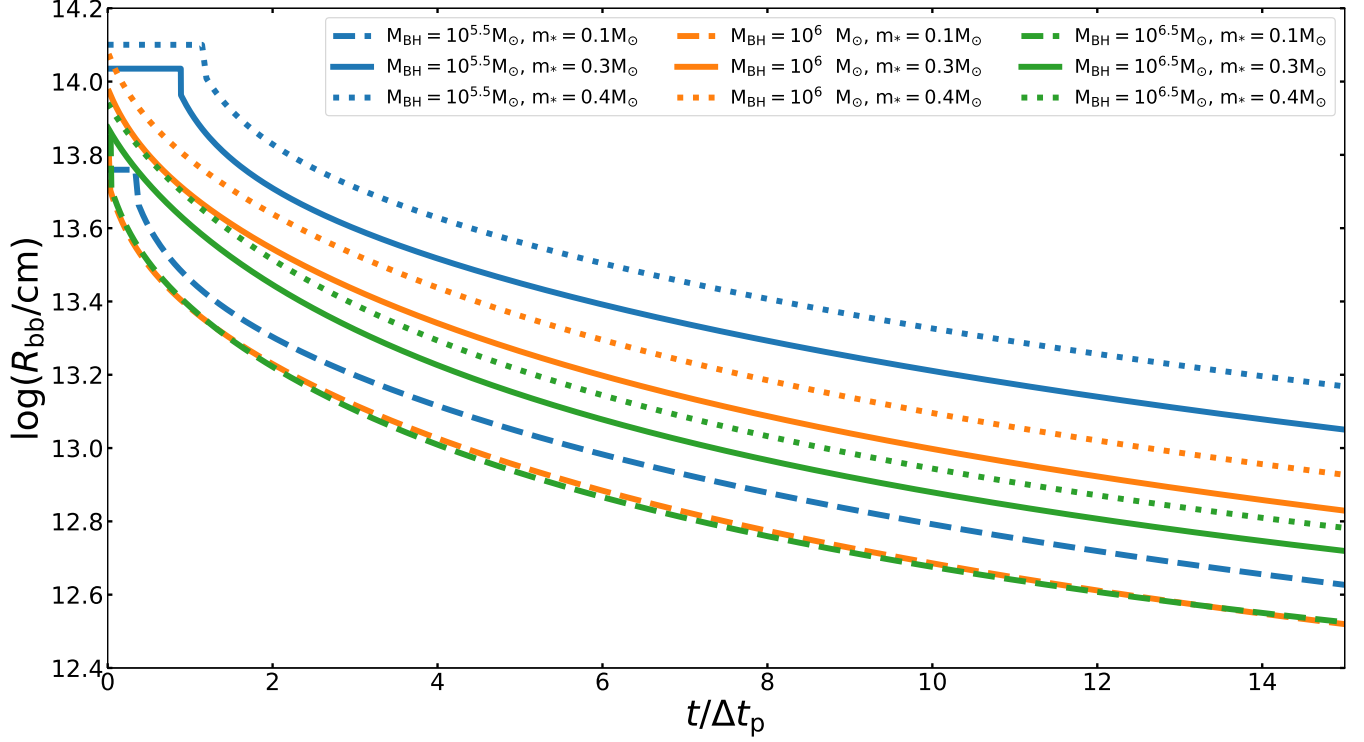


**Figure 5.** Effective blackbody radius as a function of time for different BH and stellar masses. The effective blackbody radius is calculated with  $\alpha_p = 0.2$ ,  $\beta_* = 1$ ,  $r_{ms} = 2r_S$ ,  $\beta_g = 1$ ,  $r_p = r_{p*}$ ,  $r_* = m_*^{1-\zeta}$  with  $\zeta = 0.21$ ,  $f_T = 1.47(0.80 + 0.26M_6^{0.5})$ , and  $n = 5/3$ . The time starts at the peak accretion rate.

$$\left(\frac{45\pi}{8}f\right)^{4/5} \left(\frac{20}{3\alpha_p}f\right)^{-9/5} \left\{ \left(\frac{\beta_g^{-1}k_B}{\mu m_H}\right)^{11/10} \sigma_{SB}^{-4/5} \kappa_{es}^{2/5} r_S^{-1/5} c^{1/5} \kappa_0^{-3/5} \right\} \times \beta_*^{-6/5} \left(\frac{r_t}{r_S}\right)^{6/5}, \quad (148)$$

where we have used  $1 - e^2 = 2\delta(1 + \Delta_*)$ . For  $\gamma = 5/3$ , equation (148) gives

$$\begin{aligned} \frac{\dot{M}_{cr}}{\dot{M}_p} &\simeq \left(\frac{\dot{M}_p}{\dot{M}_{Edd}}\right)^{-1} \left(\frac{1+e}{2}\right)^{46/15} \left[\frac{2\delta(1+\Delta_*)}{4}\right]^{-26/15} \times \\ &A_0^{4/15} B_0^{-4/5} C_0^{8/15} C_p^{1/3} D_p^{13/5} \left(\frac{45\pi}{8}f\right)^{4/5} \left(\frac{20}{3\alpha_p}f\right)^{-9/5} \times \\ &\left\{ \left(\frac{\beta_g^{-1}k_B}{\mu m_H}\right)^{11/10} \sigma_{SB}^{-4/5} \kappa_{es}^{2/5} r_S^{-1/5} c^{1/5} \kappa_0^{-3/5} \right\} \beta_*^{-6/5} \left(\frac{r_t}{r_S}\right)^{6/5} \\ &\simeq 0.822 A_0^{4/15} B_0^{-4/5} C_0^{8/15} C_p^{1/3} D_p^{13/5} f^{-1} \alpha_{-1}^{9/5} \times \\ &\beta_g^{-11/10} \beta_*^{8/15} \left(\frac{f_T}{1.56}\right)^{89/15} (1+\Delta_*)^{-26/15} \left(\frac{1+e}{2}\right)^{46/15} \times \\ &\left[\frac{3(n-1)}{2}\right]^{-1} \left(\frac{m_*}{0.3}\right)^{-(25+243\zeta)/90} M_6^{97/90} \end{aligned} \quad (149)$$

with  $\zeta = 0.21$ .

Equation (149) shows that the peak accretion rate of optical/UV TDEs with typical stellar mass  $M_{\text{BH}} \gtrsim 10^6 M_{\odot}$  and viscosity parameter  $\alpha_{\text{p}} \gtrsim 0.2$  is less than the critical accretion rate. For TDEs with  $\dot{M}_{\text{cr}} > \dot{M}_{\text{p}}$ , the radiation radius  $r_0$  is given with equation (117) and the effective blackbody radius  $R_{\text{bb}}$  is calculated with equation (146). Our elliptical accretion disk model suggests that both the radiation radius  $r_0$  and effective blackbody radius  $R_{\text{bb}}$  should closely follow the change of accretion rate or the luminosity with some possible delay of peak radius relative to the peak accretion rate because of the term  $[1 - (r_0/2a)]$ . The blackbody temperature is given with equation (140) and would change with accretion rate near the peak of the accretion rate or at the peak time  $t \sim 0$ , if the peak accretion rate is about the critical accretion rate  $\dot{M}_{\text{p}} \sim \dot{M}_{\text{cr}}$ , as shown in Figures 3 and 2.

Equation (149) suggests that for TDEs with BH mass  $M_{\text{BH}} \lesssim 10^6 M_{\odot}$  or viscosity parameter  $\alpha_{\text{p}} \lesssim 0.2$  the peak accretion rate may be larger than the critical accretion rate. For  $\dot{M} \geq \dot{M}_{\text{cr}}$ , the total luminosity of TDEs decreases with accretion rate and the radiation radius remains constant with  $r_0 = (1 + e)a_{\text{d}}$ . From Equation (138), we have

$$\begin{aligned}
 T_{\text{bb}} &\simeq (5\pi f)^{1/4} \left(\frac{1 - e^2}{4}\right)^{1/2} \left(\frac{1 + e}{2}\right)^{-3/4} D_{\text{p}}^{1/4} \left\{ \kappa_{\text{es}}^{-1/4} \sigma_{\text{SB}}^{-1/4} r_{\text{S}}^{-1/4} c^{3/4} \right\} \times \\
 &\quad \beta_*^{3/4} \left(\frac{r_{\text{t}}}{r_{\text{S}}}\right)^{-3/4} \left(\frac{\dot{M}_{\text{p}}}{\dot{M}_{\text{Edd}}}\right)^{1/4} \left(\frac{r_{\text{p}}}{r_{\text{p}^*}}\right)^{-3/4} \left(\frac{\dot{M}}{\dot{M}_{\text{p}}}\right)^{1/4} \\
 &\simeq 3.69 \times 10^4 \text{ (K)} f^{1/4} D_{\text{p}}^{1/4} \beta_*^{1/4} \left(\frac{f_{\text{T}}}{1.56}\right)^{-2} r_*^{-9/8} m_*^{11/12} M_6^{-7/24} \times \\
 &\quad \left[\frac{3(n-1)}{2}\right]^{1/4} (1 + \Delta_*)^{1/2} \left(\frac{1 + e}{2}\right)^{-3/4} \left(\frac{r_{\text{p}}}{r_{\text{p}^*}}\right)^{-3/4} \left(\frac{\dot{M}}{\dot{M}_{\text{p}}}\right)^{1/4}
 \end{aligned} \tag{150}$$

for  $r_{\text{mb}} \leq r_{\text{p}} \leq r_{\text{p}^*}$ , where we have used  $r_{\text{p}} = (1 - e)a$ ,  $1 - e^2 = 2\delta(1 + \Delta_*)$ , and  $B_0 = 3/2$ . The elliptical accretion disk with accretion rate  $\dot{M} \gtrsim \dot{M}_{\text{cr}}$  has a distribution of effective temperature with pericenter radius  $r_{\text{p}}^{-3/4}$  and increases with accretion rate  $\dot{M}^{1/4}$ , which are the same as those of a standard thin accretion disk (Frank et al. 2002) but have much lower peak value. Equation (150) shows that the elliptical accretion disk with accretion rate  $\dot{M}_{\text{p}} \gtrsim \dot{M}_{\text{cr}}$  has a distribution of temperature from  $T_{\text{bb}} \simeq 3.7 \times 10^4 \text{ K}$  at  $r_{\text{p}} = 23.545r_{\text{S}}$  to the maximum temperature  $T_{\text{bb}} \simeq 8.2 \times 10^4 \text{ K}$ .

Our results suggest that for optical/UV TDEs during accretion rate  $\dot{M}_{\text{p}} \gtrsim \dot{M}_{\text{cr}}$  the effective blackbody radius would remain constant, as is shown in Figure 4 for viscosity parameter  $\alpha_{\text{p}} = 0.05$  and 0.1 and in Figure 5 for BH mass  $M_{\text{BH}} = 10^{5.5} M_{\odot}$ . The blackbody temperature changes with accretion rate as a power law  $T_{\text{bb}} \propto \dot{M}^{1/4}$  and would increase with time before peak brightness and decrease afterward until  $\dot{M} < \dot{M}_{\text{cr}}$ , as is shown in Figure 2 for viscosity parameter  $\alpha_{\text{p}} = 0.05$  and 0.1 and in Figure 3 for less massive SMBH mass  $M_{\text{BH}} = 10^{5.5} M_{\odot}$ . When the accretion rate  $\dot{M}$  decreases to smaller than the critical rate  $\dot{M}_{\text{cr}}$  at late times, the SED becomes a blackbody spectrum of nearly single and constant temperature as given by equation (140), and the blackbody radius decreases with time as suggested by equation (146).

## 7. COMPARISONS WITH THE OBSERVATIONS OF OPTICAL/UV TDES

In this section, we compare the expectations of the elliptical accretion disk model with the observations of optical/UV TDEs. The low radiation efficiency of an elliptical accretion disk and its implications for the observations of the peak luminosity, total accreted mass, and the measurements of BH masses of TDEs have been discussed in recent work (Zhou et al. 2021).

### 7.1. Blackbody SEDs of single temperature of all optical/UV TDEs

One of the puzzling observations of optical/UV TDEs is that the SEDs can be well fitted with blackbody of nearly single temperature and the blackbody temperature ranges from  $1 \times 10^4$  K to  $6 \times 10^4$  K (Gezari et al. 2012; Holoien et al. 2014; Wevers et al. 2017, 2019; van Velzen et al. 2021). The effective blackbody temperature does not correlate with the estimated BH masses of optical/UV TDEs (Wevers et al. 2017, 2019).

Equation (140) shows that the temperature  $T_{\text{bb}}$  depends only weakly on the pericenter radius,  $T_{\text{bb}} \propto r_{\text{p}}^{-6/17} \propto r_{\text{p}}^{-0.35}$  with a power-law index much smaller than the index 0.75 of the standard thin or slim accretion disk (Abramowicz et al. 1988; Frank et al. 2002). For a typical tidal disruption of optical/UV TDEs by SMBHs of mass  $10^6 M_{\odot}$  and penetration factor  $\beta_* \simeq 1$ , the effective temperature  $T_{\text{bb}}$  increases only by about 70% (1.7 times), when pericenter radius  $r_{\text{p}}$  decreases from the outer boundary  $r_{\text{p}} \simeq 23.545 r_{\text{S}}$  to  $r_{\text{p}} \simeq 3 r_{\text{S}}$ . The effective surface temperature of the standard thin accretion disk increases by about 370% (4.7 times) for the same range of radius, neglecting the effect of the inner boundary condition. The small variation of effective blackbody temperature of the elliptical accretion disk would radiate with a blackbody spectrum of nearly single temperature.

Equation (140) suggests that the blackbody temperature of the elliptical accretion disk is nearly independent of the BH mass  $T_{\text{bb}} \propto M_6^{11/272} \propto M_6^{0.040}$ , which is well consistent with the observations of optical/UV TDEs (Wevers et al. 2017, 2019). The blackbody temperature weakly depends on the orbital penetration factor and the mass of a star  $T_{\text{bb}} \propto \beta_*^{6/17} r_*^{-63/272} m_*^{-3/68} \propto \beta_*^{0.35} m_*^{-(75-63\zeta)/272} \propto \beta_*^{0.35} m_*^{-0.23}$  for  $\zeta = 0.21$  but varies with the viscosity parameter  $T_{\text{bb}} \propto \alpha_{\text{p}}^{81/136} \propto \alpha_{\text{p}}^{0.596}$ . The recent observations of the disk-dominated late-time UV luminosity of optical/UV TDEs suggest that the disk viscosity parameter is roughly between 0.07 and 0.6 (van Velzen et al. 2019). The estimates of the viscosity parameter are based on a circular disk model of radial size  $2r_{\text{p}*}$  (van Velzen et al. 2019), and the viscosity parameter of the elliptical disk model is for the viscous pericenter region of the elliptical disk of the radial size of about  $r_{\text{p}*}$  and azimuthal span  $\sim \pi$ . The inferred  $\alpha$  values cannot be exactly applicable, but it is reasonable to expect that they are suitable to the elliptical disk model within orders of magnitude and that we have  $0.01 \lesssim \alpha_{\text{p}} \lesssim 1$  with typical value  $\alpha_{\text{p}} \sim 0.2$ . For the range of the viscosity parameters  $0.05 \lesssim \alpha_{\text{p}} \lesssim 0.5$ , the blackbody temperature  $T_{\text{bb}}$  ranges from  $1 \times 10^4$  K to  $8 \times 10^4$  K, well consistent with the observations.

Because the effective blackbody radius  $R_{\text{bb}}$  also depends on the viscosity parameter  $\alpha_{\text{p}}$ , the elliptical accretion disk model predicts a strong correlation between the effective blackbody temperature  $T_{\text{bb}}$  and blackbody radius  $R_{\text{bb}}$ , which will be discussed in Section 7.4.

### 7.2. Time (in)dependence of blackbody temperature

It is well known that the blackbody temperature of optical/UV TDEs changes little with time (Gezari et al. 2012, 2017a; Holoien et al. 2014, 2019; van Velzen et al. 2019, 2021; Hinkle et al. 2020). Table 6 of van Velzen et al. (2021) gave the measurements of the blackbody temperature and its variations with time ( $dT_{\text{bb}}/dt$ ) of 17 optical/UV TDEs. The measurements of  $dT_{\text{bb}}/dt$  have a very large scatter and ranges from  $-0.85 \times 10^2$  K day $^{-1}$  to  $1.95 \times 10^2$  K day $^{-1}$  with an average  $\langle dT_{\text{bb}}/dt \rangle_{\text{ob}} \sim 0.47 \times 10^2$  K day $^{-1}$ .

Equation (139) gives the variation of the blackbody temperature with the accretion rate

$$T_{\text{bb}} \propto \left[ \frac{3(n-1)}{2} \right]^{11(\gamma-2)/4(11\gamma-7)} \left( 1 - \frac{r_0}{2a} \right)^{(11\gamma-25)/8(11\gamma-7)} \left( \frac{\dot{M}}{\dot{M}_{\text{p}}} \right)^{11(\gamma-2)/4(11\gamma-7)}, \quad (151)$$

where the radiation radius  $r_0$  given with equation (115) changes with accretion rate. The term  $(1 - \frac{r_0}{2a})$  is important when  $\dot{M} \sim \dot{M}_{\text{cr}}$  and  $r_0 \sim (1 + e)a_{\text{d}}$ . From equation (2), we have

$$\begin{aligned} T_{\text{bb}} &\propto \left[ \frac{3(n-1)}{2} \right]^{11(\gamma-2)/4(11\gamma-7)} \left( 1 - \frac{r_0}{2a} \right)^{(11\gamma-25)/8(11\gamma-7)} \left( \frac{t + \Delta t_{\text{p}}}{\Delta t_{\text{p}}} \right)^{-11n(\gamma-2)/4(11\gamma-7)} \\ &\propto \left( 1 - \frac{r_0}{2a} \right)^{-5/68} \left( \frac{t + \Delta t_{\text{p}}}{\Delta t_{\text{p}}} \right)^{0.13} \quad \text{for } n = 5/3, \\ &\propto \left( 1 - \frac{r_0}{2a} \right)^{-5/68} \left( \frac{t + \Delta t_{\text{p}}}{\Delta t_{\text{p}}} \right)^{0.18} \quad \text{for } n = 9/4. \end{aligned} \quad (152)$$

To obtain the equation (152), we have adopted the typical polytropic index  $\gamma = 5/3$ . Because  $r_0$  decreases with time, the blackbody temperature decreases with time for  $\dot{M} \lesssim \dot{M}_{\text{cr}}$  and then increases slowly with time at later. The expected change of the blackbody temperature at late time is

$$\begin{aligned} \frac{dT_{\text{bb}}}{dt} &= -n \frac{11(\gamma-2)}{4(11\gamma-7)} \left( \frac{T_{\text{bb}}}{\Delta t_{\text{p}}} \right) \left( 1 + \frac{t_{\text{f}}}{\Delta t_{\text{p}}} \right)^{-1} \\ &\simeq 0.652 \times 10^2 \text{ (K day}^{-1}\text{)} \alpha_{-1}^{81/136} \beta_{\text{g}}^{-99/272} \beta_{*}^{6/17} f_{\text{T}}^{-423/136} r_{*}^{-471/272} m_{*}^{65/68} \times \\ &\quad M_6^{-125/272} \left( 1 + \frac{t_{\text{f}}}{\Delta t_{\text{p}}} \right)^{-353/408} \end{aligned} \quad (153)$$

for  $\gamma = 5/3$  and  $n = 5/3$ , where  $t_{\text{f}}$  is the time at the end of the observational campaign. Equation (153) shows that  $dT_{\text{bb}}/dt$  depends on the indices  $\gamma$  and  $n$ , the masses of the SMBH and the star, the viscosity parameter  $\alpha_{\text{p}}$ , and the duration of the observational campaign. Because of the differences of the parameters  $M_{\text{BH}}$ ,  $M_{*}$ ,  $\alpha_{\text{p}}$ , and the ratio of the observational time  $t_{\text{f}}$  to  $\Delta t_{\text{p}}$  among TDEs, a large scatter of the measurements of the change rate of blackbody temperature is expected. Therefore, we would suggest to measure

$$\frac{d(\ln T_{\text{bb}})}{d[\ln(t + \Delta t_{\text{p}})]} \simeq -n \frac{11(\gamma-2)}{4(11\gamma-7)}, \quad (154)$$

which depends only on the polytropic index  $\gamma$  and the power-law index of fallback rate  $n$ .

To compare the expectations of the elliptical accretion disk and the observations of optical/UV TDEs in van Velzen et al. (2021), we need  $t_{\text{f}}/\Delta t_{\text{p}}$ . To obtain  $t_{\text{f}}/\Delta t_{\text{p}}$ , we use their fitting results of the  $\Delta t_{\text{p}}$  in Table 6 of van Velzen et al. (2021) for  $n = 5/3$ . From their figure 5, we have the average  $\langle t_{\text{f}}/\Delta t_{\text{p}} \rangle \sim 1.03$ . From equation (153), we have the model expectation  $dT_{\text{bb}}/dt \sim 0.35 \times 10^2 \text{ (K day}^{-1}\text{)} \alpha_{-1}^{81/136} f_{\text{T}}^{-423/136} m_{*}^{-0.412} M_6^{-125/272} \sim 0.32 \times 10^2 (\alpha/0.3)^{81/136} \text{ K day}^{-1}$  for  $\zeta = 0.21$ ,  $\beta_{\text{g}} \simeq 1$ ,  $\beta_{*} \simeq 1$ ,  $M_6 = 1$ ,  $f_{\text{T}} = 1.5$ , and  $m_{*} \simeq 0.3$ . To compare the model expectations with the average of observations, we adopt the typical mass of a star,  $m_{*} \simeq 0.3$  for typical initial mass function (IMF). Taking into account the large scatters of the observations, we conclude that the model expectation of the decay rate  $dT_{\text{bb}}/dt \sim 0.32 \times 10^2 (\alpha/0.3)^{81/136} \text{ K day}^{-1}$  is consistent with the observations  $\langle dT_{\text{bb}}/dt \rangle_{\text{ob}} \sim 0.47 \times 10^2 \text{ K day}^{-1}$ .

We have adopted the adiabatic index  $\gamma = 5/3$  as the fiducial value, because the gradient of the temperature in the  $z$ -direction is expected to be  $\frac{\delta T}{T} \sim 0$  at  $r_{\text{p}}$  owing to the strong compressing shocks near pericenter, and the emission in the regions  $r \ll r_0$  is negligible. Because the radiation at  $r \ll r_0$  is mainly in soft X-rays, no significant emission is expected for polytropic process with  $\gamma = 5/3$ . If the radiation cooling in soft X-rays in the region of the ellipse  $r_{\text{p}} \lesssim r \ll r_0$  is significant,

the polytropic index  $\gamma$  would be larger than the adiabatic index  $\gamma = 5/3$ . Equation (153) shows that a larger polytropic index  $\gamma$  results in a smaller increase of the blackbody temperature with time. If the radiation cooling in soft X-rays is comparable to the optical/UV luminosity and  $\gamma \simeq 2$ , we would have a constant blackbody temperature with  $dT_{\text{bb}}/dt = 0$ , while for  $\gamma > 2$  the blackbody temperature would decrease with time,  $dT_{\text{bb}}/dt < 0$ . The elliptical accretion disk model predicts that optical/UV TDEs with significant X-ray radiation would have constant or even decreasing blackbody temperature with time. The X-ray-bright ( $L_X \sim L_{\text{opt}}$ ) optical TDEs ASASSN-14li, with a rather constant temperature with  $dT_{\text{bb}}/dt \simeq 0$  (Holoien et al. 2016a), and AT2019ehz, with a decaying temperature with  $dT_{\text{bb}}/dt \simeq -0.24 \times 10^2 \text{ K day}^{-1}$  (van Velzen et al. 2021), are consistent with the expectation. TDE AT2019dsg is the first TDE candidate associated with a neutrino event source and is detected in X-ray with a ratio of the X-ray to optical luminosities  $L_X/L_{\text{opt}} \simeq 0.1$  (Stein et al. 2020). The source has a moderate relativistic jet. The change rate of the blackbody temperature is  $dT_{\text{bb}}/dt \simeq 0.24 \times 10^2 \text{ K day}^{-1}$  (van Velzen et al. 2021), consistent with the elliptical accretion disk model for  $\gamma = 5/3$ .

### 7.3. Large and evolving blackbody radius

The observations of optical/UV TDEs (e.g. Holoien et al. 2014, 2019; Leloudas et al. 2019; Gomez et al. 2020; Hinkle et al. 2020; Short et al. 2020; van Velzen et al. 2021) show that the blackbody radii generally follow the luminosity to increase before peak brightness and reach a maximum near or soon after the peak brightness. The maximum of the effective blackbody radius is in the range  $10^{14.18} \text{ cm} \lesssim R_{\text{bb}} \lesssim 10^{15.47} \text{ cm}$  (Wevers et al. 2019; van Velzen et al. 2021). After the peak, the effective blackbody radii generally decrease with the decay of luminosity.

The equation (146) shows that the effective blackbody radius changes with the accretion rate

$$\begin{aligned}
 R_{\text{bb}} &\simeq 1.87 \times 10^{15} \text{ (cm)} \alpha_{-1}^{-81/68} f^{11/68} \left( \frac{2r_{\text{S}}}{r_{\text{ms}}} \right)^{1/2} (1 + \Delta_*)^{1/2} \beta_*^{-41/34} \times \\
 &\quad f_{\text{T}}^{-121/68} r_*^{-39/136} m_*^{64/51} M_6^{-203/408} \left[ \frac{3(n-1)}{2} \right]^{45/68} \left( 1 - \frac{r_0}{2a} \right)^{5/34} \left( \frac{\dot{M}}{\dot{M}_{\text{p}}} \right)^{45/68} \\
 &\simeq 1.87 \times 10^{15} \text{ (cm)} \alpha_{-1}^{-81/68} f^{11/68} \left( \frac{2r_{\text{S}}}{r_{\text{ms}}} \right)^{1/2} (1 + \Delta_*)^{1/2} \beta_*^{-41/34} \times \\
 &\quad f_{\text{T}}^{-121/68} r_*^{-39/136} m_*^{64/51} M_6^{-203/408} \left[ \frac{3(n-1)}{2} \right]^{45/68} \left( 1 - \frac{r_0}{2a} \right)^{5/34} \left( \frac{t + \Delta t_{\text{p}}}{\Delta t_{\text{p}}} \right)^{-45n/68}, \quad (155)
 \end{aligned}$$

which gives

$$\begin{aligned}
 R_{\text{bb}} &\simeq 1.87 \times 10^{15} \text{ (cm)} \alpha_{-1}^{-81/68} f^{11/68} \left( \frac{2r_{\text{S}}}{r_{\text{ms}}} \right)^{1/2} (1 + \Delta_*)^{1/2} \beta_*^{-41/34} \times \\
 &\quad f_{\text{T}}^{-121/68} r_*^{-39/136} m_*^{64/51} M_6^{-203/408} \left( 1 - \frac{r_0}{2a} \right)^{5/34} \left( \frac{t + \Delta t_{\text{p}}}{\Delta t_{\text{p}}} \right)^{-1.10} \quad (156)
 \end{aligned}$$

for  $n = 5/3$  and

$$R_{\text{bb}} \simeq 2.83 \times 10^{15} \text{ (cm)} \alpha_{-1}^{-81/68} f^{11/68} \left( \frac{2r_{\text{S}}}{r_{\text{ms}}} \right)^{1/2} (1 + \Delta_*)^{1/2} \beta_*^{-41/34} \times$$

$$f_{\text{T}}^{-121/68} r_*^{-39/136} m_*^{64/51} M_6^{-203/408} \left(1 - \frac{r_0}{2a}\right)^{5/34} \left(\frac{t + \Delta t_{\text{p}}}{\Delta t_{\text{p}}}\right)^{-1.49} \quad (157)$$

for  $n = 9/4$ , where  $r_0$  is given with equation (117). The effective blackbody radius decreases significantly with time, consistent with the observations. Both equations (156) and (157) show that the peak blackbody radius depends on both the mass of the star and the effective viscosity parameter,  $R_{\text{bb}} \propto m_*^{(395+117\zeta)/408} \alpha_{\text{p}}^{-81/68} \propto m_*^{1.08} \alpha_{\text{p}}^{-1.19}$  for  $\zeta = 0.21$ . The peak blackbody radius depends also on the orbital penetration factor of the star,  $R_{\text{bb}} \propto \beta_*^{-41/34}$ . For the BH mass  $10^{5.5} M_{\odot} \lesssim M_{\text{BH}} < 10^8 M_{\odot}$  and the star mass  $0.08 \lesssim m_* \lesssim 1$ , the elliptical accretion disk model with the ranges of the orbital penetration factor  $0.2 \lesssim \beta_* \lesssim 3$  and effective viscosity parameter  $0.01 \lesssim \alpha_{\text{p}} \lesssim 1$  could give a peak blackbody radius consistent with the observations  $10^{14} \text{ cm} \lesssim R_{\text{bb}} \lesssim 10^{15.5} \text{ cm}$ . Figure 6 gives the peak blackbody radius  $R_{\text{bb}}$  as a function of the BH mass for different stellar masses, the orbital penetration factor  $\beta_*$  of the star, and the effective viscosity parameter  $\alpha_{\text{p}}$ . Figure 6 shows that the peak blackbody radius increases with the mass of the star and inversely with the orbital penetration factor of the star. When the peak accretion rate  $\dot{M}_{\text{p}}$  is large and the radiation radius  $r_0$  is determined by  $r_0 \simeq (1+e)a_{\text{d}}$ , the peak blackbody radius increases with the BH mass and is independent of the effective viscosity parameter  $\alpha_{\text{p}}$ . When the peak accretion rate  $\dot{M}_{\text{p}}$  decreases with the BH mass (see equation (4)) until the radiation radius  $r_0$  at the peak accretion rate is  $r_0 < (1+e)a_{\text{d}}$  and is given with equation (117), the peak blackbody radius decreases with the BH mass. The critical BH mass depends on the effective viscosity parameter  $\alpha_{\text{p}}$ .

#### 7.4. Anticorrelation of the blackbody temperature and blackbody radius

The recent observations with the sample of 39 optical/UV TDEs showed that the blackbody temperature at the peak brightness strongly anticorrelates with the peak spherical blackbody radius

$$L_{\text{bb}} = 4\pi R_{\text{bb}}^2 \sigma_{\text{SB}} T_{\text{bb}}^4 \quad (158)$$

with a scatter of about 0.3 dex and the best fit  $L_{\text{bb}} \simeq 10^{44.05} \text{ erg s}^{-1}$  (van Velzen et al. 2021). From equation (158), we have the empirical correlation of the blackbody temperature and the effective blackbody radius

$$\begin{aligned} T_{\text{bb}} &= \left(\frac{L_{\text{bb}}}{4\pi 10^6 r_{11}^2 \sigma_{\text{SB}}}\right)^{1/4} \left(\frac{R_{\text{bb}}}{10^3 r_{11}}\right)^{-1/2} \\ &\simeq 3.67 \times 10^4 \text{ K} \left(\frac{R_{\text{bb}}}{10^3 r_{11}}\right)^{-1/2}. \end{aligned} \quad (159)$$

Equations (140) and (146) show that both the blackbody temperature  $T_{\text{bb}}$  and the effective blackbody radius  $R_{\text{bb}}$  depend mainly on the viscosity parameter  $\alpha_{\text{p}}$ . With equation (145), we eliminate the viscosity parameters  $\alpha_{\text{p}}$  from equation (139) and obtain the correlation of the blackbody temperature and radius at the peak accretion rate

$$\begin{aligned} T_{\text{bb}} &\simeq 3.27 \times 10^4 \text{ K} \left(\frac{1+e}{2}\right)^{-1/4} \left(\frac{2r_{\text{S}}}{r_{\text{ms}}}\right)^{1/4} \left[1 - \delta \frac{(1+\Delta_*)}{(1+e)} \left(\frac{r_{\text{S}}}{r_{\text{ms}} - r_{\text{S}}}\right)\right]^{1/4} (1+\Delta_*)^{1/4} \times \\ &\quad \beta_*^{-1/4} \left(\frac{f_{\text{T}}}{1.56}\right)^{-1} r_*^{-3/8} m_*^{7/12} M_6^{-5/24} \left[\frac{3(n-1)}{2}\right]^{1/4} \left(\frac{R_{\text{bb}}}{10^3 r_{11}}\right)^{-1/2}. \end{aligned} \quad (160)$$

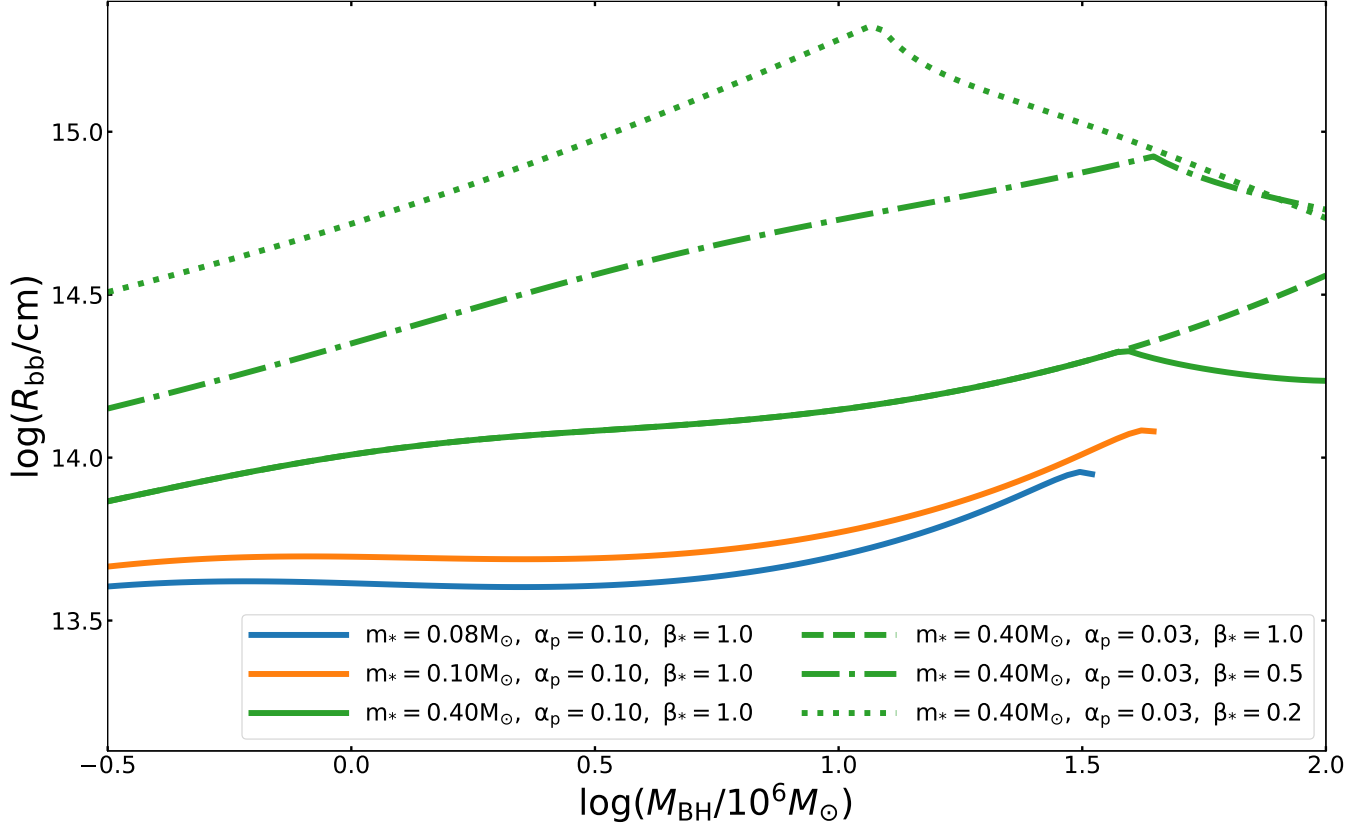


**Figure 6.** Peak blackbody radius as a function of the BH mass. The peak blackbody radius is calculated with  $n = 9/4$  for  $\beta_* < 1$  and  $n = 5/3$  for  $\beta_* \geq 1$ . In the calculations, the other parameters are  $r_{\text{ms}} = 2r_{\text{S}}$ , and  $f_{\text{T}} = f_*(0.80 + 0.26M_6^{0.5})$  with  $f_* = 1.212$  (Ryu et al. 2020a).

Equation (160) can also be obtained from equation (144) with a bit more algebraic calculations. The correlation is independent of both the polytropic index  $\gamma$  and of the physical mechanism driving the variations of the blackbody temperature. Figure 7 overplots the expected correlation and intrinsic scatter given by equation (160) on the observations of optical/UV TDEs (van Velzen et al. 2021). The theoretical correlation in Figure 7 is obtained with  $n = 5/3$ ,  $r_{\text{ms}} = 2r_{\text{S}}$ ,  $\beta_* = 1$ ,  $M_{\text{BH}} = 10^{5.5}M_{\odot}$ ,  $10^6M_{\odot}$ ,  $10^{6.5}M_{\odot}$ , and  $10^7M_{\odot}$  with  $f_{\text{T}} = f_*(0.80 + 0.26M_6^{0.5})$ , and  $m_* = 0.4$ . Here we use  $f_* = 1.212$  for  $m_* = 0.4$  (Ryu et al. 2020a). Equation (160) gives a strong anticorrelation of the blackbody temperature and radius with a small scattering because of the weak dependence of the BH mass ( $\propto M_6^{-0.21}$ ) and the stellar mass ( $\propto r_*^{-3/8}m_*^{7/12} \sim m_*^{(5+9\zeta)/24} \sim m_*^{0.287}$ ). For BHs of mass  $10^{5.5}M_{\odot} \lesssim M_{\text{BH}} \lesssim 10^7M_{\odot}$ , stars of mass  $0.08 \lesssim m_* \lesssim 3$ , and orbital penetration factor  $0.5 \lesssim \beta_* \lesssim 3$ , we have an intrinsic scatter  $\sim 0.33$  dex. Figure 7 and equation (160) show that the elliptical accretion disk can reproduce not only the anticorrelation of blackbody temperature and blackbody radius but also the intrinsic scatter of the empirical correlation and suggest that the intrinsic scatter of the correlation is mainly due to the differences of the masses of BHs and stars and possibly of the orbital penetration factor  $\beta_*$ . The slope of the logarithmic correlation of the temperature and blackbody radius is the result of the assumption that no strong outflows emerge from the accretion disk and the radial advection cooling of the heat across the ellipse is negligible, resulting in the luminosity closely following the mass fallback rate. The normalization of the correlation and its dependence on the

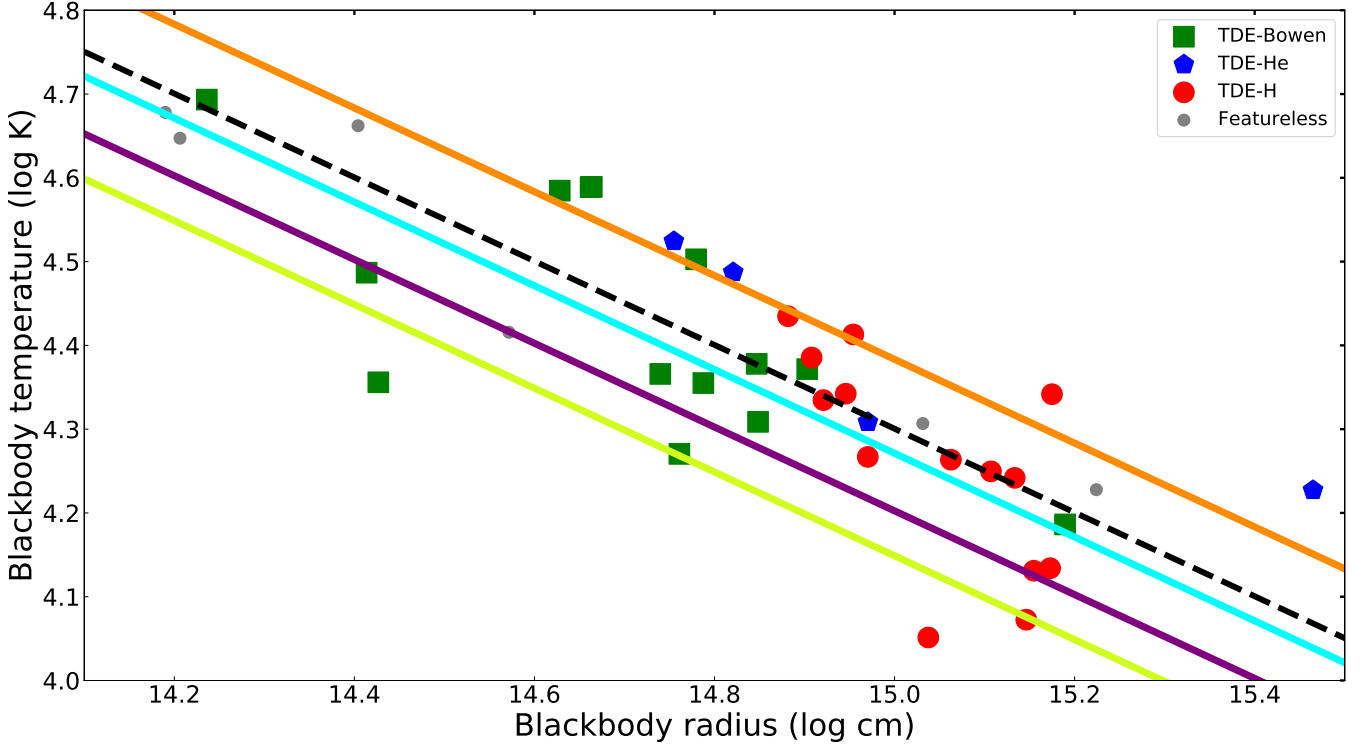


**Figure 7.** Expected correlation of the blackbody temperature and the effective blackbody radius vs the observations. The observational data and the best fit (black dashed) are taken from Figure 8 of [van Velzen et al. \(2021\)](#). The theoretical correlations are, respectively, for SMBH mass  $M_{\text{BH}} = 10^{5.5} M_{\odot}$  (orange solid),  $10^6 M_{\odot}$  (cyan solid),  $10^{6.5} M_{\odot}$  (purple solid), and  $10^7 M_{\odot}$  (lime yellow solid). In the calculations, the other parameters are  $n = 5/3$ ,  $r_{\text{ms}} = 2r_{\text{S}}$ ,  $\beta_* = 1$ ,  $m_* = 0.4$ , and  $f_{\text{T}} = f_*(0.80 + 0.26M_6^{0.5})$  with  $f_* = 1.212$  ([Ryu et al. 2020a](#)). The slope and correlation coefficients of the observations appear naturally in the elliptical accretion disk model.

masses of the BHs and stars and on the orbital penetration factor result from the assumptions that the accretion disk is elliptical with nearly uniform eccentricity over the disk and that the eccentricity is determined jointly by the location of the self-intersections and the conservations of the angular momentum of the streams.

### 7.5. TDE-Bowen TDEs have smaller blackbody radius and larger blackbody temperature

Recent studies ([van Velzen et al. 2021](#)) have shown that TDEs with both broad Balmer emission lines and Bowen fluorescence emission lines (TDE-Bowen TDEs) may have larger blackbody temperatures and smaller blackbody radii at peak brightness than TDEs with Balmer line features only (TDE-H TDEs). The two spectroscopic classes of TDEs have similar blackbody luminosity. Because the Bowen fluorescence mechanism requires both a high flux of EUV photons and a high gas density, [van Velzen et al. \(2021\)](#) interpret the observations to suggest that the TDE-Bowen class has higher gas density, larger blackbody temperature, and smaller blackbody radius than the TDE-H population.

In the elliptical accretion disk model, the broad emission lines are suggested to originate in the elliptical accretion disk ([Liu et al. 2017](#); [Cao et al. 2018](#)). The elliptical accretion disk model is able to fit well the double-peaked broad  $\text{H}\alpha$  profiles of the TDEs PTF09djl ([Liu et al. 2017](#)) and AT 2018hyz/ASASSN-18zj ([Hung et al. 2020](#); [Short et al. 2020](#)), the single-peaked broad  $\text{H}\alpha$

profiles of ASASSN-14li (Cao et al. 2018), and the flat-topped Balmer lines of AT2018zr/PS18kh (Holoien et al. 2018) because of the strong dependence of the emission-line profiles on the orientation and shape of the elliptical disk (Cao et al. 2018), and it can explain the flat Balmer decrement of a number of TDEs (Short et al. 2020). The disk origin of broad emission lines of TDEs requires that the accretion disk of TDE-Bowen TDEs has higher mass density than the accretion disk of TDE-H TDEs does. From equation (122), we have the mass density of TDEs,  $\rho \propto \alpha_{-1}^{-2/17} r_*^{-57/34} m_*^{14/17} M_6^{-3/34} [3(n-1)/2]^{3/17} \left(\dot{M}/\dot{M}_p\right)^{3/17} (r_p/r)$ , which is nearly independent of the accretion rate, the BH mass, and the viscosity parameters. Because the gas density inversely correlates with the stellar mass,  $\rho \propto m_*^{-(29-57\zeta)/34} \propto m_*^{-0.501}$ , TDE-Bowen TDEs are expected to have smaller masses of stars with respect to the TDE-H population. Equations (140) and (146) show that a smaller mass of a star implies a higher blackbody temperature and smaller blackbody radius of TDE-Bowen TDEs, which are consistent with the observations (van Velzen et al. 2021). To give quantitative comparison of the observations and the disk expectations, detailed radiative transfer calculations of the broad emission lines are needed, which is beyond the scope of this paper. Because the gas density is nearly independent of the mass of BHs,  $\rho \propto M_6^{-3/34}$ , and the large intrinsic scatter of the host galaxy correlation of the  $M_{\text{BH}}-M_{\text{tot}}$  (Häring & Rix 2004; Kormendy & Ho 2013; McConnell & Ma 2013), no correlation between the spectroscopic classification of TDEs and the total mass of host galaxy  $M_{\text{tot}}$  is expected. The prediction is in line with the observations (van Velzen et al. 2021).

### 7.6. Steep decrease of TDE event rate with the effective blackbody radius

The observations show that the TDE-Bowen class has low optical luminosity at the peak but has been detected in equal numbers to the H-only class (van Velzen et al. 2021). The low luminosity implies a higher intrinsic rate. Because the TDE-Bowen class has smaller blackbody radii at peak relative to the H-only class, the observations suggested a steep decrease of the event rate of TDEs with the blackbody radius at peak brightness,  $dN_{\text{TDE}}/dR_{\text{bb}} \propto R_{\text{bb}}^{-3}$  (van Velzen et al. 2021). van Velzen et al. (2021) showed that the correlation between the event rate of TDEs and blackbody radius at peak could be explained with a typical IMF of the stellar population, e.g.,  $dN_*/dM_* \propto M_*^{-2.3}$  (Kroupa 2001), provided that the blackbody radius of TDEs would be proportional to the mass of the star and the stars of the TDE-Bowen class have small mass.

As was discussed in Section 7.5, a high mass density is required to produce Bowen emission lines, and the stars of the TDE-Bowen class should have smaller masses, consistent with the requirement of the observations. From equation (146), the effective blackbody radius is  $R_{\text{bb}} \propto r_*^{-39/136} m_*^{64/51} \propto m_*^{(395+117\zeta)/408}$ . Because  $\zeta \simeq 0.21$  for  $0.1 \lesssim m_* \leq 1$  and  $\zeta \simeq 0.44$  for  $1 < m_* \leq 150$  (Kippenhahn & Weigert 2012), we have  $R_{\text{bb}} \propto m_*^{1.03}$  for  $0.1 \lesssim m_* \leq 1$  and  $R_{\text{bb}} \propto m_*^{1.09}$  for  $1 < m_* \leq 150$ , exactly as required by the observations.

## 8. DISCUSSION AND CONCLUSIONS

Liu and colleagues (Liu et al. 2017; Cao et al. 2018) suggested that the broad optical emission lines of TDEs originate in an elliptical accretion disk and showed that the broad double-peaked profiles of H $\alpha$  emission lines of TDE PTF09djl imply a large and highly eccentric elliptical accretion disk of nearly uniform eccentricity. A highly eccentric accretion disk would convert only a small fraction of matter into radiation (Liu et al. 2017; Cao et al. 2018; Zhou et al. 2021) – see also Svirski et al. (2017) and Piran et al. (2015) for a summary of a parallel, independent work by Piran

and collaborators, who stressed that optical/UV TDEs are powered by the shocks owing to the self-intersections of streams near apocenter. The predicted luminosities at peak and total radiation energies and the inferred BH masses with the elliptical disk model with uniform eccentricity are well consistent, respectively, with the observations of TDEs and the host galaxy properties (Zhou et al. 2021). In this paper, we investigate the hydrodynamic structures and SED of the elliptical accretion disk of uniform eccentricity, based on the analytical treatments of fluid hydrodynamics, viscosity, radiative transfer, the heat generation and cooling, and the general relativistic effects, captured with the generalized Newtonian potential.

Our results show that the highly eccentric elliptical accretion disk has distinctive hydrodynamic properties and SED with respect to the circular accretion disk because of the significant variations of the hydrodynamics and radiative transfer around the eccentric ellipse. The elliptical accretion disk cannot reach vertical hydrostatic equilibrium, and the flows are laminar because of the variations of the vertical gravitational potential around the ellipse. The elliptical accretion disk is geometrically thin and optically thick. The surface density is nearly constant around the ellipse as in the circular accretion disk, but the gas density decreases linearly with radius  $r$  along the ellipse.

Because of the large electron scattering opacity, the soft X-ray photons generated at about the pericenter are well trapped inside the accretion disk and advected around the eccentric ellipse with little emission. When the trapped soft X-ray photons move with the fluids around the ellipse, they are absorbed owing to bound-free and free-free absorptions and reemitted in emission lines and low-frequency continuum because of recombination and bremsstrahlung radiation. Electron scattering does not reprocess the soft X-ray photons into low frequency, but it significantly increases the diffusive path of photons and the effective bound-free and free-free opacities. Because the effective Rosseland mean opacity significantly increases with radius, the vertical diffusion timescale increases with radius and exceeds the dynamical timescale of fluids at the photon-trapping radius  $r_0$ . For  $r > r_0$ , the low-frequency continuum photons are trapped and advected with the fluids through the apocenter and back to  $r_0$ . The elliptical accretion disk emits mainly in the region of size of about the photon-trapping radius  $r_0$  and the radiation from region  $r > r_0$  is small. The photon-trapping radius  $r_0$  is the radiation radius and self-regulates owing to the balance of generation and cooling of heat.

Because the photon-trapping radius is self-regulated and changes with the accretion rate, the temperature of both the disk center and surface of the radiation radius is nearly independent of the BH mass, accretion rate, and the mass of the star. The radiation temperature is determined mainly by the effective viscosity parameter and is typically  $T_{\text{bb}} \simeq 3.0 \times 10^4 \text{ K} (\alpha_{\text{p}}/0.2)^{81/136} [3(n-1)/2]^{-11/136} \beta_*^{6/17} f_{\text{T}}^{-15/136} M_6^{11/272} m_*^{-(75-63\zeta)/272} (r_{\text{p}}/r_{\text{p}*})^{-6/17} (\dot{M}/\dot{M}_{\text{p}})^{-11/136}$  with  $\zeta = 0.21$  for  $0.1 \lesssim m_* \lesssim 1$ . The radiation temperature  $T_{\text{bb}}$  varies weakly with pericenter radius  $r_{\text{p}}$  with a power-law index of 0.353, much smaller than the canonical power-law index of 0.75 in the standard thin accretion disk. The radiation blackbody temperature varies only by a small amount, and the SED of an elliptical accretion disk has a blackbody spectrum of nearly single temperature. The blackbody temperature  $T_{\text{bb}}$  is typically about  $3 \times 10^4 \text{ K}$  and ranges from  $1 \times 10^4 \text{ K}$  to  $8 \times 10^4 \text{ K}$ . Because the BH mass and accretion rate affect the TDE temperature and SEDs only slightly and the stellar mass and the viscosity parameter are more influential, it would be difficult to infer BH mass or accretion from real observations of any particular event, but it would be easier to constrain the stellar mass and the viscosity parameter.

The elliptical accretion disk has very low radiation efficiency and gives rise to a typical total luminosity of optical/UV TDEs,  $L_{\text{bol}} \simeq 0.71 \times 10^{44} \text{ ergs } \beta_*^{-1} (f_{\text{T}}/1.56)^{-4} m_*^{(5+9\zeta)/6} M_6^{-5/6} (1 + \Delta_*) [3(n-1)/2] (2r_{\text{S}}/r_{\text{ms}}) \left( \dot{M}/\dot{M}_{\text{p}} \right)$ . Most TDEs with stellar mass  $m_* < 1$  have sub-Eddington peak luminosities and are expected to have luminosities closely following the mass fallback rate,  $L_{\text{bol}} \simeq 0.49 \beta_*^{-1} (f_{\text{T}}/1.56)^{-4} m_*^{(5+9\zeta)/6} M_6^{-11/6} (1 + \Delta_*) [3(n-1)/2] (2r_{\text{S}}/r_{\text{ms}}) \left( \dot{M}/\dot{M}_{\text{p}} \right) L_{\text{Edd}}$ . Provided the total luminosity  $L_{\text{bol}}$  and the blackbody temperature  $T_{\text{bb}}$ , we have the effective blackbody radius of the elliptical accretion disk,  $R_{\text{bb}} \simeq 10^{14.57} \text{ (cm)} \left( \frac{\alpha_{\text{p}}}{0.2} \right)^{-81/68} \beta_*^{-41/34} (f_{\text{T}}/1.56)^{-121/68} m_*^{(395+117\zeta)/408} M_6^{-203/408} [3(n-1)/2]^{45/68} (1 + \Delta_*)^{1/2} (2r_{\text{S}}/r_{\text{ms}})^{1/2} \left( \dot{M}/\dot{M}_{\text{p}} \right)^{45/68}$ . The effective blackbody radius changes with accretion rate and decrease with time,  $R_{\text{bb}} \propto \left( \dot{M}/\dot{M}_{\text{p}} \right)^{45/68} \propto t^{-1.10}$  for  $n = 5/3$  and  $R_{\text{bb}} \propto t^{-1.49}$  for  $n = 9/4$ .

The elliptical accretion disk has a blackbody radiation spectrum of nearly single and time-independent temperature and a large and varying effective blackbody radiation radius with accretion rate, which are the unique characteristics of optical/UV TDEs and are often adopted to identify them among the nuclear transients in the literature. We quantitatively compare the expectations of the elliptical accretion disk and the observations of optical/UV TDEs. Our results show that the expected blackbody SEDs of nearly single temperature, blackbody temperature and variations with time, effective blackbody radius and dependence on the accretion rate, anticorrelations of the blackbody temperature and blackbody radius at peak, and steep decrease of TDE event rate with blackbody radius at peak are all well consistent with the observations of optical/UV TDEs.

Observations show that the TDE-Bowen class with both broad Balmer and Bowen fluorescence emission lines has larger blackbody temperatures and smaller blackbody radii at peak brightness than the TDE-H population with Balmer line features only (van Velzen et al. 2021). The Bowen fluorescence mechanism requires that the TDE-Bowen class should have high gas density. The observations of spectral TDE classes can be explained, based on the accretion disk origin of the broad emission lines of optical/UV TDEs (Liu et al. 2017; Cao et al. 2018). Because the gas density of the elliptical accretion disk is nearly independent of the BH mass, the accretion rate, and the viscosity parameter and is mainly determined by the mass of the star,  $\rho \propto \alpha_{-1}^{-2/17} m_*^{-(29-57\zeta)/34} M_6^{-3/34} [3(n-1)/2]^{3/17} \left( \dot{M}/\dot{M}_{\text{p}} \right)^{3/17} \propto m_*^{-0.501}$  for  $\zeta = 0.21$ , the observations imply that the stars of the TDE-Bowen class have small masses. The small masses of the stars would lead to the TDE-Bowen class relative to the TDE-H population having a high blackbody temperature,  $T_{\text{bb}} \propto r_*^{-63/272} m_*^{-3/68} \propto m_*^{-(75-63\zeta)/272} \propto m_*^{-0.23}$  for  $\zeta = 0.21$ , and a small effective blackbody radius,  $R_{\text{bb}} \propto r_*^{-39/136} m_*^{64/51} \propto m_*^{(395+117\zeta)/408} \propto m_*^{1.03}$  for  $\zeta = 0.21$ . The expectations of the elliptical accretion disk are well consistent with the spectroscopic observations of TDEs. The expectation for the correlation of the effective blackbody radius and the masses of the stars is well consistent with the observation that the event rate of TDEs steeply decreases with the blackbody radius at peak brightness as  $d\dot{N}_{\text{TDE}}/dR_{\text{bb}} \propto R_{\text{bb}}^{-3}$  and the steep decrease of number density of a star with the stellar masses in the typical IMF,  $dN_*/dM_* \propto M_*^{-2.3}$ . The expectation for small masses of stars of the TDE-Bowen class is consistent with that the TDE-Bowen class relative to the TDE-H population has a higher intrinsic event rate.

Most optical/UV TDEs have strong broad optical emission lines but show little or no X-ray emission (see Komossa 2015, for a recent review). In the accretion disk model for the broad optical emission

lines, an extended soft X-ray source is required to power the broad emission lines of optical/UV TDEs, and the line emissivity of the accretion disk can be approximated with a broken power law in radius (Liu et al. 2017; Cao et al. 2018). In this paper, we showed that the soft X-ray photons are generated in the pericenter region and trapped in disk fluids owing to the extremely large electron scattering opacity. When the soft X-ray photons are advected and move around the eccentric ellipse, they would be absorbed mainly as a result of photon ionization and free-free absorption and reprocessed into emission lines and low-frequency continuum via recombinations and bremsstrahlung radiation. The soft X-ray source is extended up to the entire accretion disk and powers the broad emission lines underneath the atmosphere of the accretion disk. Because of the high gas density and temperature, the collisional excitation may make some contributions to the line emissivity. The broken radius of the broken power law of disk line emissivity may be associated at some extent with the photon-trapping radius of the low-frequency continuum. To determine the broken radius of the disk line emissivity and the correlation with the photon-trapping radius of the continuum, numerical simulations with full radiative transfer are needed.

No significant X-ray radiation is expected to be emitted from the disk surface of an elliptical accretion disk. The observations show that the soft X-ray radiation is detected in a couple of optical/UV TDEs. The origin of the soft X-ray emissions of optical/UV TDEs and the relationship between the optical/UV and soft X-rays TDEs will be discussed in the next work.

Following Liu et al. (2017) and Cao et al. (2018), we assumed for simplicity that the eccentric accretion disk has a uniform eccentricity. In reality, the eccentricity may change with radius (Bonnerot et al. 2016; Svirski et al. 2017), in particular when the orbital pericenter radius of the fluid in the disk is about the innermost stable circular orbit (ISCO),  $r_p \sim r_{\text{ISCO}} = 3r_s$ . It is shown that the orbits of the fluid elements at the inner edge may even be closer to parabolic (Svirski et al. 2017; Chan et al. 2018). However, our results do not change significantly and the conclusions are still valid, if the orbital eccentricity at  $r_p \sim r_{\text{ISCO}}$  is  $e \gtrsim 0.6$ .

### 8.1. Summary

In this paper, we investigate the dynamic structures and the disk SEDs of the elliptical accretion disks in the context of the TDEs. Our results show that such accretion flows have unique characteristics. The elliptical accretion disk is geometrically thin and optically thick and cannot reach vertical hydrodynamic static equilibrium. The flow is laminar. The surface density is nearly constant around the ellipse, but the gas density and temperature significantly vary. The heat and soft X-ray photons are generated at pericenter and nearby and are advected around the ellipse without escaping, because of the large electron scattering opacity and photon trapping. The soft X-ray photons are absorbed owing to the bound-free and free-free absorption and reprocessed into line emission and low-frequency continuum via recombinations and free-free emission. Because of the rapid increase of the bound-free and free-free opacities with radius, the low-frequency continuum photons become trapped in the fluid at the photon-trapping radius and are advected through the apocenter and back to the photon-trapping radius. The emission of the low-frequency continuum originates mainly at the photon-trapping radius. Because the photon-trapping radius is self-regulated and changes with accretion rate, the radiation temperature is nearly independent of both BH mass and accretion rate and depends weakly on the mass of the star and the viscosity parameter. The SED of the elliptical accretion disk resembles that of a single-temperature blackbody. Our results imply that it would be difficult to infer the BH mass from the real observations of any particular event, but it would

be easier to constrain the stellar mass and the viscosity parameter. The predictions of our elliptical accretion disk model are well consistent with the observations of optical/UV TDEs.

### ACKNOWLEDGEMENTS

We would like to thank Tsvi Piran and Stefanie Komossa for insightful comments and discussions and Jiayi Tang for some technical help. We are very grateful to the anonymous referee for helpful comments. This work is supported by the National Natural Science Foundation of China (NSFC No. 11473003, NSFC No. 11721303), the National Key R&D Program of China (grant No. 2020YFC2201400), and the Strategic Priority Research Program of the Chinese Academy of Sciences (Grant No. XDB23010200 and No. XDB23040000). M.A. is supported in part by the inter-excellence project No. LTI17018, aimed to strengthen international collaboration of Czech scientific institutions. M.W. acknowledges the support of the Black Hole Initiative at Harvard University, which is funded by grants from the John Templeton Foundation and the Gordon and Betty Moore Foundation to Harvard University.

### REFERENCES

- Abramowicz, M.A., Czerny, B., Lasota, J.P., & Szuszkiewicz, E. 1988, *ApJ*, 332, 646
- Abramowicz, M.A., Jaroszynski, M., & Sikora, M. 1978, *A&A*, 63, 221
- Abramowicz, M.A., Lasota, J.P., & Igumenshchev, I.V. 2000, *MNRAS*, 314, 775
- Arcavi, I., Gal-Yam, A., Sullivan, M., et al. 2014, *ApJ*, 793, 38
- Asplund, M., Grevesse, N., Sauval, A.J., & Scott, P. 2009, *ARA&A*, 47, 481
- Blagorodnova, N., Cenko, S.B., Kulkarni, S.R., et al. 2019, *ApJ*, 873, 92
- Bonnerot, C., Rossi, E. M., Lodato, G., & Price, D. J. 2016, *MNRAS*, 455, 2253
- Cao, R., Liu, F.K., Zhou, Z.Q., Komossa, S., & Ho, L.C. 2018, *MNRAS*, 480, 2929
- Chan, C.-H., Krolik, J.H., & Piran, T., 2018, *ApJ*, 856, 12
- Coughlin, E.R., & Nixon, C.J. 2019, *ApJL*, 883, L17
- Dai, L., McKinney, J.C., & Miller, M.C. 2015, *ApJL*, 812, L39
- Dai, L., McKinney, J.C., Roth, N., Ramirez-Ruiz, E., & Miller, M.C. 2018, *ApJL*, 859, L20.
- de Sitter, W. 1916, *MNRAS*, 77, 155
- Eddington, A.S. 1918, *ApJ*, 48, 205
- Evans, C.R., & Kochanek, C.S. 1989, *ApJL*, 346, L13
- Frank, J., King, A., & Raine, D. 2002, *Accretion Power in Astrophysics*, (Cambridge University Press: Cambridge)
- Gaskell, C.M., & Rojas Lobos, P.A. 2014, *MNRAS*, 438, L36
- Gezari, S., Blagorodnova, N., Roth, N., et al. 2017a, *ApJ*, 842, 29
- Gezari, S., Cenko, S.B. & Arcavi, I. 2017b, *ApJL*, 851, L47
- Gezari, S., Chornock, R., Rest, A., et al. 2012, *Nature*, 485, 217
- Gomez, S., Nicholl, M., Short, P., et al., 2020, *MNRAS*, 497, 1925
- Guillochon, J., Manukian, H., & Ramirez-Ruiz, E. 2014, *ApJ*, 783, 23
- Guillochon, J. & Ramirez-Ruiz, E. 2013, *ApJ*, 767, 25
- Häring, N., & Rix, H.-W. 2004, *ApJL*, 604, L89
- Hayasaki, K. & Loeb, A. 2016, *NatSR*, 6, 35629
- Hayasaki, K., Stone, N., & Loeb, A. 2013, *MNRAS*, 434, 909
- Hills, J.G. 1975, *Nature*, 254, 295
- Hinkle, J.T., Holoien, T.W.-S., Auchettl, K., et al. 2021, *MNRAS*, 500, 1673
- Hinkle, J.T., Holoien, T.W.-S., Shappee, B.J., et al. 2020, *ApJL*, 894, L10
- Holoien, T.W.-S., Brown, J.S., Auchettl, K., et al. 2018, *MNRAS*, 480, 5689
- Holoien, T.W.-S., Huber, M.E., Shappee, B.J., et al. 2019, *ApJ*, 880, 120
- Holoien, T.W.-S., Kochanek, C.S., Prieto, J.L., et al. 2016a, *MNRAS*, 455, 2918

- Holoien, T.W.-S., Kochanek, C.S., Prieto, J.L., et al. 2016b, *MNRAS*, 463, 3813
- Holoien, T.W.-S., Prieto, J.L., Bersier, D., et al. 2014, *MNRAS*, 445, 3263
- Hung, T., Foley, R.J., Ramirez-Ruiz, E., et al., 2020, *ApJ*, 903, 31
- Ivanov, P.B., & Chernyakova, M. A. 2006, *A&A*, 448, 843
- Jiang, Y.-F., Guillochon, J., & Loeb, A. 2016, *ApJ*, 830, 125
- Kajava, J.J. E., Giustini, M., Saxton, R.D., & Miniutti, G. 2020, *A&A*, 639, A100
- Kippenhahn, R., & Weigert, A. 2014, *Stellar Structure and Evolution* (Berlin, New York: Springer-Verlag)
- Kochanek, C.S. 1994, *ApJ*, 422, 508
- Komossa, S. 2015, *Journal of High Energy Astrophysics*, 7, 148
- Komossa, S., Zhou, H., Wang, T., et al. 2008, *ApJL*, 678, L13
- Kormendy, J., & Ho, L.C. 2013, *ARA&A*, 51, 511
- Krolik, J., Piran, T., & Ryu, T. 2020, *ApJ*, 904, 68
- Krolik, J., Piran, T., Svirski, G., & Cheng, R.M. 2016, *ApJ*, 827, 127
- Kroupa, P. 2001, *MNRAS*, 322, 231
- Leloudas, G., Dai, L.X., Arcavi, I., et al. 2019, *ApJ*, 887, 218
- Liu, F.K., Zhou, Z.Q., Cao, R., Ho, L.C., & Komossa, S. 2017, *MNRAS*, 472, L99
- Liu, X.-L., Dou, L.-M., Shen, R.-F., & Chen, J.H. 2019, *ApJ*, submitted; arXiv:1912.06081
- Lodato, G., King, A.R., & Pringle, J. E. 2009, *MNRAS*, 392, 332
- Lodato, G., & Rossi, E.M. 2011, *MNRAS*, 410, 359
- Lyubarskij, Y.E., Postnov, K.A., & Prokhorov, M.E., 1994, *MNRAS*, 266, 583
- McConnell, N.J., & Ma, C.-P., 2013, *ApJ*, 764, 184
- Metzger, B.D., & Stone, N.C. 2016, *MNRAS*, 461, 948
- Mockler, B., Guillochon, J., & Ramirez-Ruiz, E. 2019, *ApJ*, 872, 151
- Nicholl, M., Blanchard, P.K., Berger, E., et al. 2019, *MNRAS*, 488, 1878
- Ogilvie, G.I. 2001, *MNRAS*, 325, 231
- Ogilvie, G.I., & Barker, A.J. 2014, *MNRAS*, 445, 2621
- Phinney, E. S. 1989, in *IAU Symp. 136, The Center of the Galaxy*, ed. M. Morris, (Dordrecht: Kluwer), 543
- Piran, T. 2015, in *The Jerusalem Bagel Model - Elliptical Accretion*, lecture at the Jerusalem TDE workshop (Jerusalem: Israel Institute for Advanced Studies, Hebrew Univ. Jerusalem), (<http://astro-icore.phys.huji.ac.il/node/64>)
- Piran, T., Svirski, G., Krolik, J., Cheng, R. M., & Shiokawa, H. 2015, *ApJ*, 806, 164
- Ramirez-Ruiz, E., & Rosswog, S., 2009, *ApJL*, 697, L77
- Rees, M.J. 1988, *Nature*, 333, 523
- Roth, N., Kasen, D., Guillochon, J., & Ramirez-Ruiz, E. 2016, *ApJ*, 827, 3
- Ryu, T., Krolik, J., Piran, T., & Noble, S.C. 2020a, *ApJ*, 904, 98
- Ryu, T., Krolik, J., Piran, T., & Noble, S.C. 2020b, *ApJ*, 904, 99
- Sadowski, A., Tejada, E., Gafton, E., et al. 2016, *MNRAS*, 458, 4250
- Saxton, C.J., Perets, H.B., & Baskin, A. 2018, *MNRAS*, 474, 3307
- Shakura, N.I., & Sunyaev, R.A. 1973, *A&A*, 24, 337
- Shiokawa, H., Krolik, J.H., Cheng, R.M., Piran, T., & Noble, S.C. 2015, *ApJ*, 804, 85
- Short, P., Nicholl, M., Lawrence, A., et al. 2020, *MNRAS*, 498, 4119
- Stein, R., van Velzen, V., Kowalski, M., et al. 2020, arXiv:2005.05340
- Steinberg, E., Coughlin, E.R., Stone, N.C., & Metzger, B.D. 2019, *MNRAS*, 485, L146
- Stone, N., Sari, R., & Loeb, A. 2013, *MNRAS*, 435, 1809
- Strubbe, L.E., & Quataert, E. 2009, *MNRAS*, 400, 2070
- Svirski, G., Piran, T., & Krolik, J. 2017, *MNRAS*, 467, 1426
- Syer, D., & Clarke, C.J. 1992, *MNRAS*, 255, 92
- Tejada, E., & Rosswog, S. 2013, *MNRAS*, 433, 1930
- van Velzen, S., Gezari, S., Hammerstein, E., et al. 2021, *ApJ*, 908, 4
- van Velzen, S., Stone, N.C., Metzger, B.D., et al. 2019, *ApJ*, 878, 82
- Wang, T.-G., Zhou, H.-Y., Komossa, S., et al. 2012, *ApJ*, 749, 115
- Wevers, T., Stone, N.C., van Velzen, S., et al. 2019, *MNRAS*, 487, 4136
- Wevers, T., van Velzen, S., Jonker, P.G., et al. 2017, *MNRAS*, 471, 1694

Zanazzi, J.J., & Ogilvie, G.I. 2020, MNRAS, 499,  
5562

Zhou, Z.Q., Liu, F.K., Komossa, S., et al. 2021,  
ApJ, 907, 77